Light Alkane Activation on Rh(111), an Imperfectly Perfect Surface

Xingyu Wang

Huaibei, Anhui, China

B.S., Anhui University, 2017

A Dissertation presented to the Graduate Faculty

of the University of Virginia in Candidacy for the Degree of

Doctor of Philosophy

Department of Chemistry

University of Virginia

August 2022

Acknowledgement

I remember when I first learned that you could get a Ph.D. without a master's in the US; I was excited. I remember the day I got the offer letter from UVA; I was thrilled, but even more so, relieved. I remember the day I first landed in the Charlottesville airport; I was eager for what was to come and surprisingly, not nervous.

However, I will probably never forget my nervousness before candidacy. I still remember the challenges and frustrations in facing the uncertainties and unexpected setbacks in research. Grad school was certainly not easy. Luckily, Prof. Harrison was there. His resourcefulness and expansive knowledge helped guide my studies; his considerate nature and warmth reassured me throughout that journey. I would like to thank him for not only his help in research, but also in personal support.

As if grad school wasn't hard enough, COVID-19 came along. The last three years have felt like a blur. Although far away from family, I was fortunate to have friends at my side. I would like to thank my friends in the department for their company during my academic career. I'm grateful to have that support from people who understand the rigor of academia and navigating the professional world. Also, my roommates and their parents made me feel at home when it was so far away; I would like to thank them for that.

I appreciate the upper years in the Harrison lab, for giving me guidance not only in research and professional development but also in life. Also, I'm grateful to the lower years for keeping me company, having valuable discussions, helping me when in need, and keeping me sane in adverse situations.

Of course, I would like to thank my mom, for her long support of me studying abroad, before and during grad school.

Lastly, probably not a lot of people do this, but I want to say “thank you” to my younger self. It took a lot of tenacity and courage to see this through. The me now probably could not do it again.

Love,

Xander

Abstract

Steam reforming is one of the most important industrial chemical processes. However, it is usually performed in large-scale reactors and has high energy demand. Catalytic partial oxidation of methane, on the other hand, can be carried out in compact and low capital-cost reactors to produce syngas. Rh is generally considered the best metal catalyst for partial oxidation.

Effusive molecular beam experiments were used to measure CH_4 and C_2H_6 dissociative sticking coefficients, $S(T_g, T_s ;\vartheta)$ on a Rh(111) crystal, for which the impinging gas temperature, T_g, and surface temperature, T_s, could be independently varied, along with the angle of incidence, ϑ, of the impinging gas. The 500 – 900 K temperature range explored is relevant to heterogeneous catalytic processes such as methane partial oxidation. A dynamically biased precursor mediated microcanonical trapping (PMMT) model of dissociative chemisorption was used to analyze the experimental results. Modelling indicates that unlike on the Pt (111) surface where (111) terrace site reactivity dominates, methane reactivity on Rh (111) indicates that Rh step sites are not easily poisoned by C accumulation and can contribute substantially to the overall methane reactivity, especially at lower temperatures. Threshold energies for dissociative chemisorption on the terraces and steps sites were optimally modeled as 74.3 kJ/mol and 36.7 kJ/mol. Translations parallel to the surface and rotations were treated as spectator degrees of freedoms. The efficacy of vibrational energy to promote reactivity relative to normal translational energy was η_v=0.55 and one surface oscillator participated in energy exchange within the collisionally formed precursor complexes. A two-channel Arrhenius

model restricted to only the thermal dissociative sticking coefficient measured along the direction of surface normal, $S_n(T=T_g=T_s)$, yielded apparent activation energies of 70.6 and 25.5 kJ/mol which could be attributed to terrace and step sites, respectively. Such multidimensional reactivity studies allow for relatively facile designation of the terrace and step activity which allows us to reconcile single crystal and Rh foil reactivity studies. PMMT modeling of the step site reactivity on Rh(111) could be extrapolated to replicate the thermal dissociative sticking coefficient of the "defect dominated" Rh film surfaces measured by Ehrlich at temperatures in the 250 -350 K range where much of the elevated kinetic isotope effect (9 to 15) could be attributed to quantum mechanical tunneling through the reactive barrier.

In ethane dosing experiments, it is discovered that carbon migration happens at a significant rate at 900 K and carbon segregation in each direct would interfere with sticking coefficient measurements. C2 species might favor the formation of polymeric C or graphene on the surface which was not observed for methane, which may further complicate carbon behavior on Rh(111) surface.

Table of Contents

1 Introduction

1.1 Purpose

For a chemical reaction to happen, the reactants need a minimum energy to overcome an energy barrier. The presence of catalyst, in most cases, can reduce this energy barrier hence increasing the rate of chemical reactions. Catalytic process is ubiquitous in chemical industry. Today, over 90% of all industrial chemicals are produced with the aid of catalysts.[1] Catalysis can be classified into three categories: heterogeneous catalysis, homogeneous catalysis, and enzyme catalysis. In homogeneous catalysis, reactants, products, and catalysts are all in the same phase whereas in heterogeneous catalysis, the catalysts (usually in solid phase) and reagents (usually in gas or liquid phase) are in the different phases. The chemical industry has often favored heterogeneous catalysis, because in homogeneous reactions, product separation and catalyst retention are more difficult and expensive.

The majority of industrial processes occur over transition metal catalysts at high temperature and pressure. Although the catalysts, reaction conditions, and products were well studied for these processes, the detailed mechanism of individual catalytic steps is complicated by high pressure and the different sites on the catalysts. Take for example the industrial process of producing hydrogen, steam reforming of methane, the rate-determining step is believed to be the activated dissociative chemisorption of methane. In this lab, we study gas-surface reaction in ultrahigh vacuum on single crystal surfaces where the gas molecules are well characterized, and active site presents is well controlled in the hope to develop a predictive understanding of gas-surface reactions.

Heterogeneous catalysis plays a direct or indirect role in our lives daily, from fertilizers to plastics to medicines. For example, about half of the population were fed by the ammonia produced by Haber-Bosch process.[2] Some of the processes are in incredibly large scale and consumes significant amount of energy.

Reaction	Catalytic system
Ammonia synthesis from N_2 and H_2[3-4]	Fe, Ru
Ammonia oxidation to NO and HNO_3	Pt-Rh
Reduction of NO_x in exhaust	Rh, vanadium oxide
Catalytic cracking of crude oil	Zeolites
Oxidation of CO and hydrocarbons in car exhaust	Pt, Pd
Methanation	Ni
Steam reforming of methane to syngas	Ni
Vinyl chloride (ethylene + Cl_2)	Cu (as chloride)
Reforming of naphtha to gasoline	Pt, Pt-Re, Pt-Ir
Acrylonitrile from propylene and ammonia	Bi-Mo, Fe-Sb (Oxides)

Table 1-1[5] Some common large-scale industrial processes involving heterogeneous catalysis

Take ammonia synthesis as an example, approximately 120 million tons of ammonia are synthesized annually using the Haber-Bosch process, consuming 29 gigajoules of energy per ton of ammonia synthesized.[6] While nitrogen can be obtained by separation of air, the other ingredients for the reaction, hydrogen, has to be synthesized by other means. Approximately half of the global hydrogen production (20 Mt) is from steam reforming of

natural gas.[7] This is yet another energy-heavy process, consuming 12.6 GJ per ton hydrogen produced. Steam reforming also produces CO, along with H_2, to make synthesis gas, which can subsequently be turned into large hydrocarbons such as synthetic fuels, and olefins via the Fischer-Tropsch process. Other common product from natural gas includes fabrics, glass, steel, and plastics. Overall, converting natural gas to other products accounts for 2% of the total global energy consumption. All of these processes depend in part on the interaction of small alkanes with transition metal surfaces, and the rate determining step is the first C-H bond cleavage at the surface to form alkyl and hydrogen on the surface. Hence, revelation of reaction kinetics and dynamics may offer an important additional control element in the design and optimization of future green catalysts and catalytic pathways. One of the most promising ways of improving energy efficiency in natural gas processing is by partial oxidation of alkanes ($C_nH_{2n+2} + O_2 \rightarrow CO + H_2$). Schmidt showed that partial oxidation is possible on platinum and rhodium surfaces in metal coated ceramic monoliths at reaction times as short as 10^{-3} seconds.[8-9] However, there was no single crystal study of CH_4/Rh(111) dissociative chemisorption in the literature. In this lab, using effusive beam technique, we were able to measure the sticking coefficient of light alkanes, providing an in-depth view of alkane activation mechanism on Rh(111) surface.

1.2 Rhodium Catalysts

Rhodium is one of the precious metals in the platinum group. It is the rarest naturally occurring stable element in earth's crust[10-12] (some sources list Re as rarest with Rh being the second) and often the most expensive one (in 2022, $442k per kg[13], in comparison, gold is $62k per kg[14]). It is an exceptional catalyst for car exhaust removal and partial oxidation of alkanes.

In 1991, 87% of the world Rh production went to three-way-catalytic (TWC) converters in cars[15]; the number remained high in 2018, at 85%[16]. The advantages of three-way-catalytic converters is that they convert three of the pollutants in car exhaust, namely NO_x, CO, and hydrocarbons, into CO_2, H_2O, and N_2; whereas the old "two-way" catalytic converters only convert CO and hydrocarbons into CO_2 and H_2O. Since its widespread application in 1979, Rh has been the most important component of TWCs for numerous reasons. It is discovered that Rh has high activity and selectivity for NO reduction to N_2 and high stability in harsh environments. The uniquely high selectivity that's different from other noble metals may be from the ability to promote N-pairing in adsorbed NO molecules before the N-O bond is broken. Rh catalysts need to work in an operational "window" to convert combustion mixture stoichiometrically to benign exhaust (figure 1-1). Within the narrow range around the stoichiometric air/fuel mixture, it is possible to simultaneously react more than 90% of all three pollutants. If there's excess oxygen, the system behaves as a typical oxidation catalyst, removing all the reducing species while keeping the NO.[15]

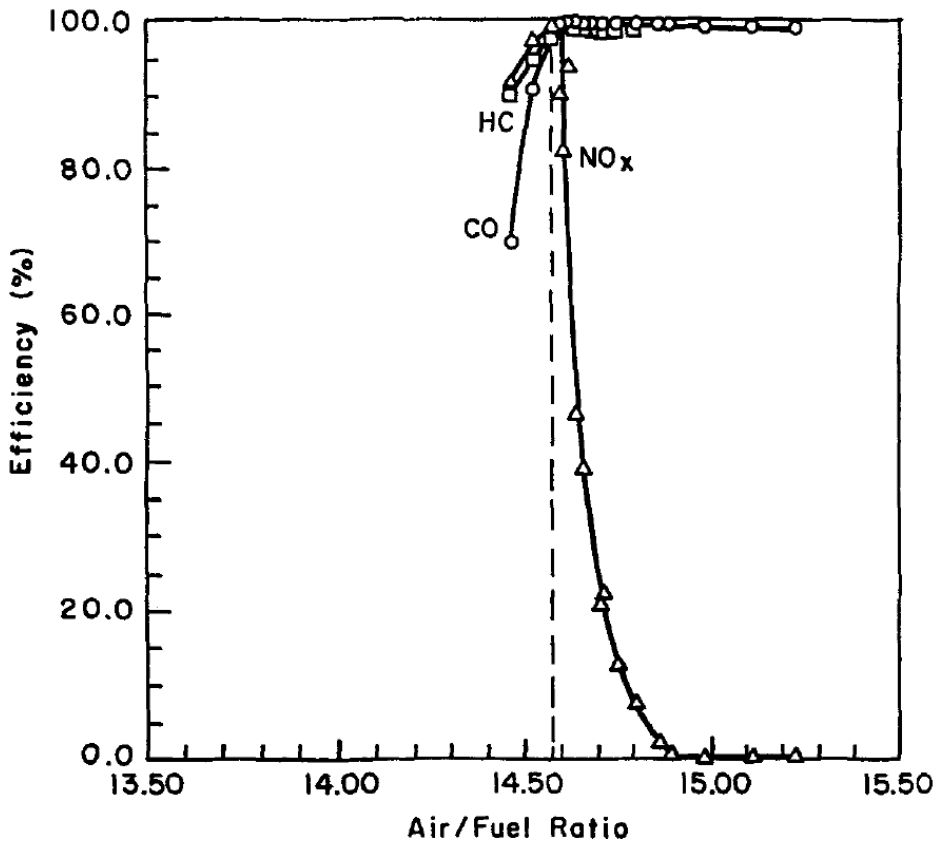

Figure 1-1[15] Operational "window" of Rh-containing TWC

Attempts to find a replacement for Rh in TWCs aiming to reduce the cost and improve performance. The metallic active component most mentioned to replace Rh in TWCs is Pd. Although Pd deactivates by Pb in the gasoline easily, gasoline nowadays in the US market is essentially Pb-free. There are also attempts using Pd and rare earth metal oxides to overcome the deficiencies of Rh catalysts (narrow operating window). Another metal that exhibits similar behavior to that of Rh is molybdenum. With a large excess of molybdenum, 15-20 wt%, covering the entire surface of alumina support, TWC-like behavior can be achieved. However, because that sulfur oxides in exhaust are strong poisons for molybdenum, and that molybdenum and tungsten oxyhydroxides creates extra emissions, Mo catalysts are not practical in use.[15]

Other than being an important composition in catalytic converters, Rh is also a great catalyst for partial oxidation (CPO) of alkanes.

$$CH_4 + \frac{1}{2}O_2 \rightarrow CO + 2H_2 \quad \Delta H = -36\ kJ/mol$$

Compared to traditional way, steam reforming, of making syngas:

$$CH_4 + H_2O \rightarrow CO + 3H_2 \quad \Delta H = 206\ kJ/mol$$

CPO has several advantages: first, it is exothermic, so no external energy is needed once the reaction is initiated; second, it doesn't require large-scale plants, can be carried out at short contact times (10^{-2} to 10^{-4} s) in small autothermal reactor configurations; third, it has high selectivity (>90%) towards H_2 and CO. Supported Rh and Pt metal catalysts can achieve optimal performance without carbon formation.[17]

Industrial acetic acid production, Monsanto process, also utilizes Rh as the catalyst. Methanol and carbon monoxide are used, through methanol carbonylation, to produce acetic acid.

$$CH_3OH + CO \xrightarrow{catalyst} CH_3COOH$$

However, this process is a homogeneous process with Rh coordination compound as catalyst.

Ostwald process is another heterogeneous process that uses Rh. Nitric oxide is produced by oxidation of ammonia and is subsequently oxidized to make nitric acid.

$$4NH_3 + O_2 \rightarrow 4NO + 6H_2O$$

$$2NO + O_2 \rightarrow 2NO_2$$

$$3NO_2 + H_2O \rightarrow 2HNO_3 + NO$$

1.3 Dissociative Sticking Coefficient Studies

When a molecule hits a surface, it either bounces away or adsorb onto the surface. The adsorption has two forms: physisorption and chemisorption. In chemisorption, a molecule could either form chemical bond as a whole with the surface (such as CO chemisorbs on transition metals) or it could dissociatively adsorb, forming two or more fragments bonding to the surface. The ratio of the number of molecules that adsorb to a surface to the total number of molecules that impinge the surface is called the sticking coefficient; for the case of dissociative adsorption, the ratio is called the dissociative sticking coefficient (DSC). There have been several techniques developed to measure DSCs.

1.3.1 Thermal Bulb

The thermal bulb technique is by far the simplest technique to measure DSCs. In thermal bulb experiments, gas is introduced into a vacuum chamber as ambient gas. When the surface temperature is different than the chamber temperature, the ambient pressure needs to be sufficiently high (> 3 torr) for the mean free path of the molecules to be short enough so that the gas molecules above the crystal surface can reach thermal equilibrium with the crystal. After a period of time, the chamber is evacuated and the absorbed species is measured. Because the pressure is high, the impinging flux is so high that only low DSCs ($<10^{-8}$) can be measured, otherwise the dosing time would be impractically short. To circumvent this, experiments can be done with massive pumping speed in order to maintain a short dosing time. Generally, the reactant gas was admitted into the chamber while the

crystal is cold, then the crystal is heated to the desired temperature rapidly. Once the desired dosing time is reached, valves are open to allow gas to be removed promptly.

Even with massive pumping speed and short dosing time, the > 3 torr high pressure requirement still limits the accuracy of the DSCs measured. An alternative way is to dilute the reactive gas with inert reagent such as argon or nitrogen. The high pressure in the chamber makes it possible for gas reaching equilibrium with the heated surface, the low partial pressure of the reactive gas ensured that dosing time does not need to be unpractically short.

However, reaching thermal equilibrium between the gas and the heated surface is difficult and unreliable even with the two methods mentioned above. A few methods were thus developed to prepare the gas in a valved section whose temperature can be controlled before admitting into the main chamber to react with the surface.[18-24] The valved section was either heated or cooled to the desired temperature then the gas was admitted into the valved section and allowed to thermalize. Once the gas is fully thermalized with the valved section, the valve is opened and allows gas to react with the substrate. The substrate and the main chamber could also be heated or cooled to the same temperature as the valved section to allow for measurements at equilibrium conditions. Because the whole chamber needs to be heated or cooled, the temperature can only be within a range near room temperature (-40 to 80 °C). High temperature experiments common in molecular beam experiments (above 500 K) are not possible. However, this bulb technique does allow for equilibrium measurements below room temperature, which is difficult for modern molecular beam experiments to achieve. Using this method, Brass and Ehrlich measured the methane dissociative sticking coefficient on an evaporated Rh thin film on Pyrex glass

vessel.[18, 20-21] The sticking coefficients were found to be in the range of 10^{-6} – 10^{-8} in the temperature range 80 to -40 °C. The activation energy was determined for CH_4 and all its deuterated forms, with CH_4 being 20.9 kJ/mol and CD_4 being 26.0 kJ/mol.

1.3.2 Supersonic Beam

Thermal bulb experiments, limited by their own design, can only provide so much information on kinetics. Supersonic beams are directional, and provide great control over the flux and energy distribution of the reactants. Basic non-equilibrium kinetics data, including activation energies and preexponential factors can be measured by supersonic beam experiments as a function of surface coverage, surface temperature, and beam energy and direction. [25-26] However, connecting such non-equilibrium kinetics information to transition state properties and thermal equilibrium rate constants can be difficult.

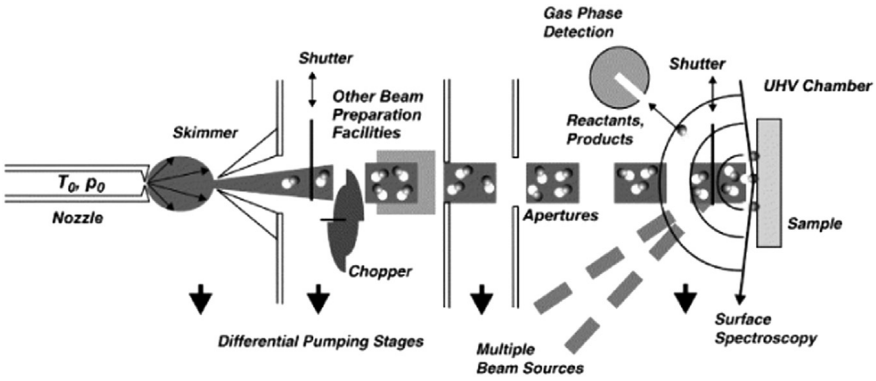

Figure 1-2 Schematic representation of a typical supersonic molecular beam instrument.[27-28]

In a typical supersonic beam setup, high pressure gas exits through a small hole in a heated nozzle into high vacuum, differentially pumped regions separated by skimmers and small orifices, before reaching the UHV chamber where gas-surface reaction occurs. This results in a highly collimated beam of molecules. Because of the substantial pressure difference between the nozzle and the source high vacuum region, the gas undergoes a

supersonic expansion. Collisional buffeting during supersonic expansion cools the relative translational motion amongst molecules in the beam. Translational to rotational energy transfer is highly efficient, thus the supersonic expansion also cools the beam molecules rotation temperature. On the other hand, translational to vibrational energy transfer is far less efficient, particularly for small molecules with high frequency modes. Because of this, vibrations are not cooled in a supersonic expansion for small molecules such as methane, but for bigger alkanes, vibrational cooling can be significant. The translational energy of molecules in a supersonic beam can be described as relatively narrow and can be tuned by varying the nozzle temperature or by "seeding" the molecules of interest in inert carrier gases of different mass (e.g., 1% alkane in 99% He). In summary, the supersonic molecular beam is a well-collimated beam with a narrow translational energy distribution whose translational temperature relative to the mean stream velocity of the beam molecules is close to 10 K.

The most common method to study adsorption is the King and Wells method. It is widely used to measure the sticking coefficient of species. Supersonic beams allow for studies of sticking coefficients dependence on kinetic energy and on the angle of incidence of the incoming molecules; it also makes possible the studies of molecular quantum state, such as electronic, vibrational, and rotational state of the molecules. In King and Wells method, the partial pressure of the desired gas species is monitored as a function of time by a quadrupole mass spectrometer (QMS). There are two shutters intercepting the beam, shutter 1 in the differential pumping stage, and shutter 2 just in front of the sample. When the beam is turned on and shutter 1 is close, QMS measures a background pressure P_0 of the studied species in the main chamber. When shutter 1 is turned down, the beam enters

the main chamber causing an increase in the partial pressure measured by the QMS. When both the beam flux and the overall pumping speed are constant, the main chamber should maintain a constant pressure P_1. Shutter 2 intercepts the beam and prevents it from striking the surface of the sample and it needs to be inert. When shutter 2 is removed from the beam path, the beam strikes the sample surface and if adsorption happens, a drop in pressure ΔP can be measured. The relative decrease of the QMS signal is the absolute sticking coefficient: $S = \frac{\Delta P}{P_1 - P_0}$. The sensitivity of the methods is determined by the QMS signal to noise ratio and by the stability in time and intensity of the beam. Due to the limit of this, only relatively high DSCs (>10^{-2}) can be measured with King and Wells method.

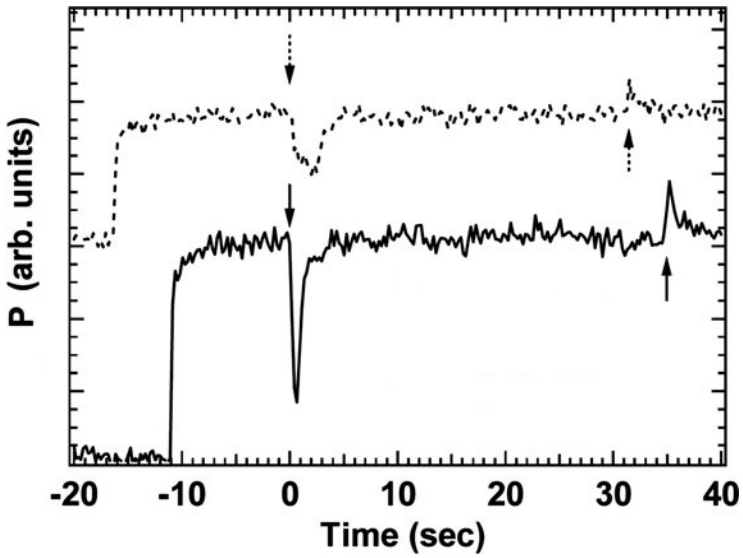

Figure 1-3 QMS signals for King and Wells method.[29] Down arrows indicate the removal of shutter 2.

Supersonic beams provide a high-density and collision-free source of incident reactant molecules with a well-defined and narrow range of velocities.[30-34] Coupled with lasers, incident reactant molecules can be state-specifically prepared and the molecules scattered from the surface can be state resolved detected. By exciting different vibrational

modes then measuring the change in DSCs, it is possible to understand how vibration affects reactivity. By comparing the difference in DSCs made by different translational and vibrational energies, the efficacy of vibrational energy in promoting the reaction with respect to translational energy along the surface normal could be determined.

It is worth noting that in supersonic beam studies, nonthermal high-energy molecules only represent a small fraction of the gas molecules in typical catalytic mixtures (high-energy tail of the Boltzmann distribution). Because of this, the results may not adequately reflect the chemistry observed in other more typical environments.

1.3.3 Effusive Beam

Because of the complications involved with supersonic beams, effusive beams may be used for kinetic studies to more closely simulate the conditions of typical reaction conditions in catalysis, film deposition, and other practical applications.[25] Different from supersonic beam setup that involves multiple pumping stages, effusive beam has a relatively simple setup. It essentially consists of a tube that's capable of being heated to desired temperatures with an orifice that emits gas. The diameter of the tube needs to be smaller than the mean free path of the gas feeding into it in order to maintain a molecular flow, considering the low pressure (0.2 torr max) in the gas line, this is easy to achieve. Because gases are in molecular flow, there is no collision amongst the gas stream, hence no supersonic cooling effect. This allows each degree of freedom to be thermalized to the nozzle temperature, $T_g = T_{rans} = T_{vib} = T_{rot} = T_{nozzle}$, resulting in a well-characterized beam. King and Wells method can also be used in effusive beam experiments to measure dissociative sticking coefficients, but typically only for DSCs greater than ~0.01.[35] An alternative approach, used by this lab, which measures the species left on the surface and

dosage on the surface from pumping speed, pressure, and the geometry of the chamber can be used to determine DSCs as small as 10^{-6}.

When the wall of the orifice is infinitely thin, the effusive beam emitted will have a cosine angular flux distribution. The cosine flux angular distribution in the three-dimensional space projects onto a two-dimensional plane, resulting in a $cos^4\vartheta$ distribution of flux across the surface. In this case, the translational energy along the surface normal, $E_n = E_t \cos^2 \vartheta$, has a $cos^2\vartheta$ dependence whereas the vibrational and rotational energies remain the same. This allows for the studies of angle-resolved DSCs. This can only be realized by measuring the species left on the surface at different locations (corresponding to different ϑ), which is not possible with King and Wells method.

In effusive beam studies, similar to supersonic beam, the sticking coefficient measured when the gas molecules strike the surface directly from the doser is called **direct sticking coefficient**, $S(T_g, T_s, \vartheta)$; the special case, direct sticking coefficient along the surface normal $S_n(T_g, T_s)$, is when the gas molecules strike the surface along the surface normal. The temperature of the doser and the crystal can be controlled independently, either equilibrium, $S(T_g=T_s)$ or non-equilibrium, $S(T_g\neq T_s)$, DSCs can be determined. When the gas molecules that strike the surface are not directly from the doser, such as the scattered gas that has hit the chamber wall and thermalized to the chamber temperature, a **background sticking coefficient**, $S_{bkg}(T_c, T_s)$, can be determined. Since the molecules that hit the surface come from different angles, background sticking coefficient is not angle dependent. Because the chamber cannot be heated to a desired temperature precisely, background sticking coefficient measurement is limited to when the gas temperature is the chamber temperature, typically 297K. The thermal equilibrium DSC is available by

integrating the angle-resolved S(T, ϑ) measurements over the cosine angular distribution of the incoming flux under thermal equilibrium conditions,

$$S(T) = \int S(\mathrm{T}, \vartheta) \frac{\cos}{\pi} d\Omega$$

This kind of direct connection to the reactivity relevant to high pressure thermal catalysis is missing for non-equilibrium and vibrationally ambiguous supersonic beam experiments.

1.4 Outlook

Reaction energetics have always been a focus of catalyst design. However, we have shown that dynamical biases in gas-surface reactivity can alter the reactivity by orders of magnitude as compared to statistical expectations. The effects of dynamics for H_2 on Cu(111)[36] and for CH_4 on Pt(111)[37] are equivalent to changes in activation barriers by 27 kJ/mol and 13 kJ/mol at 700K, respectively. This indicates that dynamics, as well as reaction energetics, should be crucial considerations in the design of catalysts and catalytic processes. Surprisingly, there is little experimental information about the underlying dynamics of reactions at surfaces that can modulate overall reaction rates. Modern electronic structure theory methods can provide information in both the shape (early/late position) of the transition state and the energetics of the transition state of a gas-surface reaction. However, the shape of the TS is not typically used as a control parameter in the search for new catalysts. We believe that improving understanding of the dynamics of gas-surface reactions could be transformative in catalyst design by providing new "dynamical" reaction rate control parameters based on transition state features other than the barrier energy alone. A long-term goal of this lab is to establish more robust connection between

experimental dynamics, transition state properties, and quantitative models of gas-surface reactivity. Ultimately, this would enable catalyst improvements through *in silico* screening of potential catalysts by purposefully optimizing their calculated transition state features separately, identified as controlling energetics *and* dynamics.

Furthermore, experimental results on single crystal surface provide useful models, benchmarks, and ideas for catalysis and electronic structure theory communities. Improving understanding of heterogeneous catalysis is challenging because of limited reliable experimental or theoretical information about reactivity at specific surface sites. DFT calculations of transition state activation energies vary substantially with choice of different functionals. Typical accuracies claimed are only ±30 kJ/mol. Moreover, DFT calculations are often done to model individual reactive steps at single crystal surfaces, but experimental evaluation of such DFT calculations is usually done by comparison of DFT-informed multi-step microkinetic models to an overall thermal rate constant observed on nanocatalysts, rather than on the single crystals originally modeled. There have been several DFT studies[6, 38-41] on CH_4/Rh(111) yet no direct single crystal experiments. The work done in this thesis on activated gas-surface reactions makes direct comparison between theory and experiments possible for structurally well-defined reactions where the reagents can be brought together with well-defined non-equilibrium or thermal states. The experimentally extracted d-PMMT model transition state parameters can also be used to find correlations between DFT-calculated transition state properties.

In this thesis, an effusive molecular beam technique was used to measure light alkane dissociative sticking coefficients, $S(T_g, T_s, \vartheta)$, on a Rh(111) surface. The impinging gas temperature T_g, the surface temperature T_s, and the impinging angle ϑ were well defined

and independently varied. Chapter 2 discusses the instrumental setup and experimental detail. Chapter 3 discusses methane dissociation on Rh(111). The unusually high sticking coefficient observed at low temperature (below 500K) led to the discovery of active step sites that remain active even when the accumulated surface carbon coverage is much higher than the surface step density. This revealed that even on Rh(111), a nominally perfect single crystal surface, small amounts of imperfect defect sites play a significant role in dictating the observed reactivity. The two different reactivity domains attributed to terrace sites at high temperatures and step sites at low temperatures helped close discrepancies between previous methane/Rh experimental and theoretical research. Chapter 4 discusses ethane dissociation on Rh(111). The high activation energy at high temperature (above 700 K) led to the discovery of carbon migration on Rh. The migration seems to be complicated by the carbon bulk concentration and surface species. Improved attention to the kinetics of cleaning and annealing processes prior to experiments and extended monitoring of carbon coverage may be needed to better understand the ethane/Rh(111) system.

Reference

1. Armor, J. N., A History of Industrial Catalysis. *Catal Today* **2011**, *163*, 3-9.
2. Erisman, J. W.; Sutton, M. A.; Galloway, J.; Klimont, Z.; Winiwarter, W., How a Century of Ammonia Synthesis Changed the World. *Nature Geoscience* **2008**, *1*, 636-639.
3. Palma, V.; Ruocco, C.; Martino, M.; Meloni, E.; Ricca, A., 7 - Catalysts for Conversion of Synthesis Gas. In *Bioenergy Systems for the Future*, Dalena, F.; Basile, A.; Rossi, C., Eds. Woodhead Publishing: 2017; pp 217-277.
4. Ross, J. R. H., Chapter 1 - an Introduction to Heterogeneous Catalysis and Its Development through the Centuries—Chemistry in Two Dimensions. In *Contemporary Catalysis*, Ross, J. R. H., Ed. Elsevier: Amsterdam, 2019; pp 3-38.
5. Kakaei, K.; Esrafili, M. D.; Ehsani, A., Chapter 1 - Introduction to Catalysis. In *Interface Science and Technology*, Kakaei, K.; Esrafili, M. D.; Ehsani, A., Eds. Elsevier: 2019; Vol. 27, pp 1-21.
6. Fechete, I.; Wang, Y.; Vedrine, J. C., The Past, Present and Future of Heterogeneous Catalysis. *Catal Today* **2012**, *189*, 2-27.
7. Kalamaras, C. M.; Efstathiou, A. M. In *Hydrogen Production Technologies: Current State and Future Developments*, Conference papers in science, Hindawi: 2013.
8. Hickman, D. A.; Schmidt, L. D., Production of Syngas by Direct Catalytic-Oxidation of Methane. *Science* **1993**, *259*, 343-346.
9. Goetsch, D. A.; Schmidt, L. D., Microsecond Catalytic Partial Oxidation of Alkanes. *Science* **1996**, *271*, 1560-1562.
10. Haynes, W. M.; Lide, D. R.; Bruno, T. J., Crc Handbook of Chemistry and Physics. CRC press: 2016; pp 14-18.
11. Chemical Elements Abundance in Earth's Crust. https://www.webelements.com/periodicity/abund_crust/ (accessed July 11th 2022).
12. Barbalace, K. https://environmentalchemistry.com/yogi/periodic/ (accessed July 11th 2022).
13. Platinum Group Metals. https://mineralprices.com/platinum-group-metals/ (accessed July 5th 2022).
14. Precious Metals. https://mineralprices.com/precious-metals/ (accessed July 5th 2022).
15. Shelef, M.; Graham, G. W., Why Rhodium in Automotive Three-Way Catalysts? *Catalysis Reviews* **1994**, *36*, 433-457.
16. Singerling, S. A.; Schulte, R. F., Minerals Yearbook Platinum-Group Metals. 2018.
17. Michael, B. C.; Donazzi, A.; Schmidt, L. D., Effects of H2o and Co2 Addition in Catalytic Partial Oxidation of Methane on Rh. *J Catal* **2009**, *265*, 117-129.
18. Brass, S. G.; Ehrlich, G., Internal Molecular Motions and Activated Chemisorption - Ch4 on Rhodium. *J Chem Phys* **1987**, *87*, 4285-4293.
19. Brass, S. G.; Ehrlich, G., Activated Chemisorption of Ch4 and Internal Molecular Motions. *Surf Sci* **1987**, *191*, L819-L824.
20. Brass, S. G.; Ehrlich, G., Dissociative and Molecular Adsorption of Methane on Rhodium. *Surf Sci* **1987**, *187*, 21-35.
21. Stewart, C. N.; Ehrlich, G., Dynamics of Activated Chemisorption - Methane on Rhodium. *J Chem Phys* **1975**, *62*, 4672-4682.
22. Brass, S. G.; Reed, D. A.; Ehrlich, G., Vibrational-Excitation and Surface Reactivity - Examination of the Nu-3 and 2nu-3 Modes of Ch4. *J Chem Phys* **1979**, *70*, 5244-5250.
23. Stewart, C. N.; Ehrlich, G., Activated Chemisorption of Molecules. *Chem Phys Lett* **1972**, *16*, 203-&.
24. Yates, J. T.; Zinck, J. J.; Sheard, S.; Weinberg, W. H., Search for Vibrational Activation in the Chemisorption of Methane. *J Chem Phys* **1979**, *70*, 2266-2272.

25. Zaera, F., 7.03 - Kinetics on Model Systems. In *Comprehensive Inorganic Chemistry Ii (Second Edition)*, Reedijk, J.; Poeppelmeier, K., Eds. Elsevier: Amsterdam, 2013; pp 39-74.
26. Vattuone, L.; Bracco, G.; Smerieri, M.; Savio, L.; Rocca, M., Supersonic Molecular Beams Studies of Surfaces. In *Dynamics of Gas-Surface Interactions: Atomic-Level Understanding of Scattering Processes at Surfaces*, Díez Muiño, R.; Busnengo, H. F., Eds. Springer Berlin Heidelberg: Berlin, Heidelberg, 2013; pp 1-23.
27. Libuda, J., Reaction Kinetics on Model Catalysts: Molecular Beam Methods and Time-Resolved Vibrational Spectroscopy. *Surf Sci* **2005**, *587*, 55-68.
28. Libuda, J.; Freund, H. J., Molecular Beam Experiments on Model Catalysts. *Surf Sci Rep* **2005**, *57*, 157-298.
29. Vattuone, L.; Savio, L.; Rocca, M., Coverage Dependence of the Dynamics of Ethylene Adsorption on Ag(210). *Journal of Physics: Condensed Matter* **2004**, *16*, S2929-S2936.
30. Beck, R. D.; Utz, A. L., Quantum-State Resolved Gas/Surface Reaction Dynamics Experiments. In *Dynamics of Gas-Surface Interactions*, Springer: 2013; pp 179-212.
31. Ueta, H.; Chen, L.; Beck, R. D.; Colón-Dìaz, I.; Jackson, B., Quantum State-Resolved Ch 4 Dissociation on Pt (111): Coverage Dependent Barrier Heights from Experiment and Density Functional Theory. *Phys. Chem. Chem. Phys.* **2013**, *15*, 20526-20535.
32. Chen, L.; Ueta, H.; Bisson, R.; Beck, R. D., Quantum State-Resolved Gas/Surface Reaction Dynamics Probed by Reflection Absorption Infrared Spectroscopy. *Rev Sci Instrum* **2013**, *84*, 053902.
33. Chadwick, H.; Beck, R. D., Quantum State–Resolved Studies of Chemisorption Reactions. *Annual Review of Physical Chemistry* **2017**, *68*, 39-61.
34. Chadwick, H.; Beck, R. D., Quantum State Resolved Gas–Surface Reaction Dynamics Experiments: A Tutorial Review. *Chem Soc Rev* **2016**, *45*, 3576-3594.
35. Bowker, M., The Molecular Beam Reactor. *Applied Catalysis A: General* **1997**, *160*, 89-98.
36. Donald, S. B.; Harrison, I., Rice-Ramsperger-Kassel-Marcus Simulation of Hydrogen Dissociation on Cu(111): Addressing Dynamical Biases, Surface Temperature, and Tunneling. *J Phys Chem C* **2014**, *118*, 320-337.
37. Donald, S. B.; Navin, J. K.; Harrison, I., Methane Dissociative Chemisorption and Detailed Balance on Pt(111): Dynamical Constraints and the Modest Influence of Tunneling. *J Chem Phys* **2013**, *139*, 214707.
38. Bunnik, B. S.; Kramer, G. J., Energetics of Methane Dissociative Adsorption on Rh{111} from Dft Calculations. *J Catal* **2006**, *242*, 309-318.
39. van Grootel, P. W.; van Santen, R. A.; Hensen, E. J. M., Methane Dissociation on High and Low Indices Rh Surfaces. *J Phys Chem C* **2011**, *115*, 13027-13034.
40. Zhu, T.; van Grootel, P. W.; Filot, I. A. W.; Sun, S.-G.; van Santen, R. A.; Hensen, E. J. M., Microkinetics of Steam Methane Reforming on Platinum and Rhodium Metal Surfaces. *J Catal* **2013**, *297*, 227-235.
41. Liu, Z. P.; Hu, P., General Rules for Predicting Where a Catalytic Reaction Should Occur on Metal Surfaces: A Density Functional Theory Study of C-H and C-O Bond Breaking/Making on Flat, Stepped, and Kinked Metal Surfaces. *J Am Chem Soc* **2003**, *125*, 1958-1967.

2 Experimental Methods

2.1 Instrumental Setup

An ultra-high vacuum (UHV) chamber (figure 2-1) equipped with Auger electron spectroscopy (AES), mass spectrometry, residual gas analysis (RGA), and an effusive molecular beam doser was used. A detailed description of the chamber is available elsewhere[1-3], and only a brief overview is provided here. A metal single crystal of normally 1 cm diameter and 2 mm thickness was attached to a mount located in the main chamber that allowed for cooling to 100K and heating to 1400K (Figure 2-4). The manipulator attached to the main chamber allows for movements of the crystal in x, y, z directions as well as the rotation of the crystal to various analytical positions (eg. AES, TPD) (Figure 2-2). Reagent gases are stored and prepared using a gas manifold separated by a series of valves from the main chamber (Figure 2-4). A twice differentially pumped quadrupole mass spectrometer chamber allows for quantitative, line of sight mass spectrometry experiments such as temperature programmed desorption (TPD).

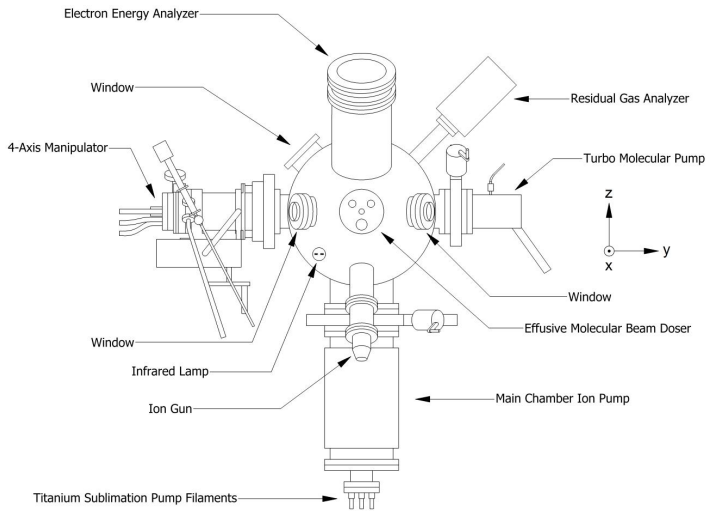

Figure 2-1 Schematic representation of the UHV chamber, adapted from Navin.[3]

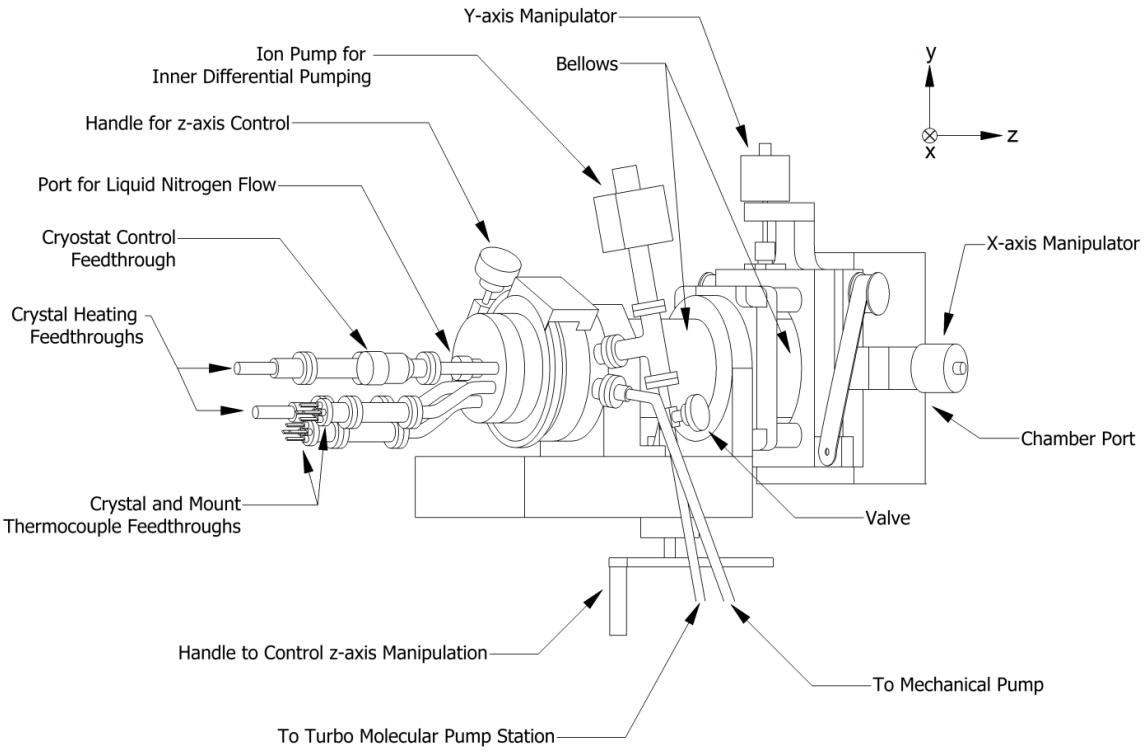

Figure 2-2 Schematic representation of 4-axis manipulator. Adapted from Navin.[3]

The main UHV chamber maintains a base pressure of 1×10^{-10} torr. The pressure within the chamber is measured using a 370 Stabil-Ion Bayard-Alpert gauge from Granville-Phillips. UHV conditions are achieved with a number of pumps: (i) a TMH-261 Pfeiffer turbo-molecular pump (TMP) with a nominal pumping speed of 210 L/s backed by an Edwards B2M5 mechanical pump that serves as a roughing pump on the exhaust side of the TMP; (ii) behind a gate valve, a double ended Physical Electronics ion pump with 210 L/s pumping speed with a Physical Electronics Boostivac titanium sublimation pump (TSP) inserted in the far end of the ion-pump.

The gas composition of the UHV chamber is measured using a Stanford Research System RGA 200 quadrupole mass spectrometer. The RGA 200 is also capable of measuring a single mass with respect to time which is useful for helium leak detection.

More quantitative mass spectrometry for temperature programmed desorption (TPD) is realized by an Extrel quadrupole mass spectrometer located within a twice differentially pumped region, pumped by dedicated ion pumps.

Gas reagents can be admitted into the main chamber by three different dosers: a variable leak valve from Duniway Stockrooms that controls the reagent gas pressure precisely within the chamber without changing the manifold pressure, an Accu-Low nitrogen calibrated leak (Model. CLO-7-3P-N2-100M-4FVCR-4MVCR-SP450, leak rate 8.15×10^{-4} L/s at 22.5°C) from Vacuum Technology Incorporated for measuring the pumping speed, and a heated effusive molecular beam doser which emits a cosine angular distribution of molecules for direct gas dosing.

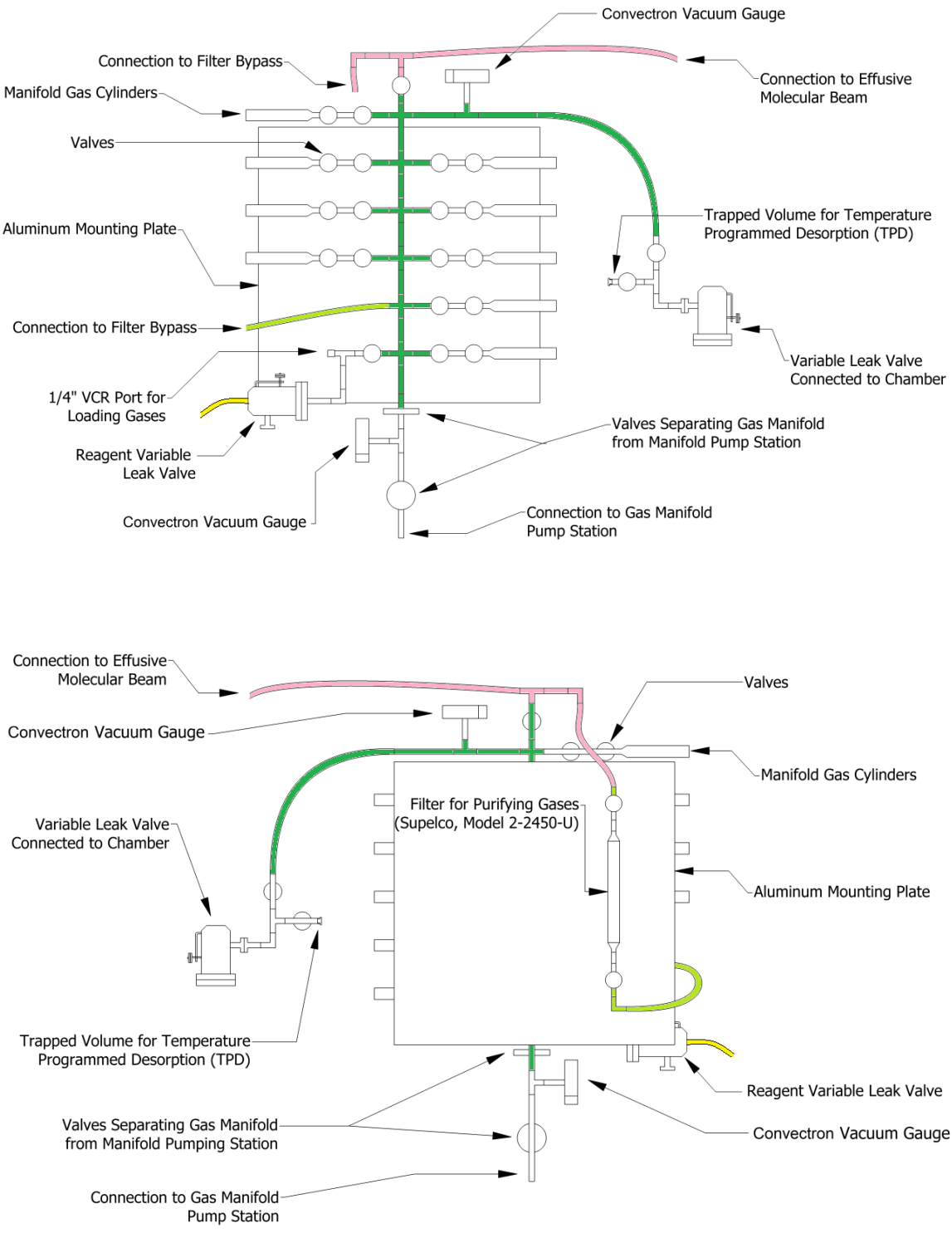

Figure 2-3 Schematic representation of gas manifold, top: front view, bottom: back view. Adapted from Navin.[3]

2.1.1 Rhodium crystal

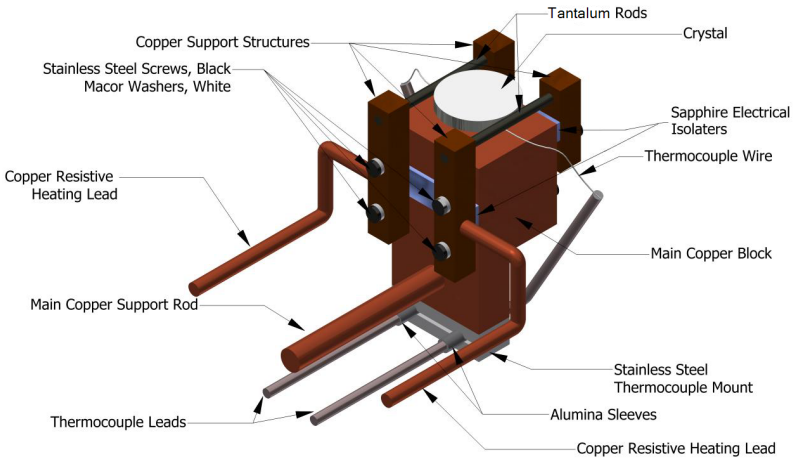

Figure 2-4 Schematic representation of crystal mount from the viewpoint of the manipulator. Adatped from Navin.[3]

The rhodium crystal used for this thesis has an 8mm diameter × 1.5 mm thickness with a surface cut to within 0.1º precision of the (111) surface. The crystal was obtained from Surface Preparation Laboratory from the Netherland with an elemental purity of 99.995%. As shown in Figure 2-1, the crystal mount is attached to the manipulator and cryostat cold finger by a large diameter copper rod at the base. Four rectangular copper support structures at each corner of the mount, separated from the copper bulk by insulating sapphire pieces, are secured in place with stainless steel screws and insulating Macor washers. Two 1 mm diameter tantalum rods are positioned in grooves on a pair of these copper supports and run parallel to the copper rod leading to the manipulator. The Rh crystal is spot welded to these rods for support and resistive heating. Two copper rods connect the support structures and the tantalum rods to the manipulator and allow a voltage for resistive heating between the tantalum rods and the crystal. Thermocouple leads are attached to a stainless steel structure at the base of the mount, which connects to

feedthroughs on the manipulator. Alumina sleeves insulate the thermocouple leads from the steel structure. The thermocouple wires extend up and are spot-welded together onto the side of the Rh crystal.

The area density of Rh(111) surface is calculated based on the atomic radius of Rh (r = 1.35×10^{-10} m) and the structure of fcc pack (lattice constant a=3.8034 Å[4]).

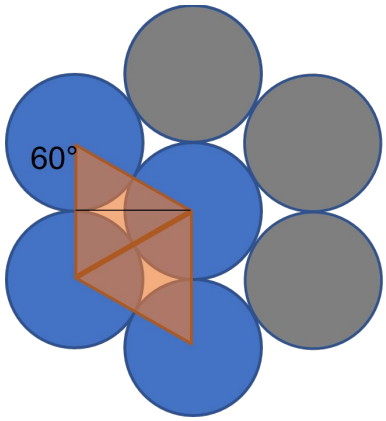

Figure 2-5 the 111 surface of an fcc crystal. The blue atoms are in the unit cell, which has a diamond shaped face. The length of the diamond is the diameter of Rh atom, hence the area of the cell is $d \times sin\,60 \times d = 2r \times \sqrt{3}r = 6.31 \times 10^{-20} m^2$. *Thus 1 m² of Rh(111) surface have* $\frac{1}{6.31 \times 10^{-20}} = 1.58 \times 10^{19}$ *unit cells, as there's* 1.58×10^{19} *rhodium atoms per meter squared.*

2.1.2 The distance between the doser and the crystal surface

The distance between the doser and the surface is needed in determining the flux ratio of direct flux and background flux, which is important in calculating the direct sticking coefficient; thus, it must be measured precisely. However, since the crystal surface normal and doser centerline are collinear and in the horizontal plane, there's only one orientation the distance could be measured: from the turbomolecular pump side. To measure the distance between the surface and the doser orifice, the turbomolecular pump needs to be

dismounted while the manipulator of the crystal and the doser are in the experimental dosing position. A Brunson model 82852 alignment telescope is used to measure the dosing distance. First, the crystal is placed in front of the doser in a dosing position. Second, align the cross in the telescope's view window with the crystal's surface, fix the telescope as a reference point. Then the crystal is moved away to leave room for the doser. Lastly, move the doser by rotating its manipulator until the center of the doser align with the reference point in the telescope's view window. The distance moved by the doser, read by the ruler besides the bellow, is the distance between the doser and the crystal. It was determined that when the doser's manipulator position is at 1.85 cm (read on the ruler by the bellow) and the crystal's manipulator position is at 0.4500 inches (read on the x-axis on the nob), the distance between the orifice and the surface is 1.00 cm. The distance can be changed by either moving the doser or the crystal. In practice, it is easier to move the doser so that the crystal does not need to be moved back and forth for dosing and AES scan.

2.1.3 Gas preparation

Methane (PRAXAIR (ME 5.0RS), purity 99.999%) and ethane (Matheson Tri-Gas (RES), purity 99.995%) are admitted into the chamber through a Supelpre-O Oxygen/Moisture trap (22450-U) filter.[5-6] The filter is capable of removing O_2, H_2O, CO_2, CO, NH_3, alcohols, alkanes, alkenes, amines, aromatics, diethylether, halogen, and sulfers from He, H_2, N_2, Ar, and CH_4.

To test the effectiveness of the filter, approximately 0.1 torr of methane was released into the gas manifold, then approximately 0.02 torr of CO was released into the manifold and the mixture was admitted into the main chamber and analyzed in RGA. Then the mixture of the gas was fed into the gas line through the filter, and the filtered gas was

analyzed again in RGA. Compared to the CO/methane mixture before going through the filter, CO level was reduced to the same level as that of pure methane, which indicated that the filter is effective in removing CO.

Although not stated in the Supelco filter manual, experiments showed that the filter does not absorb ethane. In an experiment, approximately 0.1 torr of ethane was released into the gas manifold, then the valve separating the filter and the gas manifold was opened to let ethane contact the filter. The pressure rose to a limiting value in one to two minutes and remain constant for a couple of hours, which indicates that the filter is not absorbing ethane from the manifold. The RGA spectra of before and after the filter were also compared and shows no difference, indicating that the filter does not crack ethane either. In comparison, when oxygen or CO is released in the manifold then contact the filter, the pressure in the manifold will decrease until it reaches 0, which indicates that the filter is effective in removing oxygen or CO.

2.2 Analytical Methods

2.2.1 Auger electron spectroscopy (AES) theory

Auger electron spectroscopy (AES) is used to analyze the elemental composition of a surface. AES works on the basis of interaction of an electron beam with the core electrons of an atom. When a high energy electron, typically 3000 eV in our AES measurements, collides with an atom, a core electron can be ejected from the atom leaving an electron vacancy. To maintain the stability of the atom, an electron from a higher energy level of the atom relaxes to fill the vacancy. The energy released by this process transfers to another electron in a different energy level, causing it to eject as a secondary electron, which is known as the Auger electron. The energy of an Auger electron is element specific, and

does not depend on the chemical environment or the energy of the electron beam. However, some elements have similar Auger electron energies, when the energy gaps between pairs of electron energy levels are similar. Additionally, AES can only be used to probe to a depth of 4 – 50 Å[7], after that the mean free path of Auger electrons is too short to exit the bulk and reach the electron analyzer without losing energy.

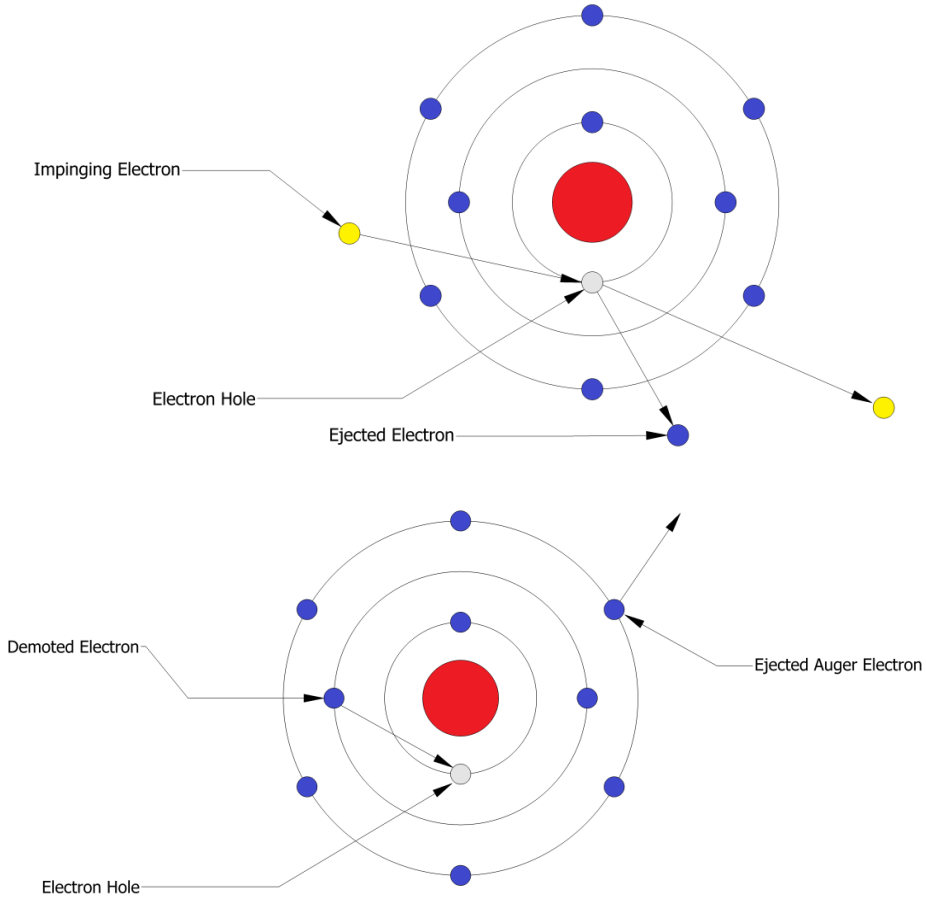

Figure 2-6 Schematic representation of Auger process. Adapted from Navin[3].

On rhodium, the area that is hit by the electron beam in AES gives off a blue fluorescence, which can be used as an indication of the position of the area probed. This is not observed from Pt surfaces.

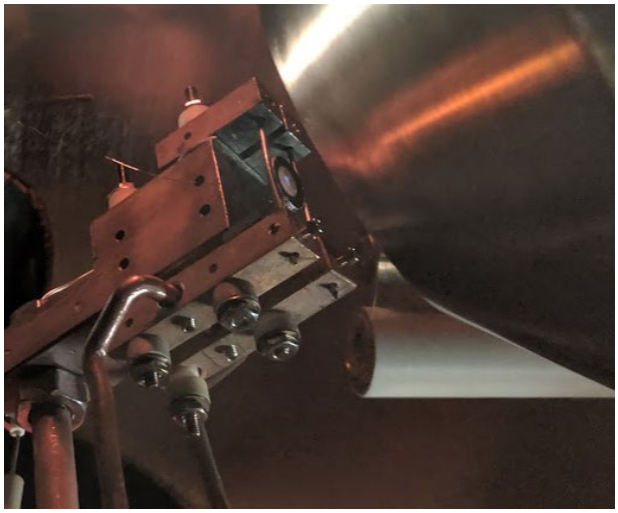

Figure 2-7 Fluorescence given out by the electron beam hitting the rhodium surface (the blue spot)

2.2.2 AES analysis

The Auger electron spectra gives the rate of emitted Auger electrons as a function of their energies in eV. Traditionally, there are two methods to analyze the spectra, by the area under the curve of raw data and by the peak intensity and atomic sensitivity factor of differentiated data.

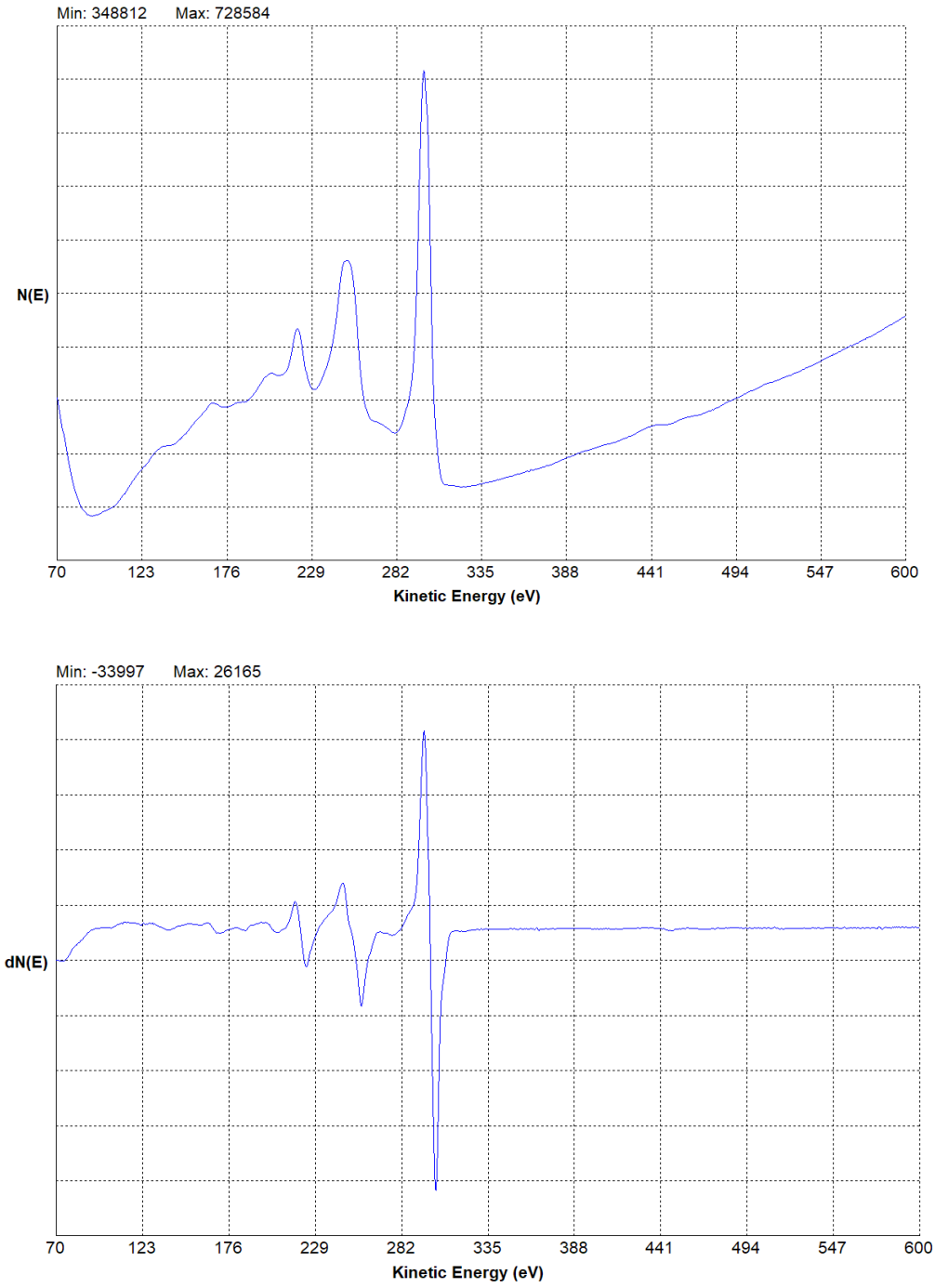

Figure 2-8 Raw (top) and differentiated (bottom) AES spectra of a clean Rh surface. The peaks at 207, 225, 259, and 305 eV are characteristic of Rh.

The first method is to use the area under the curve.[8] It is generally used when the peaks are close together hence are hard to differentiate. It is also useful when the spectra's

signal to noise ratio is high, in which case the differentiated data reflects more of the noise rather than the signal. For example, this method was used for carbon deposition on platinum, the relative ratios of the elemental areas give the total carbon coverage at the surface with respect to platinum. The procedure is described in detail by Eldridge.[8]

The second method is to differentiate the raw spectra first, then the height of the peak corresponding to each element is proportional to the concentration of the element, with a pre-determined atomic sensitivity factor.[7] A general expression for determining the atomic concentration of any constituent in a sample X_a, can be written as:

$$X_a = \frac{N_a}{\sum N_i} = \frac{I_a/S_a}{\sum I_i/S_i}$$

where N_i is the atom density of element i, I_i is the intensity (height) of the peak, and S_i is the atomic sensitivity factor.

Element/peak energy (eV)	S_i
Rh/305	3.1578
C/275	0.6143
O/510	1.2571

Figure 2-9 elemental sensitivity factors for Rh, C, and O at their characteristic Auger electron energy, primary beam energy is 3 keV.

The AugerScan software provides a function that shows the concentration of each element on the differentiated spectra. Note that this concentration is not the coverage of carbon on the surface, because although AES is a surface sensitive technique, it still detects a few layers deep into the bulk. The coverage of carbon is expressed as:

$$\theta_C = \frac{X_C}{X_{Rh}}$$

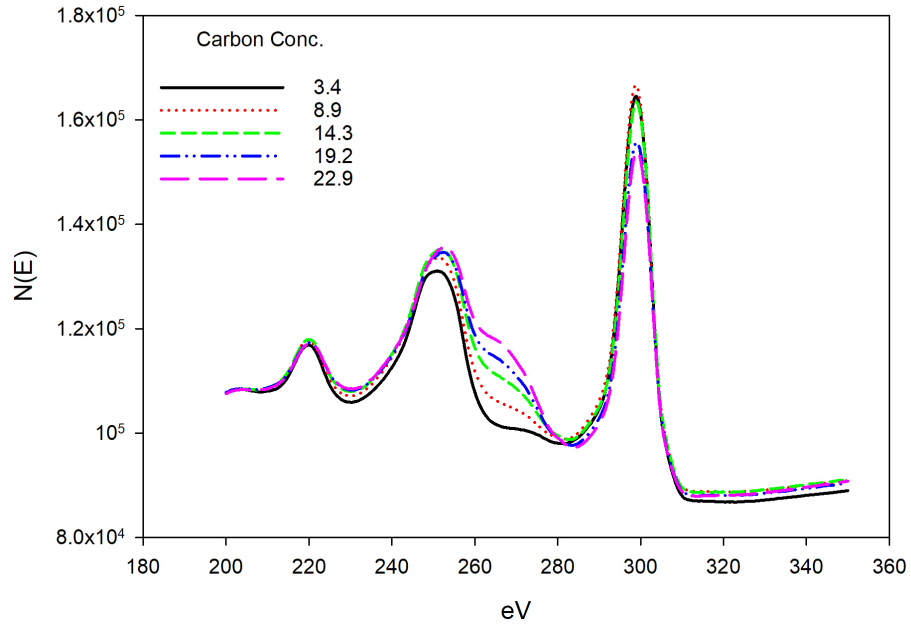

Figure 2-10 Undifferentiated AES showing Carbon peak (near 270 eV) increment. Carbon peak overlaps with Rh secondary peak to cause it to increase too.

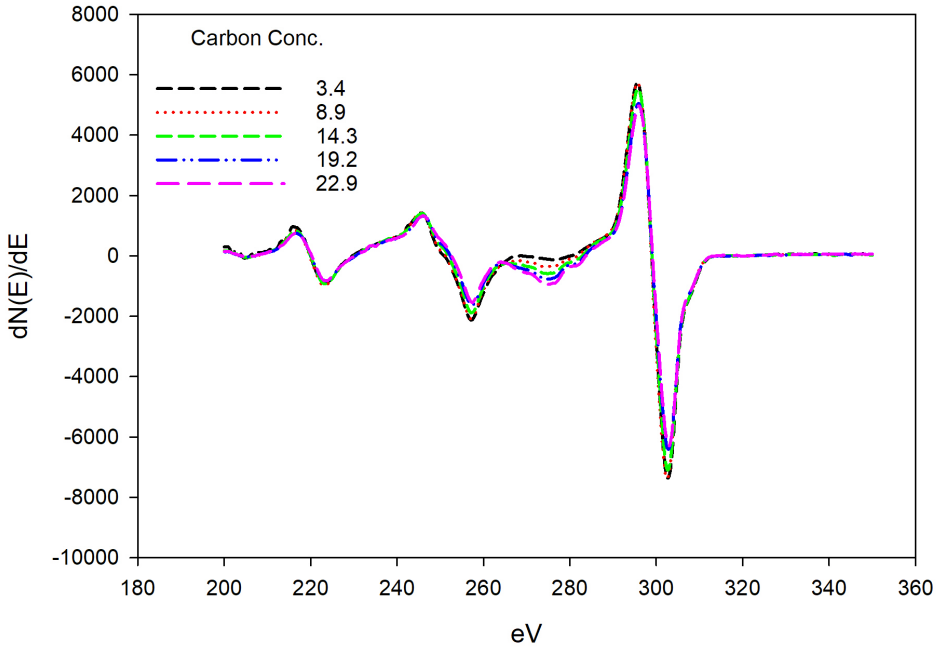

Figure 2-11 Differentiated AES showing carbon peak (near 270 eV) increment. Note that different from the undifferentiated spectra, carbon peak can be distinguished from the secondary Rh peak.

2.3 Crystal Preparation

From the process of refinement and cutting, common contaminations found on Rh are C, S, B, O, Si, and Mg.[9] Also, after alkane dissociative sticking coefficient experiments, some C may remain on the surface, which need to be cleaned before each next experiment. Despite being in an UHV chamber, the crystal is still exposed to residual gas. A typical gas composition in the chamber is acquired by the SRS RGA:

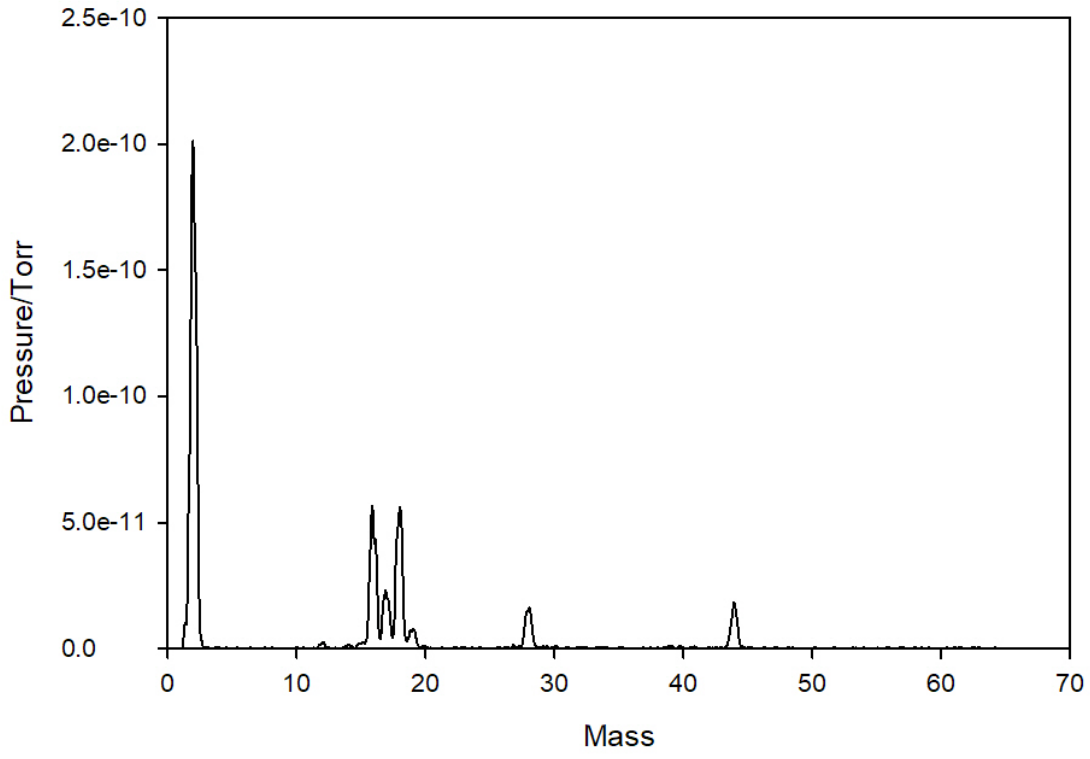

Figure 2-12 RGA spectrum, chamber pressure is 2e-10 torr when taken. H_2 is the main species in the UHV chamber, followed by water, CO, and CO_2

At our temperature of dosing (above 500K), CO does not adsorb on the surface; for experiments done below 500K, the crystal is flashed to above 500K to desorb any CO that might stick on the surface before running AES measurements.

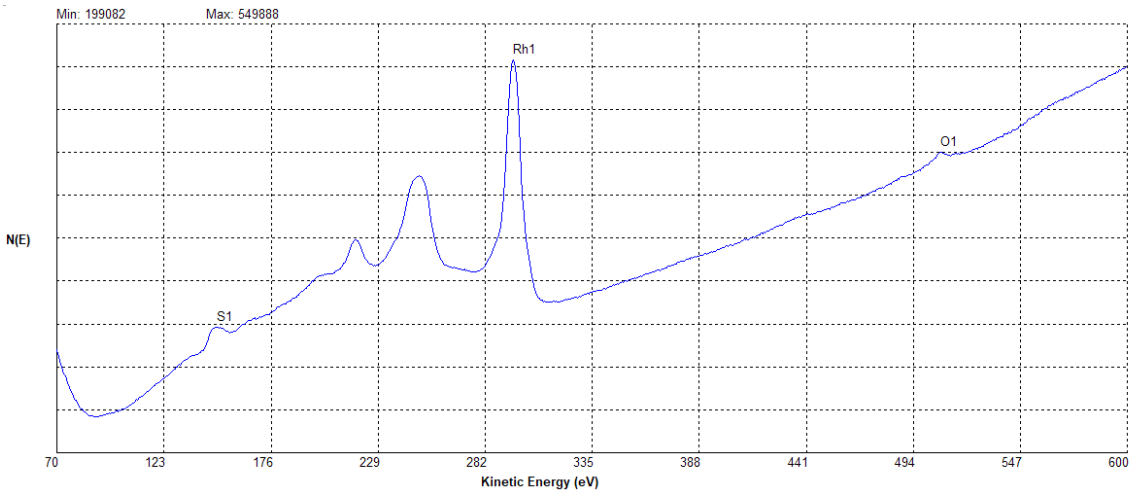

Figure 2-13 Rh surface with S and O

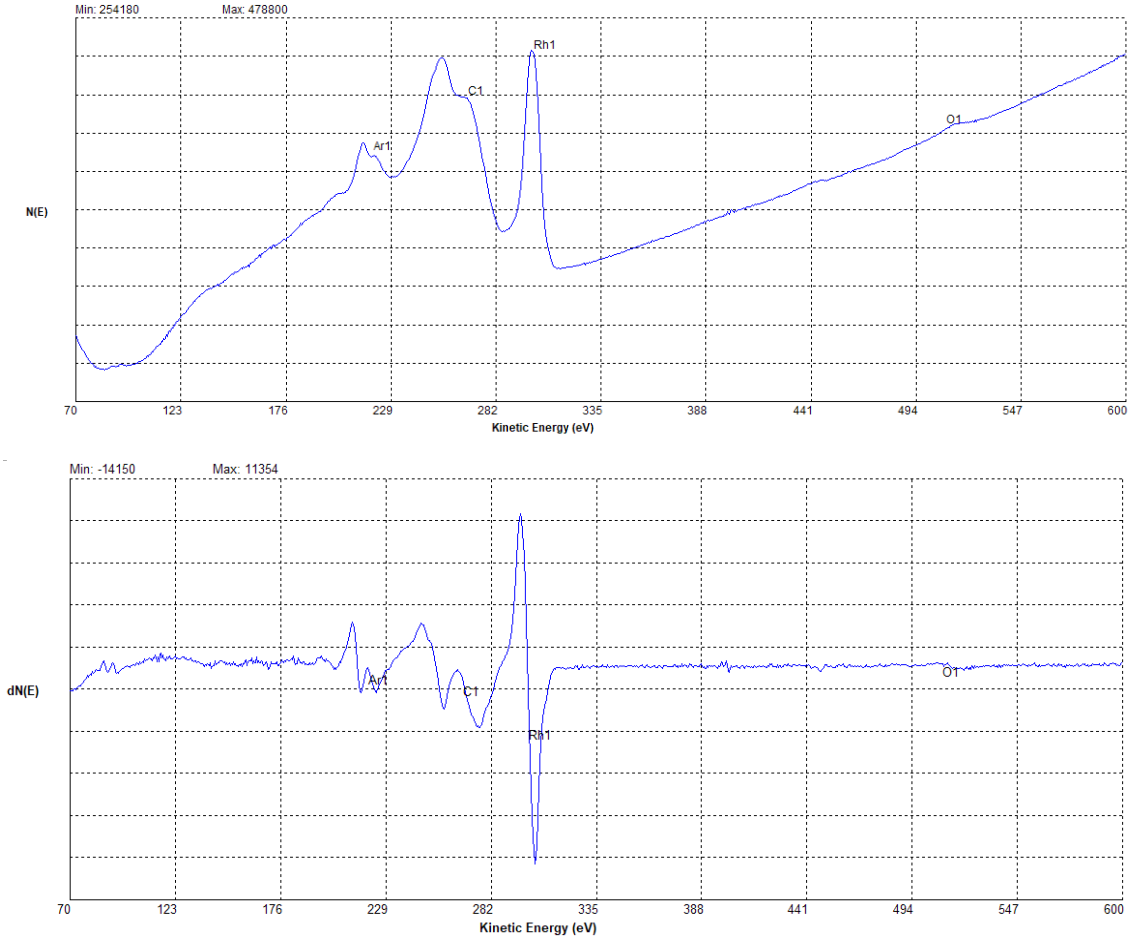

Figure 2-14 Rh surface with Ar, C, and O, raw spectrum (top) and differentiated spectrum (bottom)

2.3.1 Oxygen Cleaning

Oxygen cleaning is a common way for cleaning metal surfaces. It works by converting strongly bound contaminates into products that can easily desorb from the surface. The surface temperature needs to be greater than the molecular desorption temperature (T_s > 300 K) and lower than the recombinative desorption (T_s < 1000 K) temperature so that O_2 can dissociatively chemisorb to produce atomic O on the surface which may react with other adsorbates. The surface temperature should also allow carbon migration from the bulk to the surface in order to clean the subsurface carbon effectively while preventing surface carbon going into the bulk. The temperature for carbon diffusion into the bulk is around 1100 K. At 800 K, there is small amount of carbon migrating from the bulk to the surface; the diffusion rate is found to reach maximum at 900 K surface temperature. There have been several methods of cleaning Rh surfaces reported.[9-15] These methods generally involve argon ion sputtering, oxygen cleaning, and annealing in either oxygen, hydrogen, or vacuum, based on the type of experiments done and species on the Rh surface. In our lab, the species needs to be cleaned is carbon, and the following procedure was found to be effective in cleaning carbon on Rh(111) surface. O_2 is dosed onto the surface through a multicapillary array doser at the pressure of approximately 2×10^{-7} torr at 900 K crystal temperature for 15 minutes to 2 hours depending on the amount of carbon present. During the cleaning process, RGA can stay on to monitor the CO level. The CO level can be high initially, around 5×10^{-10} torr; then depends on the carbon coverage, the CO level should gradually decrease to around 5×10^{-11} torr. This can be used as an indication of the progress of cleaning.

Although oxygen cleaning is very effective in removing carbon on the rhodium surface, rhodium forms very stable oxides which cannot be cleaned even after prolonged time of annealing at 1250 K (Figure 2-7). Thus, argon sputtering is needed to clean the residual oxygen on the surface.

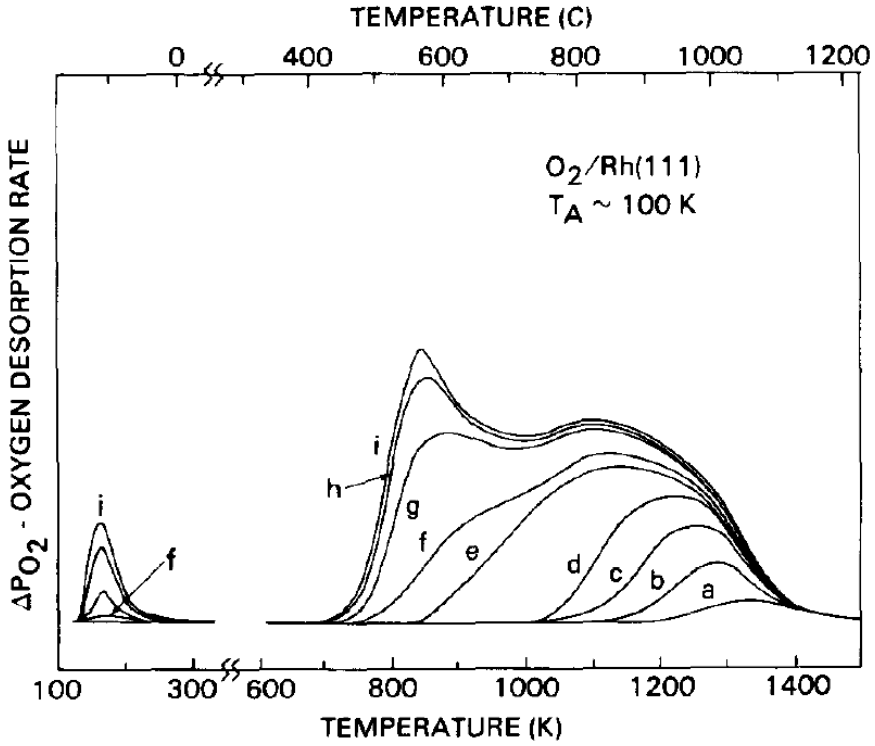

Figure 2-15 Oxygen TPD on Rh(111)[16]. Molecular desorption temperature is around 180 K, recombinative desorption temperature is around 1200 K. The peak near 850 K is from the subsurface oxygen.[15]

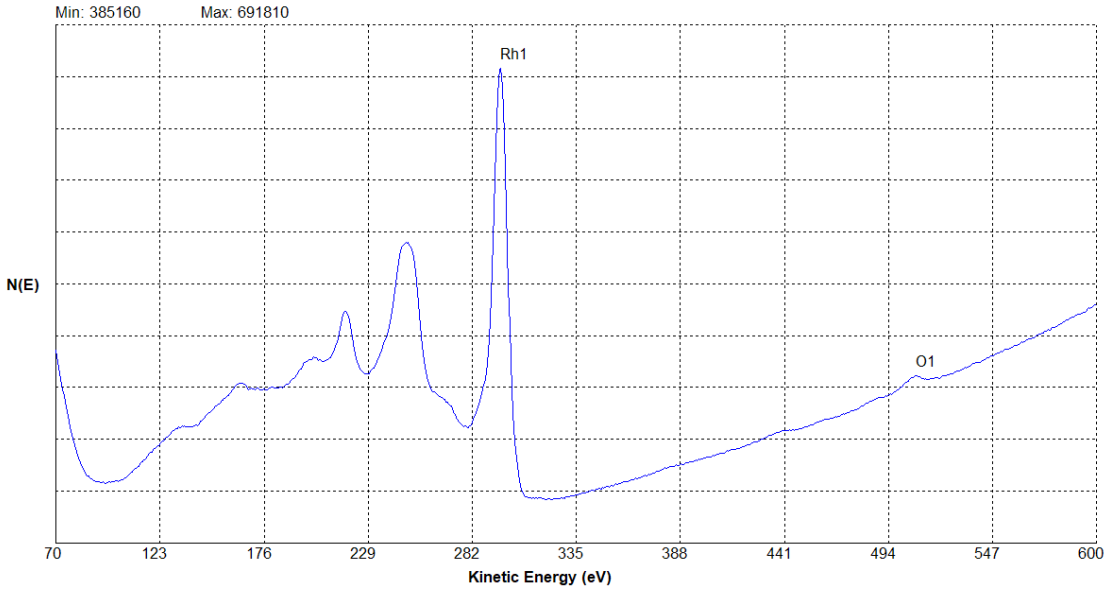

Figure 2-16 AES of Rh after oxygen cleaning for 20 mins at 2e-7 torr at 800 K, annealing to 1250K for 5 mins. Note there is still some oxygen left on the surface

2.3.2 Argon Ion Sputtering

Because oxygen on Rh is hard to remove by annealing to high temperature, argon sputtering is needed to clean Rh surface. In argon sputtering, the argon ions with high energy bombard the surface, causing the atoms (contamination and the substrate) on the surface to dislodge from the surface. This leads to damage and defect sites on the surfaces. However, this damage can be restored by annealing the crystal at high temperatures. In the meantime, by sputtering at low temperatures without annealing, it is possible to create defects on the surface hence changing the behavior of the surface.

For argon sputtering, the crystal is heated to 700 K, the chamber's ion pumps are first valved off because Ar pumping is damaging to them. And then the chamber is filled with 5×10^{-5} torr of Argon. The ion beam is started for argon sputtering for 10 minutes with Ar^{+} ions accelerated to 1 keV. The ion beam current reaching the crystal is typically 5 μA under

these conditions as measured by a multimeter connected to the crystal bias connection. After the sputter is done, turn off the ion beam then wait for the pressure in the chamber to decrease to below 5×10^{-8} torr, then gradually heat the crystal to 1300 K for annealing. The Oxford instruments cryostat cannot exceed 300 K, which limits how long and hot we can heat the attached sample. Hence, the process of annealing should last about 5 minutes, but not too long before the crystal mount is heated up and the pressure in the chamber starts to increase. It is good practice to keep the LabVIEW program on while doing argon sputtering to monitor the pressure change in the process.

After annealing, the crystal's temperature is brought down to below 400K to check for cleanliness and repeat if necessary. Dependent on the amount of contamination on the surface, the Ar^+ ion sputtering time may vary.

Carbon migration into the bulk of rhodium could be observed at sufficiently high surface temperature, typically above 900 K. A cycle of both oxygen cleaning and argon sputtering is needed to clean both the surface and the near-surface bulk of rhodium to ensure the carbon deposition measured is only from the dosing molecules. A detailed discussion of this is presented in chapter 4 of this thesis.

2.4 Dissociative Sticking Coefficient Measurements

Typically, after cleaning and annealing, the chamber's pressure is still high. Thus, after checking the cleanliness of the surface with AES from range 70 – 600 eV, all ion pumps and ion gauge are turned off to minimize the amount of active species formed, and the chamber is set still for about an hour to let the residual Ar to be pumped out of the chamber. Meanwhile the cooling stage continues to cool down from the elevated temperature caused by annealing.

Before the dosing starts, the surface composition is checked again by AES, this time, in 200 – 350 eV range where the peaks of carbon and rhodium reside. This step is to ensure that no contamination was deposited on the surface while chamber was being pumped out. This coverage of carbon is recorded to be the initial carbon coverage. It is worth mentioning that for clean rhodium surface, there is a small section on the differentiated AES that overlaps with the carbon peak, however, this "carbon coverage" can be subtracted from the apparent carbon peak to acquire the real carbon coverage increase.

To start dosing, the crystal is first brought to the heated doser's position; then the crystal is brought to the desired temperature for dosing. The gas manifold is then filled with desired pressure of dosing species. Next, start recording on the LabVIEW programmed for heated dosing that keeps track of the manifold pressure versus time that defines the gas exposed, then open the valve that's right behind the heated doser, then immediately open the valves that separate the dosing line with the alkane lecture bottle line. The first dosing time and pressure is set by trial and error. For example, first set the dosing pressure at the baratron to be 0.05 torr, dosing for 10 minutes. If the carbon concentration is too high (~30%), then dose again at either half the time or half the pressure. Repeat this process until one dose accumulates around 5 – 10% of carbon concentration increase. On the other hand, if the carbon concentration is too low after the first dose (less than 2%), next dose would need to be increased until the carbon concentration increases by 5 – 10 %. Once the appropriate dosage is determined for one temperature, dosing at other temperatures can be adjusted based on the known temperature, thus saving the process of finding the appropriate dosage. Then based on the coverage increase and corresponding

exposure (calculated by the pumping speed and dosing geometry of the chamber), sticking coefficient can be calculated.

In sum, the steps for the experiment are as follows. First, chamber pumping speed for the gas in question is measured. Second, the functional relationship between the pressure of gas line, read by an MKS Baratron, and the pressure of chamber, read by an ion gauge, is obtained. Third, the background sticking coefficient for each surface temperature is measured. Lastly, the direct sticking coefficient is calculated. The following sections discuss the details of each step.

2.4.1 Chamber pumping speed

To calculate the direct dissociative sticking coefficient, the chamber pumping speed C_c must be known accurately in order to calculate the flux ratio R. The pumping speed of the chamber (with all ion pumps turned off) is measured with a calibrated leak of conductance of 8.15×10^{-4} L/s. The throughput of the leak is linear with respect to the pressure behind the valve in the range of 0.005 – 0.100 torr. When only the leak valve and the turbomolecular pump is open, the throughput balance gives:

$$0 = C_l p_l - C_c p_c$$

where C_l is the conductance of the leak valve; p_l is the pressure behind the leak, which is estimated by the baratron adjacent to the leak; p_c is the pressure in the chamber; then the practical chamber pumping speed C_c could be expressed as:

$$C_c = \frac{C_l p_l}{p_c}$$

For methane, the chamber pumping speed is found to be 205 L/s. Note that when chamber pressure is too low, below 8×10^{-7} torr, corresponding to baratron pressure below 5×10^{-3} torr, the pumping speed is not constant anymore. This should not be a problem since all the dosing experiments were done at baratron pressure between 0.01 to 0.2 torr.

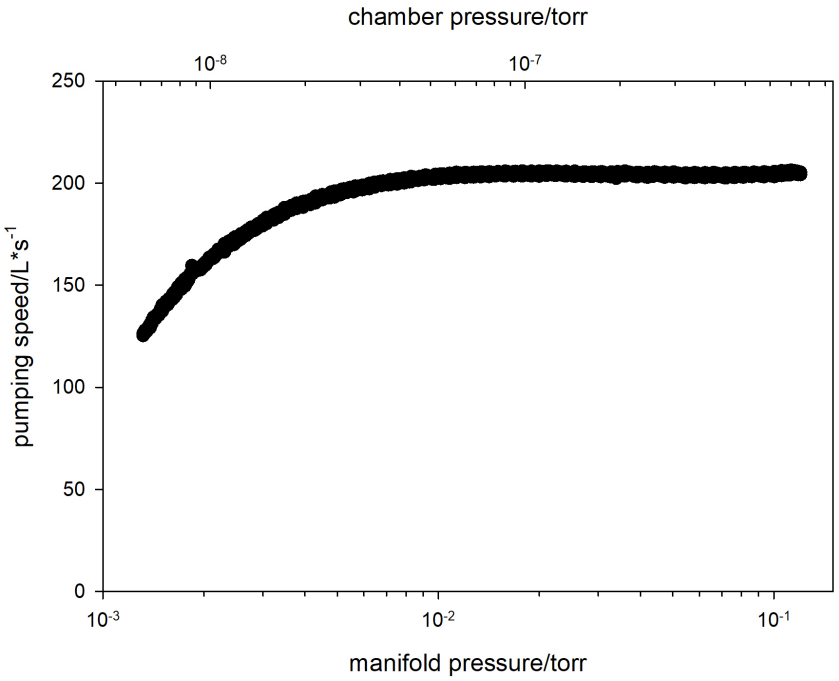

Figure 2-17 Measurement of chamber pumping speed for methane. The pumping speed is 205 L/s in experiment condition (0.01 – 0.1 torr in manifold). Note that when pressure is too low (<5×10^{-3} torr in manifold or <5×10^{-8} torr in the chamber), pumping speed starts to decrease

2.4.2 Chamber pressure and gas line pressure

During a dosing experiment, all ion pumps and ion gauge are turned off to prevent the formation of highly active radicals by collisions with the electrons or ions. However, the chamber pressure is needed in calculating the sticking coefficient. Empirically, the chamber pressure and the pressure in the gas line follow a quadratic equation. Thus, a quadratic curve was required for each doser temperature to monitor the chamber pressure during the experiment.

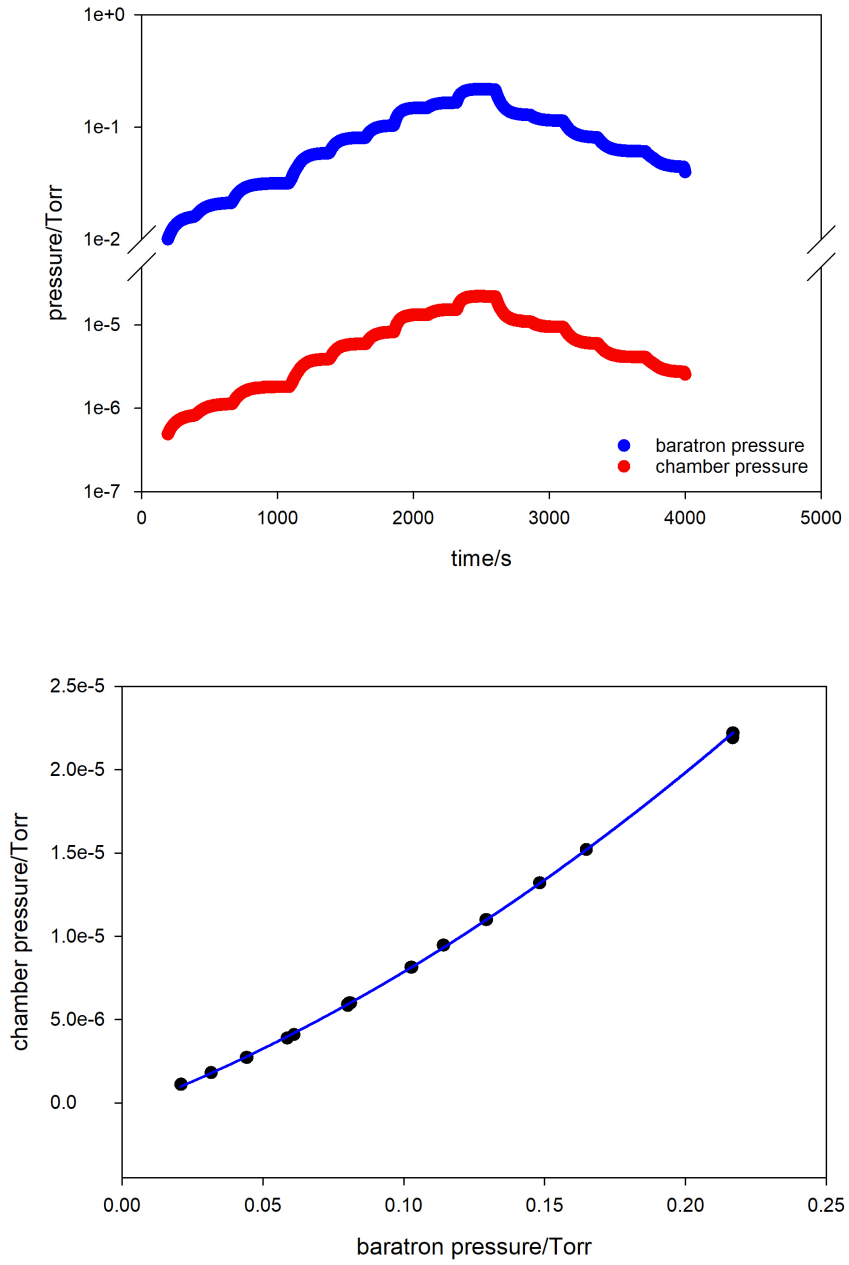

Figure 2-18 pressure of Baratron and chamber v.s. time (top) and the relation curve between the Baratron and chamber ion gauge when the pressure is at equilibrium(bottom). Every time the reagent variable leak valve rotates (about 30°), it takes about one minute for the pressure in the gas line (pink region in figure 3-2) to stabilize. The pressures on the Baratron and the chamber that are relatively still (flat on the top figure) were used to calculate the working curve. The data points on the increasing and decreasing curve fit on the same quadratic curve.

During a dosing experiment, the pressure remains relatively still before opening the valve. Once the valve behind the doser is opened, the pressure starts to drop. Then the pressure started to increase when the gas line is open to the lecture bottle. The challenge here is to maintain the pressure at the baratron, this is done by changing the variable leak valve right after the lecture bottle. Note that extra precautions are needed for this step because a slight rotation (about 15º) in the reagent variable leak valve would result in quite large (about 20% when at 0.1 torr) but a slow (takes about one minute) change of the pressure at the baratron. The pressure of the baratron cannot be changing too fast (more than 0.001 torr per second at 0.1 torr), because the quadratic curve that relates the chamber pressure and baratron pressure is acquired at equilibrium states. If the pressure is changing drastically (more than 1% per second), the pressure relation would not hold true.

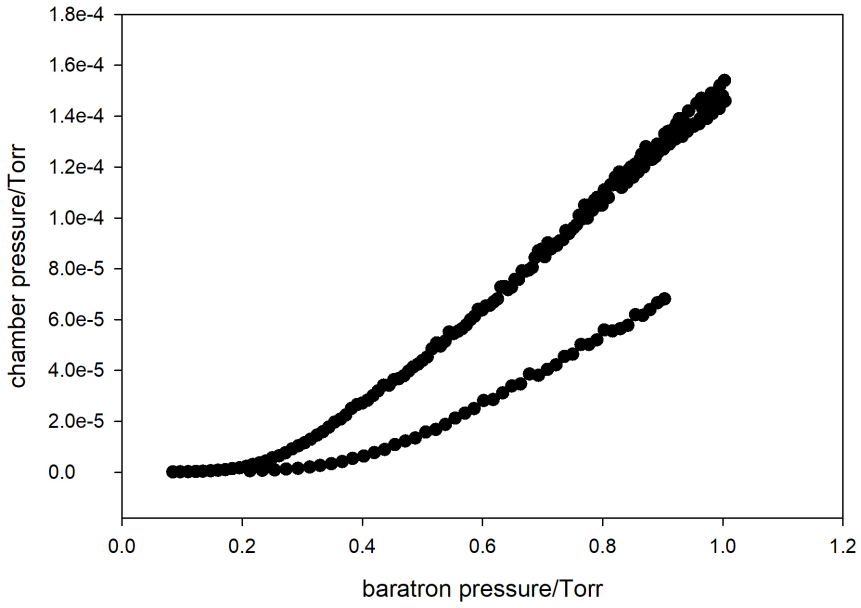

Figure 2-19 Pressure relation between baratron and chamber ion gauge when pressure is constantly changing. The top line took 3 minutes from 0.1 to 1.0 torr and the bottom line took 1 minute. Note that the pressure relation is not reproducible. The faster the pressure at Baratron is changing, the lower the chamber pressure is, due to not having enough time for gas to enter the chamber.

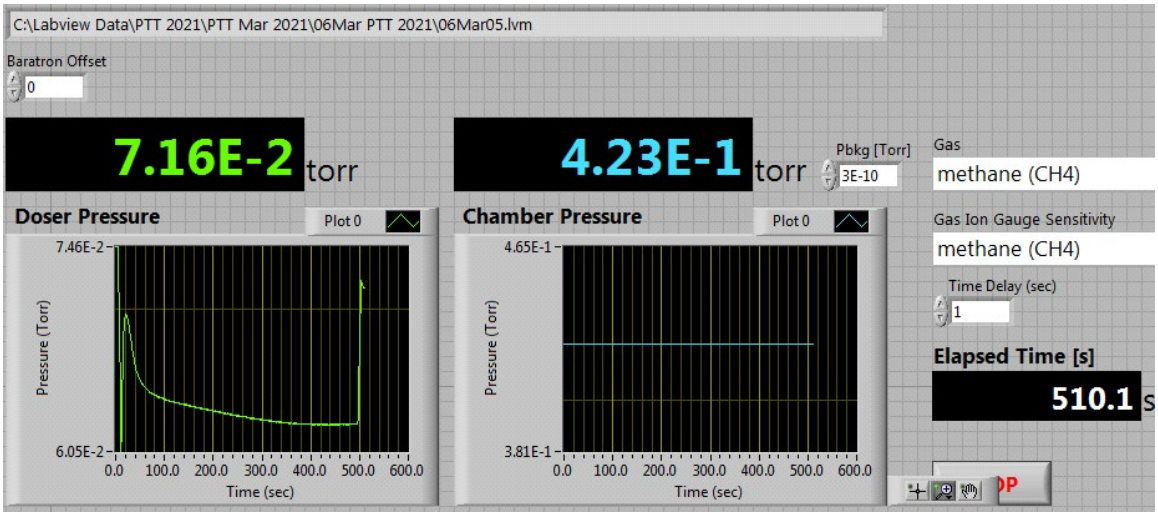

Figure 2-20 A typical dosage pressure profile. The gas line (pink region on figure 3-2) pressure drops when the valve (in the pink region) behind the doser opens then increase when the valves (in the light green region) that separate the gas line (pink region) from the gas manifold (green region) open. Then the reagent variable leak valve is adjusted to let the gas from the lecture bottle (yellow region) into the manifold (green region) to maintain the pressure stable. As can be seen from the left figure, the pressure only changes slightly (0.07 to 0.065) over the period of 450 s, which is much slower than 1% per second. The ion gauge in the chamber is turned off, hence the right figure reads a constant off value.

2.4.3 Background Sticking Coefficient

The background sticking coefficients were measured in separate experiments where the gas is leaked into the chamber at room temperature and with the crystal facing away from the doser. When the coverage is low, $S_{bkg}(T_c, T_s)$ can be determined by fitting the carbon coverage θ_C with exposure,

$$S_{bkg}(T_c, T_s) = \frac{\theta_c \sigma}{n F_{bkg} \tau} \tag{2.1}$$

Where n is the number of carbon atoms in the alkane molecule, σ is the areal density of the surface studied, τ is the dosing time, $F_{bkg} = \frac{p}{\sqrt{2\pi m k_B T_c}}$ is the background flux. In practice, it is difficult to maintain the pressure stably, so the dosage is calculated by integrating pressure at each second over time.

$$S_{bkg}(T_c, T_s) = \frac{\theta_c \sigma}{n F_{bkg} \tau} = \frac{\theta_C \sigma}{n \frac{p}{\sqrt{2\pi m k_B T_c}} \tau} = \frac{\theta_C \sigma \sqrt{2\pi m k_B T_c}}{n \int_0^\tau p dt} \quad (2.2)$$

Where p is the chamber pressure while dosing, m is the mass of the molecule in kg, k_B is the Boltzmann constant, and T_c is the chamber temperature.

To measure the background sticking coefficients, the crystal is set to a position that does not face the doser. Then the crystal is heated to the desired temperature to acquire the carbon deposition at that temperature. During this process, the doser is not heated and should remain room temperature. Dosing pressure was monitored by the LabVIEW program and recorded every second; then the pressures were integrated over every second to get the exposure. Then the carbon deposition is measured by AES and sticking coefficient is calculated using the equation (2.2).

2.4.4 Directed Sticking Coefficient

During a direct dosing experiment, the carbon deposition is from two sources: direct flux F_{dir} from the doser and background flux F_{bkg} from the scattered gas that did not react on the first collision with the surface but rather hit the chamber walls and thermalized to the chamber temperature before possibly hitting the surface:

$$\frac{d\theta_c}{dt} = \frac{n}{\sigma}\left[S(T_g, T_s;\ \vartheta)F_{dir} + S_{bkg}(T_c, T_s)F_{bkg}\right] = \frac{nF_{bkg}}{\sigma}\left[RS(T_g, T_s; \vartheta) + S_{bkg}(T_c, T_s)\right] \tag{2.3}$$

where θ_c is the carbon coverage at time t, $S(T_g, T_s;\ \vartheta)$ is the direct sticking coefficient at gas (doser) temperature T_g and surface (crystal) temperature T_s with an incident angle of ϑ, $S_{bkg}(T_c, T_s)$ is the background sticking coefficient at surface temperature T_s, T_c is the chamber temperature, and R is the ratio of direct flux to background flux.

$$R = \frac{F_{dir}}{F_{bkg}} = \frac{C_c\sqrt{2m}cos^3(\vartheta)j(\vartheta)}{W\sqrt{\pi k_B T_c}d^2} \tag{2.4}$$

where C_c is the chamber pumping speed. The detail of derivation and calculation of R is described elsewhere.[3]

The coverage dependence of each of the sticking coefficients are assumed to be in the form

$$S_i = S_{i0}\left(1 - \frac{\theta_C}{\theta_{C,sat}}\right)^m \tag{2.5}$$

where i = dir or bkg, $\theta_{C,sat}$ is the saturation carbon coverage, and S_{i0} is the initial sticking coefficient for the clean surface. Substitute S_{dir},

$$\frac{d\theta_C}{dt} = \frac{n}{\sigma_{Rh}}\left[S_{dir,0}(T_g, T_s)F_{dir} + S_{bkg,0}(T_c, T_s)F_{bkg}\right]\left(1 - \frac{\theta_C}{\theta_{C,sat}}\right)^m \tag{2.6}$$

where $F_{dir} = R\,F_{bkg}$,

$$\frac{d\theta_C}{dt} = \left[S_{dir,0}(T_g, T_s) + \frac{1}{R} S_{bkg,0}(T_c, T_s) \right] \left(1 - \frac{\theta_C}{\theta_{C,sat}} \right)^m \frac{n F_{dir}}{\sigma_{Rh}} = S_{app,0} \left(1 - \frac{\theta_C}{\theta_{C,sat}} \right)^m \frac{n F_{dir}}{\sigma_{Rh}} \quad (2.7)$$

when m = 1,

$$\theta_C = \theta_{C,sat} \left(1 - Exp \left[- \frac{S_{app,0}\, n\, \varepsilon_{dir}}{\theta_{C,sat}} \right] \right) \quad (2.8)$$

where ε_{dir} is the direct exposure in 111 monolayers which is given by,

$$\varepsilon_{dir} = \frac{\int_0^\tau F_{dir} dt}{\sigma_{Rh}} = \frac{R \int_0^\tau F_{bkg} dt}{\sigma_{Rh}} = \frac{R \int_0^\tau p dt}{\sigma_{Rh} \sqrt{2\pi m k_B T_C}} = \frac{R F_{bkg} \tau}{\sigma_{Rh}} \quad (2.9)$$

The final direct sticking coefficient can be calculated as,

$$S_{dir,0}(T_g, T_s) = S_{app,0} - \frac{1}{R} S_{bkg,0}(T_c, T_s) \quad (2.10)$$

where $S_{app,0}$ comes from fitting the $\theta_C(\varepsilon_{dir})$ experimental data, R is calculated based on the chamber pumping speed and the dosing geometry, S_{bkg} is measured in separate ambient dosing experiments.

The carbon coverage, for small θ_C accumulation so that the argument of the exponent in Eq(2.8) is small, is linear with exposure, such that,

$$\theta_C = \theta_{C,sat} \left(1 - Exp \left[- \frac{S_{app,0}\, n\, \varepsilon_{dir}}{\theta_{C,sat}} \right] \right) = S_{app,0}\, n\, \varepsilon_{dir} \quad (2.11)$$

Substituting (2.9), eq.(2.11) can be rewritten as,

$$S(T_g, T_s) = \frac{1}{R}\left[\frac{\theta_C \sigma}{nF_{bkg}\tau} - S_{bkg}(T_c, T_s)\right] \tag{2.12}$$

Where $S_{bkg}(T_c, T_s)$ is the background sticking coefficient at surface temperature T_s. In practice, it is difficult to maintain the pressure stably, so the dosage is calculated by integrating pressure at each second over time.

$$\begin{aligned} S(T_g, T_s) &= \frac{1}{R}\left[\frac{\theta_C \sigma}{n\frac{p}{\sqrt{2\pi m k_B T_c}}\tau} - S_{bkg}(T_c, T_s)\right] \\ &= \frac{1}{R}\left[\frac{\theta_C \sigma\sqrt{2\pi m k_B T_c}}{n\int_0^\tau p dt} - S_{bkg}(T_c, T_s)\right] \end{aligned} \tag{2.13}$$

To measure the direct sticking coefficient, the crystal's surface faces the orifice of the doser, and the temperature of either the doser or the crystal is varied independently to acquire either equilibrium ($T_s = T_g$) or non-equilibrium ($T_s \neq T_g$) sticking coefficient. Similar procedure to that of the background is used to get the exposure and carbon coverage. Lastly, the sticking coefficient is subtracted by the background sticking coefficient at that surface temperature using Eq. (2.13).

2.4.5 Angle Resolved Sticking Coefficient

Varying the relative position of the crystal and the doser allows for measuring the angle-resolved sticking coefficient $S(T_g, T_s; \vartheta)$. Since the distance d is fixed during experiments (1.0 cm), the impinging angle ϑ of a spot on the surface can be calculated by $\tan\vartheta = \frac{c}{d}$, where c is the displacement of a spot relative to the centerline of the doser. The doser line is usually inline with the center of the crystal, and because the crystal is 8 mm

diameter, this allows for angle-resolved measurements up to ±21 degrees. By measuring the carbon coverage as a function of position across the surface using AES and knowing how the impinging flux varies across the surface, the $S(T_g, T_s; \vartheta)$ can be determined. When measurements at higher angles are needed, the crystal can be moved away from the doser in the plane perpendicular to the beam direction, which allows a larger transverse displacement. Because of this, two experiments are enough to acquire angle-resolved sticking coefficients from -15 to 45 degrees. This is discussed in detail in chapter 3.

2.4.6 Calculated by Slope

For methane dissociative chemisorption, the rate of carbon deposition is[17]:

$$\frac{d\theta}{dt} = S_0 \left(1 - \frac{\theta}{\theta_{max}}\right) F \tag{2.14}$$

where θ is the coverage, θ_{max} is the saturation coverage of carbon, and S_0 is the initial sticking coefficient, F is the flux in ML/s, and the exposure is $\epsilon = Ft$. When $\theta \ll \theta_{max}$, equation (2.14) reduces to

$$\frac{d\theta}{dt} = S_0 F, \text{ or } \theta = S_0 \epsilon$$

where coverage increase linearly with increasing exposure. When the coverage is in the linear range, a simple linear regression fit can be used to determine the sticking coefficient. Note that the unit of ϵ is monolayer (ML) in this case. For methane on Rh(111), 1 ML is $\frac{\sigma}{F} = \frac{\sigma\sqrt{2\pi m k_B T_c}}{p} = 3.12\times10^{-6}$ Torr·s.

In surface experiments,exposure is ofen reported in unit of Langmuir, L, which is defined as 1L = 1×10^{-6} Torr·s. For convenience, the sticking coefficient in the linear range is thus expressed as:

$$S_{bkg}(T_c,\ T_s) = \frac{\sigma\theta_C\sqrt{2\pi mk_BT_c}}{n\int_0^\tau pdt}$$

$$\theta_C = \frac{S_{bkg}(T_c,\ T_s)n}{\sigma\sqrt{2\pi mk_BT_c}}\int_0^\tau pdt = S_{bkg}(T_c,\ T_s)\epsilon_{bkg}$$

where θ_C is the coverage with corresponding dosage ϵ_{bkg}.

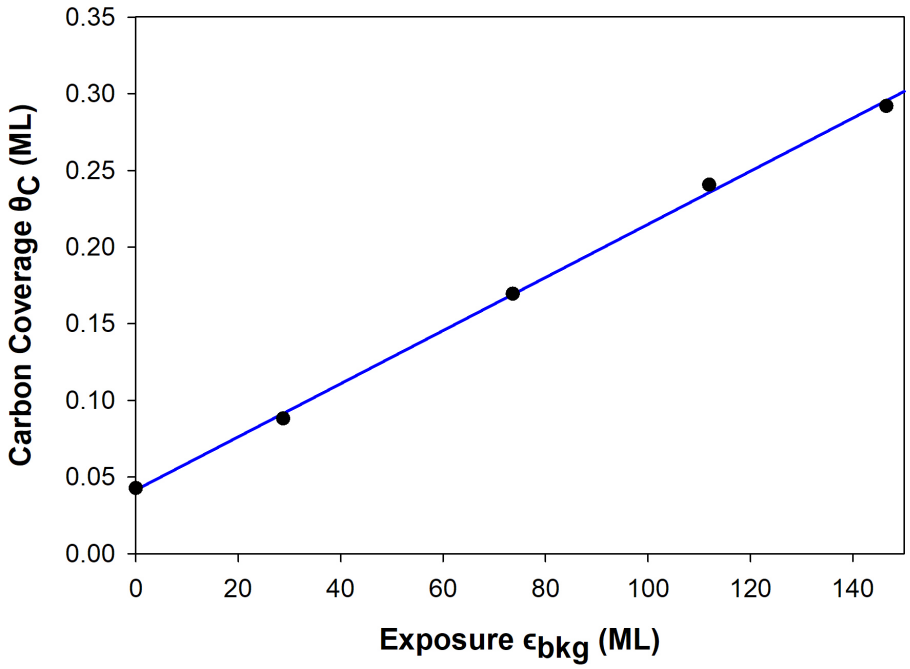

Figure 2-21 Carbon coverage vs. exposure in ML, the slope of this curve is S_{bkg}

2.4.7 Calculated by Saturation Curve

When the surface's temperature is low hence the saturation coverage of carbon is low, it is challenging to work in the linear range of sticking coefficients. In this case, a

coverage dependent sticking coefficient nonlinear fit could be used to determine the initial sticking coefficient:

$$\theta = \theta_{max}\left[1 - \exp\left(-\frac{S_0\epsilon}{\theta_{max}}\right)\right]$$

where ϵ is the exposure, θ is the coverage at the corresponding exposure, θ_{max} is the apparent maximum coverage of carbon at that temperature, and S_0 is the initial sticking coefficient when the coverage is 0. This way not only could the initial sticking coefficient be determined, but also the apparent maximum coverage of carbon at that surface temperature.

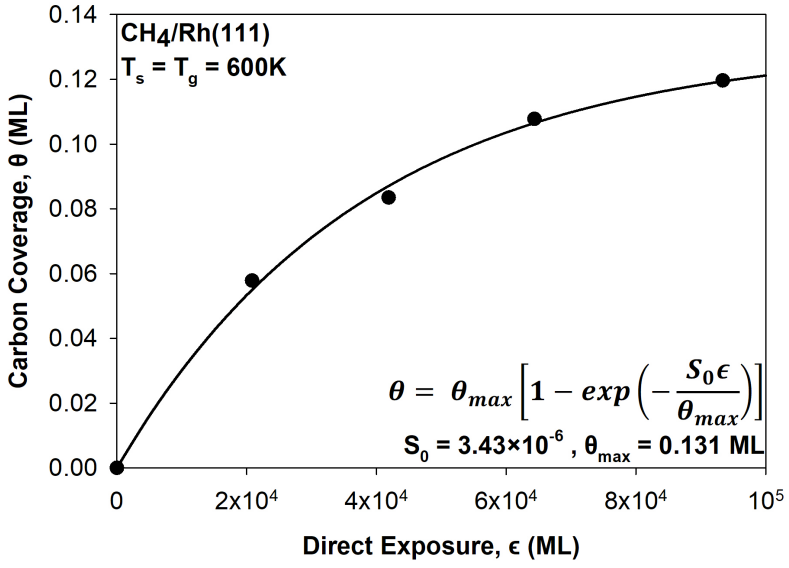

Figure 2-22 coverage curve fit to coverage dependent sticking coefficient of methane at 600K gas and 600K surface. The apparent sticking coefficient is 3.43×10^{-6} *and the maximum coverage of carbon at this surface temperature is* 0.131 ML.

Reference

1. Cusing, G. W. Hydrocarbon Reactivity on Pt(111): Dissociative Sticking Coefficient and Evan-Polanyi Relation. University of Virginia, 2011.
2. Donald, S. B. Precursor Mediated Microcanonical Trapping Model of Activated Dissociative Chemisorption at Surfaces: Assessment of Dynamical Effects. University of Virginia, 2013.
3. Navin, J. K. Light Alkane Reactivity on Pt(111) Investigated Using Effusive Molecular Beam Methods. University of Virginia, 2014.
4. Singh, H., Determination of Thermal Expansion of Germanium, Rhodium and Iridium by X-Rays. *Acta Crystallographica Section A: Crystal Physics, Diffraction, Theoretical and General Crystallography* **1968**, *24*, 469-471.
5. *Sigma-Aldrich Bulletion 918b Selecting Purifiers for Gas Chromatography*, 1999.
6. *Sigma-Aldrich Supelpure®-O Oxygen/Moisture Trap, Safety Data Sheet.*, 6.3 ed., 2020.
7. Childs, K. D.; Carlson, B. A.; LaVanier, L. A.; Moulder, J. F.; Paul, D. F.; Stickle, W. F.; Waston, D. G., *Handbook of Auger Electron Spectroscopy*, Third ed.; Physical Electronics, 1995.
8. Eldridge, T. J. Alkane Activation on Pt(111): Thermal Kinetics, Thermodynamics, and the Role of Van Der Waals Interactions. University of Virginia, 2018.
9. Musket, R. G.; Mclean, W.; Colmenares, C. A.; Makowiecki, D. M.; Siekhaus, W. J., Preparation of Atomically Clean Surfaces of Selected Elements - a Review. *Appl Surf Sci* **1982**, *10*, 143-207.
10. Zhang, C., et al., Steps and Catalytic Reactions: Co Oxidation with Preadsorbed O on Rh(553). *Surf Sci* **2022**, *715*, 121928.
11. Winkler, P.; Zeininger, J.; Raab, M.; Suchorski, Y.; Steiger-Thirsfeld, A.; Stöger-Pollach, M.; Amati, M.; Gregoratti, L.; Grönbeck, H.; Rupprechter, G., Coexisting Multi-States in Catalytic Hydrogen Oxidation on Rhodium. *Nat Commun* **2021**, *12*, 6517.
12. Garcia-Martinez, F.; Schiller, F.; Blomberg, S.; Shipilin, M.; Merte, L. R.; Gustafson, J.; Lundgren, E.; Ortega, J. E., Co Chemisorption on Vicinal Rh(111) Surfaces Studied with a Curved Crystal. *The Journal of Physical Chemistry C* **2020**, *124*, 9305-9313.
13. Xu, X. P.; Friend, C. M., Role of Coverage in Determining Adsorbate Stability - Phenol Reactivity on Rh(111). *J Phys Chem-Us* **1989**, *93*, 8072-8080.
14. Fisher, G. B.; Schmieg, S. J., The Molecular and Atomic States of Oxygen Adsorbed on Rh(100) - Adsorption. *J Vac Sci Technol A* **1983**, *1*, 1064-1069.
15. Derouin, J.; Farber, R. G.; Killelea, D. R., Combined Stm and Tpd Study of Rh(111) under Conditions of High Oxygen Coverage. *The Journal of Physical Chemistry C* **2015**, *119*, 14748-14755.
16. Root, T. W.; Schmidt, L. D.; Fisher, G. B., Adsorption and Reaction of Nitric Oxide and Oxygen on Rh(111). *Surf Sci* **1983**, *134*, 30-45.
17. Cushing, G. W.; Navin, J. K.; Valadez, L.; Johanek, V.; Harrison, I., An Effusive Molecular Beam Technique for Studies of Polyatomic Gas-Surface Reactivity and Energy Transfer. *Rev Sci Instrum* **2011**, *82*.

3 Methane Activation on Rh(111) and the Reactivity of Step Sties

3.1 Introduction

Steam reforming is one of the most important chemical processes. Its product, syngas (a mixture of H_2 and CO) is the primary feedstock to produce higher hydrocarbons and other useful organic chemicals via Fischer-Tropsch synthesis. Ni-based catalysts are most commonly used in industry due to its availability, although other precious transition metals such as Rh, Ru, Pd, and Pt also display high activity towards steam reforming. However, steam reforming is usually performed in large-scale reactors and has high energy demand.

Catalytic partial oxidation of methane, on the other hand, can be carried out in compact and low capital-cost reactors to produce syngas. Platinum and rhodium are both intensively studied for this process. Vlachos et al. found that for short contact time partial oxidation of methane on Rh catalysts, different chemical reactions compete in different reaction zones: deep combustion of methane in oxidation zone, steam reforming and water gas shift in reforming zone where oxygen is not available.[1-2] On a woven platinum-10 percent rhodium gauze catalyst, with rapid heating, short contact time, and rapid quenching to avoid homogeneous reactions, higher alkanes can be converted to olefins and aldehyde with efficiency as high as 60%.[3] On a rhodium based honeycomb monolith reactor, it is found that partial oxidation of methane increases with lower oxygen coverage, where partial oxidation takes dominance hence increasing syngas selectivity.[4] Rhodium has been shown to be a better catalytic material for partial oxidation of methane than platinum[5] whereas platinum is favored as a catalyst for complete oxidation of methane[6]. In a series

of combined experimental and theoretical studies, Schmidt et al concluded that, in short contact time experiment where methane is directly oxidized to H_2 and CO, rhodium was much better than platinum in producing more H_2 and less H_2O, due to the higher energy barrier towards formation of OH hence favoring H + H == H_2 reaction.[5, 7]

These short contact time reaction studies disclosed the competing relation of the methane dissociation on Rh surface and the homogeneous combustion in gas phase. Hence, understanding how methane dissociate on Rh surface has attracted a great amount of studies since last century. Ehrlich et al conducted isotope experiments that showed that vibration is effective in dissociation.[8] Later, Yates et al. conducted a direct laser excitation study using only excited ν_3 and $2\nu_4$ vibrational modes to promote reactivity, but those attempts were unsuccessful.[9-10] Ehrlich et al. obtained an activation energy in the range of 21 – 26 kJ/mol by measuring thermal sticking coefficients of methane and deuterated methanes where gas temperature and surface temperature were kept the same, from 250K to 350K.[11-12]

Since the new century, density functional theory (DFT) electronic structure calculation studies have also been done to illuminate the activation mechanism of methane on Rh. Multiple groups have used PW91 to study the activation energy of the initial C-H bond breakage in CH_4. However, the results varies even though the same set was used. (Table 1)

	Activation Energy kJ/mol	Functional
Bunnik, et al. [13]	70	PW91
Grootel, et al. [14]	58	PW91
Wang, et al. [15]	79.4	PW91
Zhu, et al. [16]	58	PW91
Hu, et al. [17]	64.6 on terraces, 30.9 on steps	PBE

Table 3-1 activation energies calculated by different groups

Another DFT calculation using PBE by Hu suggested 65kJ/mol and 31kJ/mol for terrace and step activation energies, respectively, for CH_4 dissociation on Rh(111).[17] Unfortunately, to the author's best knowledge, there has not been direct surface chemistry experimental work on Rh(111) to determine the activation barrier.

Here, using effusive beam technique, we were able to measure the sticking coefficient of methane with different gas and surface temperature, providing information on both gas activation and surface activation. Using an Arrhenius fit, we calculated the activation energy of methane dissociation on Rh(111) at equilibrium temperatures where gas temperature is equal to surface temperature. Furthermore, with the ability to change the dosing angle, we can alter the normal translational energy in dosing gas, hence allows us to study the efficacy of translational and vibrational energy. Combined with our own precursor-mediated microcanonical trapping (PMMT) model[18-20], we provide an in-depth view of methane activation mechanism on Rh(111) surface.

3.2 Experiments Detail

Experiments were performed using an ultrahigh vacuum (UHV) surface analysis chamber equipped for Auger electron spectroscopy (AES) using a double pass cylindrical mirror analyzer, thermal programmed desorption, residual gas analysis, and effusive molecular beam dosing. The UHV chamber had a base pressure of 1×10^{-10} torr. The 8 mm diameter Rh(111) crystal was cleaned prior to experiments by Ar^+ ion sputtering at T_s at 700K and annealing to 1150K in good UHV, until no contaminants were detectable by AES. Methane was obtained from PRAXAIR (ME 5.0RS) and had a purity of 99.999%, and was further purified by flowing through a Supelco filter (model 2-2450-U), capable of removing trace amounts of reactive impurities. The molecular beam doser [21] and

methodology[22] for making effusive molecular beam measurements of alkane dissociative chemisorption have been described in detail elsewhere, and only a brief synopsis follows. Methane dissociative chemisorption was assumed to lead exclusively to desorbing H_2 gas and chemisorbed products at temperature above 500K. the effusive molecular beam doser had a 0.0076 mm thick end-wall with a 0.5 mm diameter orifice that resulted in a calculated molecular flux distribution in solid angle, $d^2N(\theta)/d(\Omega)dt$, that varied as $\sim\cos^{1.3}\theta$, which, when projected onto the Rh(111) surface, oriented normal to the beam's center line, gave an incident molecular flux, $d^2N(\theta)/d(A)dt$, that varied as $\sim\cos^{4.3}\theta$ across the surface. The net effusive beam flux was determined by comparison to flux from a calibrated leak. With the effusive beam doser and surface temperatures set to certain temperatures, the cleaned Rh(111) surface was positioned 10.0 mm in front of the effusive beam orifice before gas dosing began. After dosing, AES was used to measure the C reaction product coverage left behind on the surface as a function of dosage. Heated beam molecules that missed the Rh(111) surface, raised the ambient chamber pressure and were assumed to be rapidly thermalized to the chamber wall temperature prior to any further possible collisions with the surface. The reactive contribution from this "cold" ambient alkane gas flux to the C deposition on the surface was subtracted when calculating the sticking coefficient.

$$S(T_g, T_s) = \frac{1}{R}\left[\frac{\theta_C \sigma}{n F_{bkg} \tau} - S_{bkg}(T_c, T_s)\right] \tag{3.1}$$

Where $\sigma = 1.58 \times 10^{19}$ m^{-2} is the areal density of Rh(111), n is the number of carbons in the alkane, in this case, 1 for methane, $F_{bkg} = p/(2\pi m k_B T_c)^{1/2}$ is the background flux from the thermalized gas load that strikes the surface, R is the ratio of the direct flux, F_{dir}, from the effusive molecular beam that strikes the surface to the background flux, and $S_{bkg}(T_c, T_s)$

is the dissociative sticking coefficient for the ambient background gas at the chamber temperature that strikes the surface. With the beam orifice at a distance d away from the center of the sample surface, the ratio R varies spatially across the surface as

$$R = \frac{F_{dir}}{F_{bkg}} = \frac{C_c\sqrt{2m}cos^3(\theta)j(\theta)}{W\sqrt{\pi k_B T_c}d^2} \tag{3.2}$$

The experiments were done at both doser and crystal temperature range from 500K to 900K. The ion pumps and ion gauges were turned off to avoid high reactivity radicals. The chamber pressure was then related to the doser pressure by a quadratic curve which was measured at each different doser temperature. In practice, the dosage is calculated by integrating pressure at each second over time due to the difficulty of keeping the dosing pressure constant.

$$\begin{aligned} S(T_g, T_s) &= \frac{1}{R}\left[\frac{\theta_C \sigma}{n\dfrac{p}{\sqrt{2\pi m k_B T_c}}\tau} - S_{bkg}(T_c, T_s)\right] \\ &= \frac{1}{R}\left[\frac{\theta_C \sigma\sqrt{2\pi m k_B T_c}}{n\int_0^\tau dp} - S_{bkg}(T_c, T_s)\right] \end{aligned} \tag{3.3}$$

For high surface temperatures, the final sticking coefficient is the average of several increment dosing. For low surface temperatures, the sticking coefficient is acquired by fitting the coverage v.s. exposure to the coverage dependent sticking coefficient.

$$\theta = \theta_{max}\left(1 - \exp\left(-\frac{S_0\epsilon}{\theta_{max}}\right)\right) \tag{3.4}$$

To ensure the coverage was measured at where the beam centerline hit the surface, a trial dosing was done, then measured across the crystal to find the maximum coverage spot. The following measurements were all done at the same position. Background sticking was measure for each surface temperature and was subtracted when calculating the sticking coefficient. To ensure the carbon deposited on the surface is only from methane, the crystal was put in the chamber similar to the experimental condition for several hours, and no carbon coverage change was observed.

For sticking coefficients at different angles, the gas and surface temperature were both kept at 700K. AES was used to measure the C coverage across the surface as a function of distance away from where the beam centerline hit the surface. To measure the sticking coefficient at higher angles, the crystal was shifted further away from the doser. Sticking coefficients were calculated at the same angles for different experiments, and the absolute values were found to be within 20% of difference. To ensure no carbon migration on the surface, the surface was heated to 900K for 10 mins, and no change in carbon coverage distribution was observed.

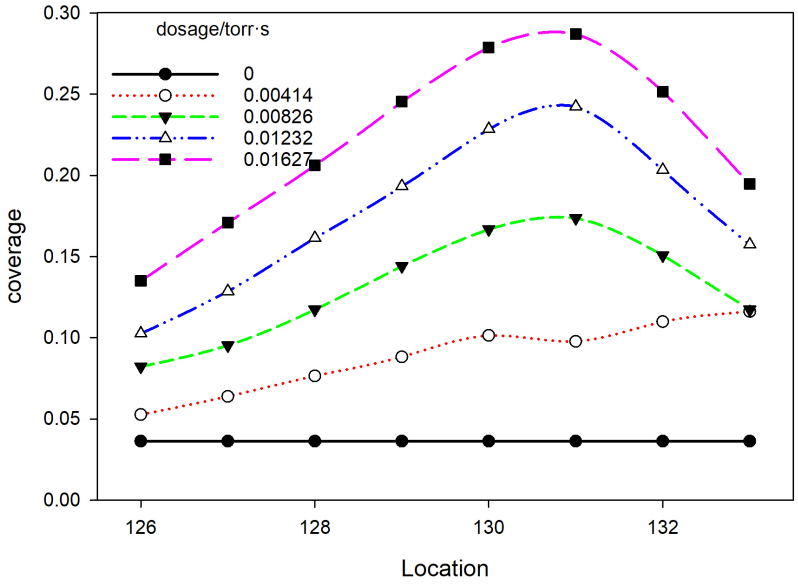

Figure 3-1 carbon coverage increases with respect to dosage at different locations on the surface. The coverage near the center of the beam (130.5) increases the fastest, the further away the location is from the center, the slower the increase is.

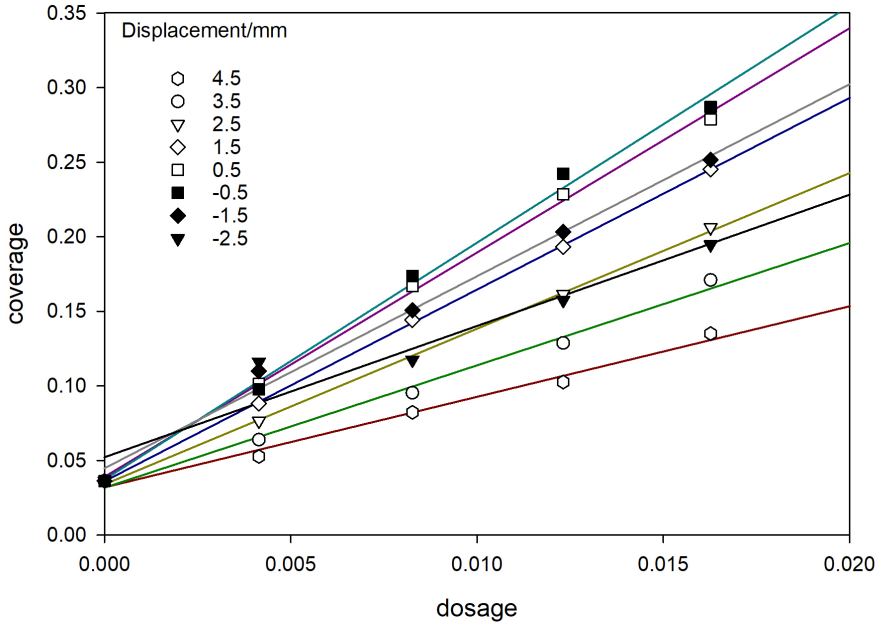

Figure 3-2 carbon coverage at different locations increases with dosage. The coverages at symmetry spots increase at very similar rate.

3.3 PMMT Model

Figure 3-3 shows a schematic overview for the PMMT models of activated dissociative chemisorption.[19, 21, 23] The precursor complexes (PC) in these models are transient gas-surface collision complexes composed of an impinging molecule interacting with a few local surface oscillators. PCs are assumed to have their exchangeable energy microcanonically randomized if their energy is sufficient to gain access to the strongly state-mixing regions of the reactive potential energy surface near the transition state, at least a collective sense when averaged over the ensemble of collision complexes formed.[23-25] The PCs formed are transiently trapped between the transition states for the desorption and dissociative chemisorption (reaction) and are assumed to go on to desorb or react with Rice-Ramsperger-Kassel-Marcus (RRKM)[26] microcanonical rate constants.

$$k_i(E^*) = \frac{W_i(E^*)}{h\rho(E^*)} \tag{3.5}$$

where E^* is the active exchangeable energy whose zero occurs for the reactants at rest at infinite separation, $W_i(E^*)$ is the sum of states for transition state $i = D, R$ with threshold energies $E_D^* = 0$ and $E_R^* = E_0$, $\rho(E^*)$ is the PC density of states, and h is the Planck's constant.

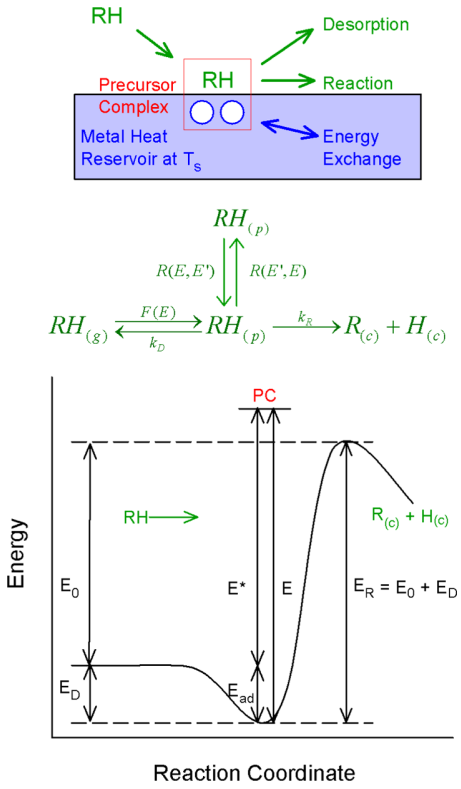

Figure 3-3 Schematic describing the energetics and reaction scheme for precursor-mediated microcanonical trapping (PMMT) models of alkane dissociative chemisorption. Upon striking the surface, an impinging molecule interacts with a small number of local surface oscillators, s, forming a transient precursor complex (PC) that, treated on a microcanonical basis, can go on to react, desorb, or exchange energy with the surrounding metal atoms.

For activated dissociative chemisorption of sufficiently small molecules, ultrafast desorption time scales at energies sufficient to react allows energy transfer between the PCs formed and the surrounding surface to be ignored.[19, 21, 23] A complication for small molecules is they can exhibit dynamical biases away from statistical behavior, and a dynamically biased (d-) PMMT model has been developed to treat such cases.[21, 23, 27] Some PMMT model parameters typically need to be derived from experiments, but parameterization has been minimized by using density functional theory (DFT) calculated

transition state vibrational frequencies. For alkanes with DFT determined transition state frequencies, d-PMMT models typically require three parameters, $\{E_0, s, \eta_v\}$, where E_0 is the reaction threshold energy, s is the number of surface oscillators in the PC, and η_v is the efficacy of molecular vibrational energy to promote reactivity relative to translational energy directed along the surface normal. These parameters were fixed by minimizing the average relative discrepancy (ARD) between simulated theoretical and experimental dissociative sticking coefficients,

$$ARD = \frac{|S_{theory} - S_{expt}|}{\min\left(S_{theory},\ S_{expt}\right)} \tag{3.6}$$

for the effusive molecular beam experiments performed in this article at different surface and gas temperatures.

Once these few parameters are determined by PMMT simulations to a limited set of experimental data, they can be used to simulate or predict reactivity under any other arbitrary thermal or nonequilibrium experimental conditions.[21, 23] For all the PMMT models of methane dissociative chemisorption considered in this article, molecular translations parallel to the surface were treated as spectators degrees of freedom. Following the findings for the CH_4/Pt(111) system, molecular rotations were also treated as spectators.

The theoretical sticking coefficient for a particular experiment is

$$S_{theory} = \int_0^{E^*} S(E^*) f(E^*) dE^* \tag{3.7}$$

where $S(E^*)$ is the microcanonical sticking coefficient,

$$S(E^*) = \frac{k_R(E^*)}{k_R(E^*) + k_D(E^*)} = \frac{W_R(E^*)}{W_R(E^*) + W_D(E^*)} \tag{3.8}$$

and $f(E^*)$ is the probability distribution for forming PCs with exchangeable energy E^*.

$$f(E^*) = \int_0^{E^*} f_n(E_n) \int_0^{E^*-E_n} f_s(E_s) \times f_v\left(\eta_v^{-1}(E^* - E_n - E_s)\right) dE_s dE_n \tag{3.9}$$

For the specific case of Rh(111), it became apparent that the step sites and terrace sites have different reactivities. The theoretical sticking coefficient was taken to be the sum of sticking attributed to the two different kinds of sites as follows

$$S_{theory} = \int_0^{E^*} [(1 - \theta_d) S_{terrace}(E^*) + \theta_d \times S_{steps}(E^*)] f(E^*) dE^* \tag{3.10}$$

θ_d is the defects coverage. In this case, the crystal was cut to 0.1° precision. The defect coverage was estimated as $\theta = \arctan(0.1°) = 0.0017$ ML and attributed to steps.

To account for tunneling through the barrier to dissociative chemisorption, the RRKM rate constant for dissociative chemisorption was written in its generalized form as

$$k_R(E) = \frac{W_R(E)}{h\rho(E)} = \int_0^E p(e_t) k_R(E, e_t) de_t = \frac{1}{h\rho(E)} \int_0^E p(e_t) \rho_R(E - e_t) de_t \tag{3.11}$$

where $E = E^* + Z_{Re}$ is the classical energy above the electronic potential energy surface whose zero is set by the well-separated reactants at T = 0 K; e_t is the translational energy along the reaction coordinate leading to separated products; $p(e_t)$ is the tunneling probability; and $\rho_R(E - e_t)$ is the density of states, excluding the reaction coordinate mode, of the reactive transition state evaluated at the energy available to populate vibrational states of the transition state complex when tunneling occurs at e_t. The barrier to

chemisorption was approximated by a 1D Eckart potential whose height was $E_c = E_0 - (Z_{TS} - Z_{Re})$, while the curvature and exothermicity were fixed by DFT. The analytic expression for the tunneling probability through a 1D Eckart barrier relates to e_t above the classical electronic potential evaluated for the well-separated reactants, without regard to zero-point energies, and so the sum the states for the reactive transition state referenced to the E^* energy scale is written as

$$W_R(E^*) = \int_0^{E^*+Z_{Re}} p(e_t)\rho_R(E^* + Z_{Re} - e_t)de_t \tag{3.12}$$

where the argument of ρ_R is the energy available to populate vibrational states of the transition state complex, taking into account their vibrational zero-point energy. Tunneling was not relevant to calculation of $W_D(E^*)$ for molecular desorption because there is no barrier for intact molecular adsorption/desorption that rises above the E^* energy floor defined by the infinitely separated molecule and surface.

3.4 Results

3.4.1 Direct sticking coefficient

The measured direct sticking coefficient is tabulated below:

T_g↓ T_s→	450	500	550	600	700	800	900
300 ambient		4.7E-08	6.8E-08	8.91E-08	2.56E-07	4.34E-07	5.79E-07
450	2.47E-07						
500		6.68E-07		9.18E-07	1.33E-06	1.94E-06	3.28E-06
550			1.89E-06				
600		1.69E-06		2.35E-06	3.62E-06	7.14E-06	1.03E-05
700		2.67E-06		5.63E-06	1.11E-05	1.24E-05	2E-05
800		1.09E-05		2.53E-05	2.79E-05	4.6E-05	5.47E-05
900		3.02E-05		4.21E-05	7.09E-05	8.75E-05	0.000129

Table 3-2 Direct sticking coefficient, columns: surface temperature, rows: gas temperature

Qualitatively, changing gas temperature has a bigger effect on reactivity than changing the surface temperature. To the authors' surprise, the slopes of the curves at each individual gas temperature do not vary much as the theory predicted.

According to Tolman relation,

$$E_a(T_i) = < E_i(T_i) >_R - < E_i(T_i) > \tag{3.13}$$

where $< E_i(T_i) >_R$ is the mean energy of the transition state that reacts and $< E_i(T_i) >$ is the mean energy of all transition states. The effective activation energy of either gas or surface, $E_a(T_i)$, can be calculated from experimental measurements via,

$$E_a(T_i) = -R \frac{\partial(ln[S(T_i)])}{\partial(\frac{1}{T_i})} \tag{3.14}$$

where R is the ideal gas constant. The effective activation energies with respect to varying surface temperatures at a fixed gas temperature ranging from 500K-900K were found to be from 13 – 19 kJ/mol; E_a at 300K ambient dosing was found to be 25 kJ/mol.

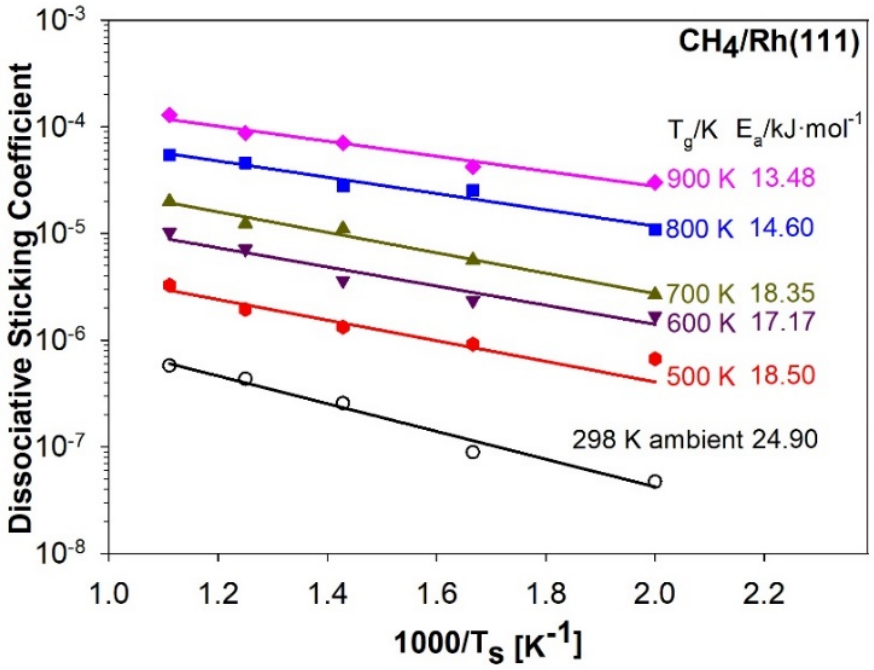

Figure 3-4 Experimental dissociative sticking coefficient (points) and Arrhenius plots to fixed gas temepratures with activation energy. The activation energy decreases with increasing gas temperature.

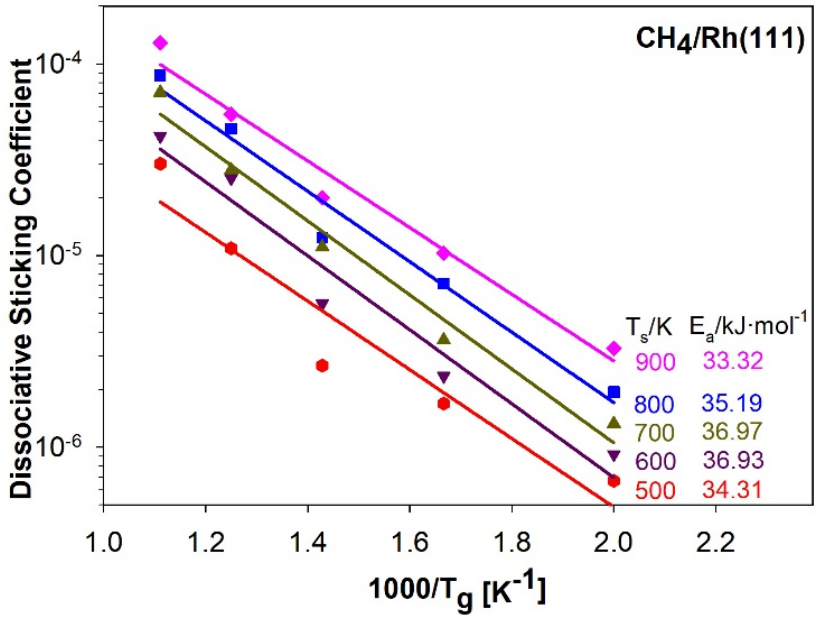

Figure 3-5 Arrhenius plots to fixed surface temepratures with activation energy. The activation energy remains the same for different surface temperatures.

With parameters {E_0 = 62.7 kJ/mol, number of surface oscillators s = 1, and vibrational efficacy $\eta_v = 0.1$}, the PMMT was found to fit the best, with an average relative discrepancy (ARD) of 1.08. Although high temperatures (above 600K) fit fairly well, the model fits poorly at lower temperatures. The experimental sticking coefficients from 500K doser and 298K ambient gas vary relatively moderate with respect to surface temperature, whereas the theory sees much steeper change.

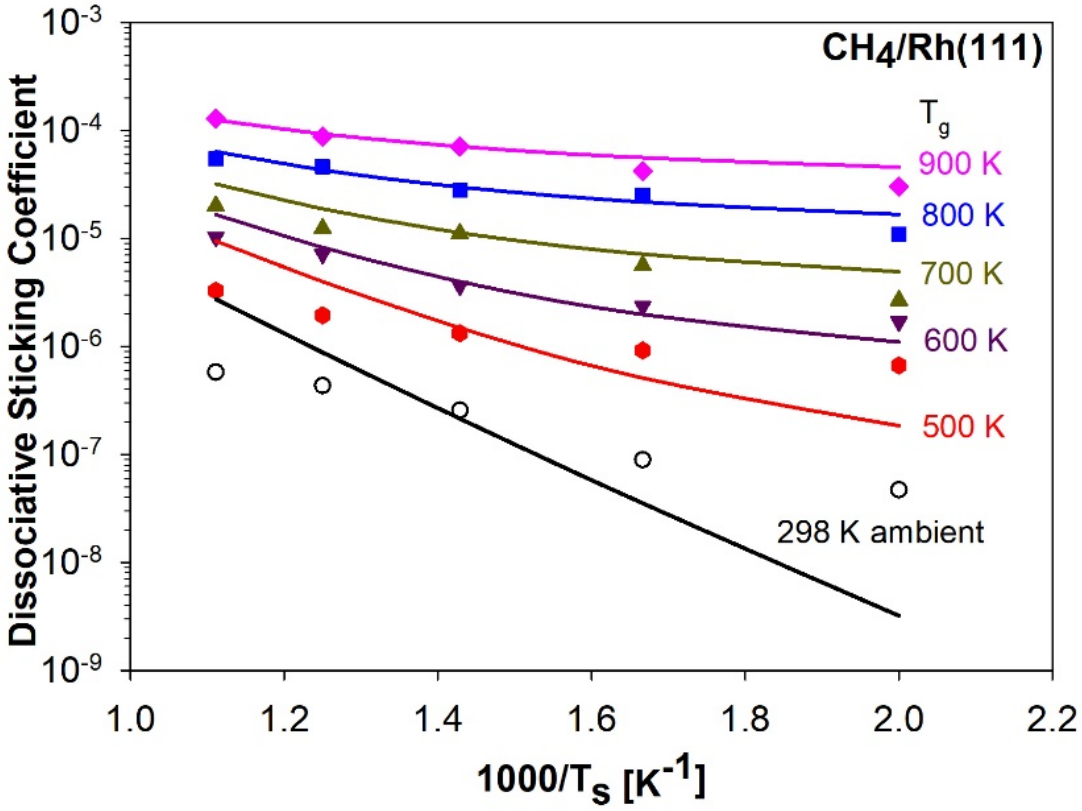

Figure 3-6 Experimental dissociative sticking coefficients (points) and PMMT calculated values (lines) with parameters {threshold energy E_0 = 0.65eV, surface oscillator s = 1, vibrational efficacy η_v= 0.05} for terrace sites. Effusive molecular beam experiments were directed along the surface normal.

3.4.2 Angle-resolved sticking coefficient

Angle-resolved sticking coefficient experiments revealed the relative importance of normal translational energy as compared to other forms of energies in promoting reactivity, because only normal translational energy varies with the incident angle. Although the translational and internal energy distributions of molecules striking a surface under thermal equilibrium conditions is independent of incident angle, the distribution of normal translational energy varies with angle as:

$$P(E_n, T_\vartheta) = (RT_\vartheta)^{-2} E_n e^{-E_n/RT_\vartheta} \text{ where } T_\vartheta = T\cos^2\vartheta \tag{3.15}$$

Consequently, angular distribution experiments are revelatory to the relative importance of normal translational energy in promoting reactivity. If normal translational energy doesn't promote reactivity, there would be no angular variation of dissociative sticking coefficient. Whereas if normal translational energy is the dominant promoter of reactivity, the dissociative sticking coefficient would fall rapidly due to the decreasing of the effective temperature T_ϑ.

The sticking coefficient from -14 to 24 degrees were measured with the center of the crystal being 1.0 mm from the centerline of the doser; the value from 8.5 to 40 degrees were acquired with the center of the crystal being 6.0 mm from the centerline of the doser. The value from 8 to 24 degrees is the average of two experiments.

angle/°	S0
-14.0362	7.64E-06
-8.53077	9.93E-06
-2.86241	1.14E-05
2.862405	1.08E-05
8.530766	9.41E-06
14.03624	7.71E-06
19.29005	6.33E-06
24.22775	5.72E-06
28.81079	4.77E-06
33.02387	4.23E-06
40.36454	2.88E-06

Table 3-3 sticking coefficient at T_g=T_s=700K with different angles

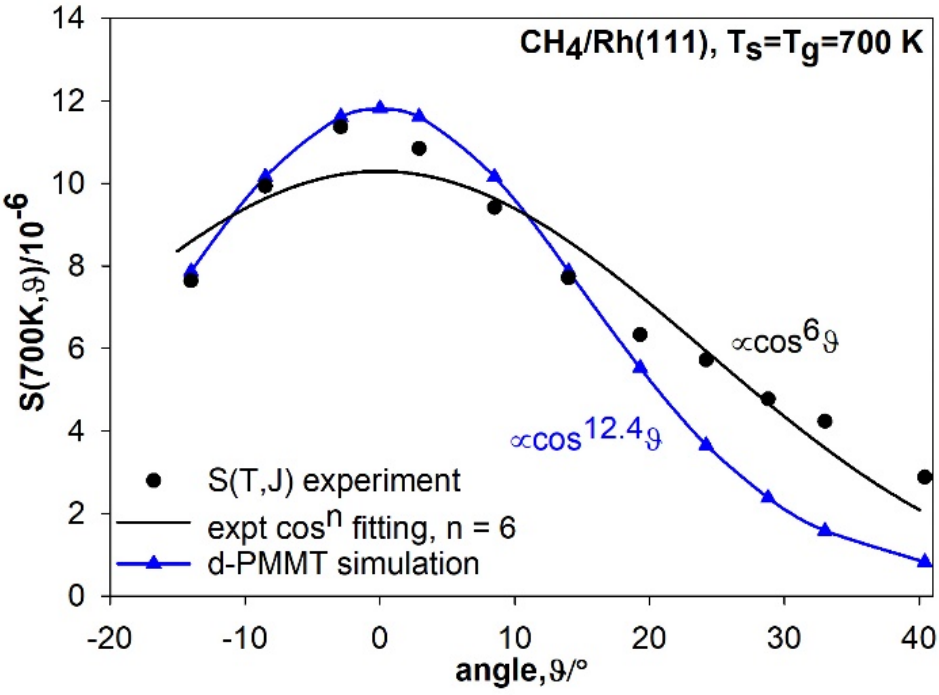

Figure 3-7 PMMT model without defect sites (blue) v.s. experimental sticking coefficient (black dots) at T_g=T_s=700K, angular distribution.

The cosine dependent was found to be cosine to the 6.0th power, which was much lower than on Pt(111), $\cos^{14.5}\vartheta$.[28] Using the same parameters {E_0 = 0.65eV, s = 1, η_v =

0.05} for PMMT model, fitting is acceptable at small angles (high E_n), discrepancy gets bigger at large angles (low E_n).

In comparison, angle-resolved sticking coefficients were acquired for 800K and 900K too. The cosine dependence decreases from 6 to around 4. At high temperature, vibrational energy and surface energy are also high and remain the same regardless of impinging angle; so, at higher angle, even if the translational energy is discounted greatly, there's still enough energy from vibration and the surface to overcome the activation barrier. However, no distinguishing difference was observed in 800K and 900K.

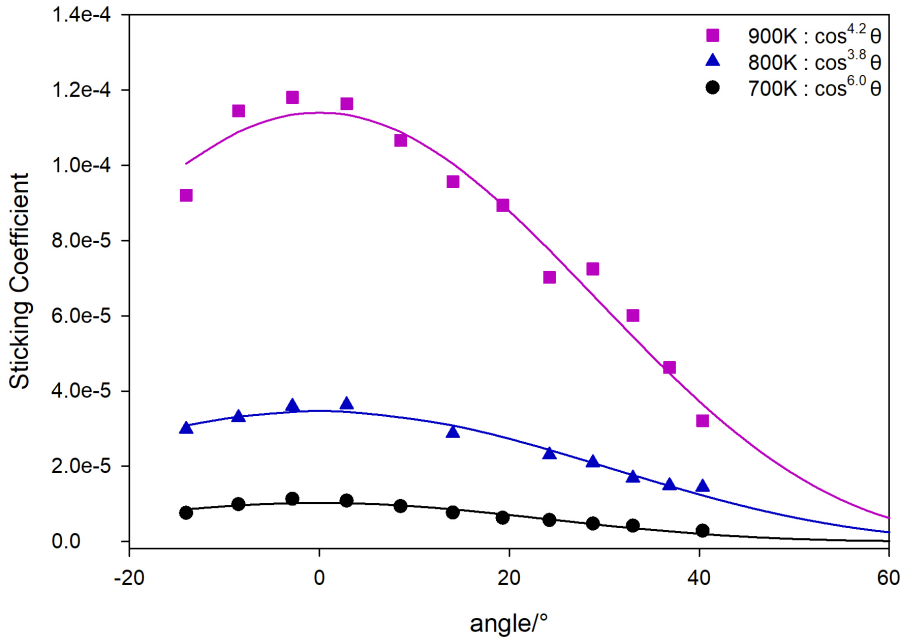

Figure 3-8 absolute angle-resolved sticking coefficient at 700K, 800K, and 900K

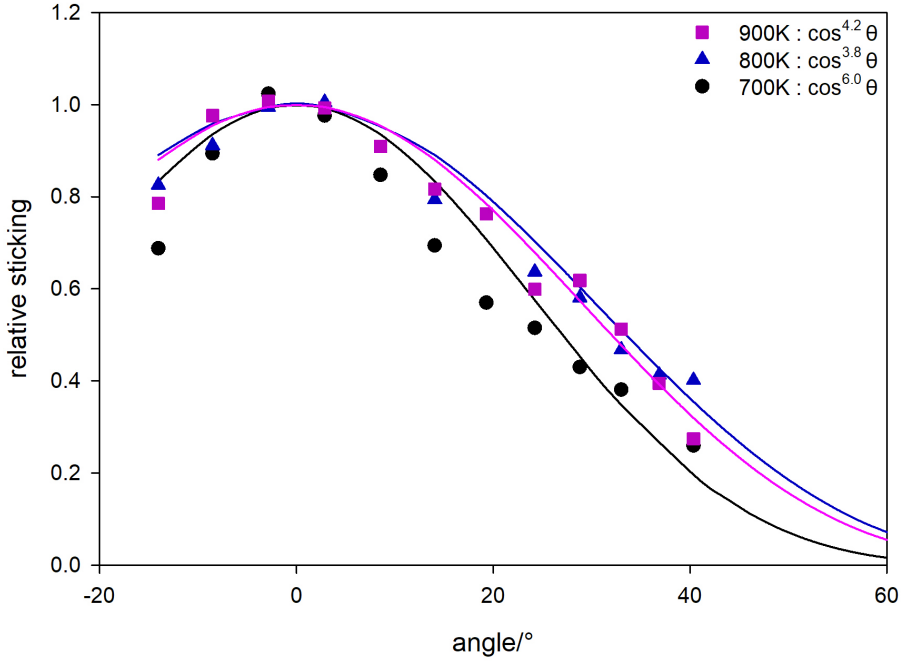

Figure 3-9 relative angle-resolved sticking coefficient, all scaled to 1, at 700K, 800K, and 900K

3.4.3 Dual channel activation

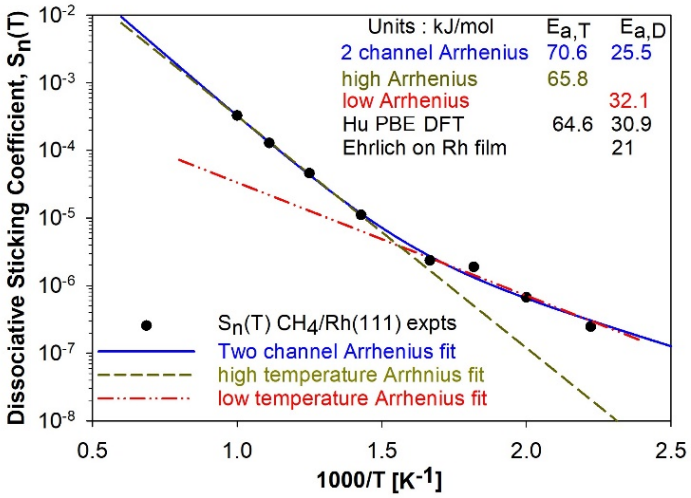

Figure 3-10 Extended equilibrium (T_s=T_g) experiments (1000K – 450K)

With equilibrium experiments $S_n(T_g=T_s)$ over a wider range, we can see there could be two Arrhenius domains with a turning point between 600K and 700K. The data fit well to a two channel Arrhenius form, $S = S_T \exp\left(\frac{E_{a,T}}{RT}\right) + S_D \exp\left(\frac{E_{a,D}}{RT}\right)$, with the parameter $\{S_1=1.529, E_{a1}=70.6$ kJ/mol, $S_2=2.69\times10^{-5}$, $E_{a2}=25.5$ kJ/mol$\}$, which suggests there could be two reaction channels. If fitted to single channels over different domains, the activation energies were $E_{a\_high}=65.8$ kJ/mol and $E_{a\_low}=32.1$ kJ/mol, respectively. These activation energies are comparable to DFT calculations by Hu[17], where $E_{a\_terrace}=64.6$ kJ/mol and $E_{a\_step}=30.9$ kJ/mol.

unit: kJ/mol	$E_{a,T}$	$E_{a,D}$	ΔE
Two-channel Arrhenius	70.6	25.5	45.1
High T Arrhenius	65.8		33.7
Low T Arrhenius		32.1	
Hu PBE DFT	64.6	30.9	33.7
Ehrlich Rh film expts		21	

Table 3-4 activation energies for step and terrace sites.

3.5 Validation of Sticking Coefficient

3.5.1 Dosing at different distance

In order to test the reproducibility of the data acquired, a dosing experiment at different dosing distance was done at surface temperature of 900K where it's most likely subject to background contamination.

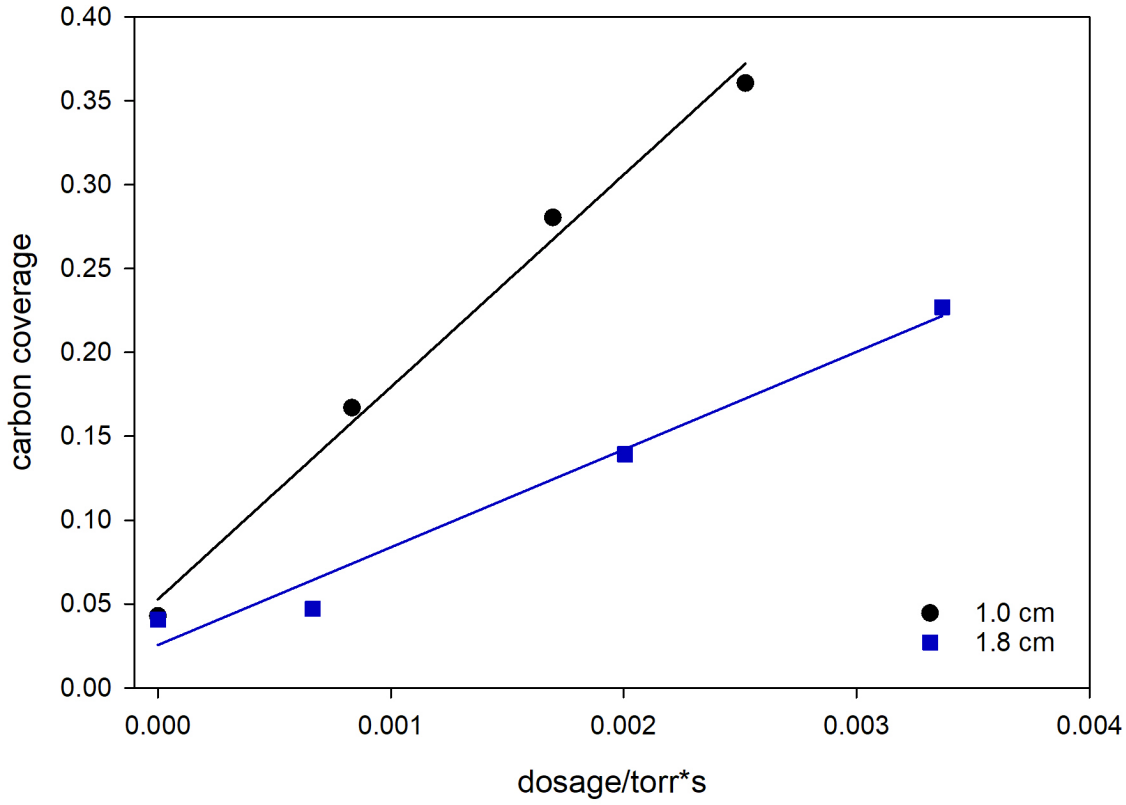

Figure 3-11 Carbon coverage increase at different dosing distances

As seen on figure 3-11, carbon coverage increases slowly when dosing at a further distance. This is because when the surface is further away from the doser, the molecular density of the beam hitting the surface decreases hence resulting in less molecules reacting on the surface. Although the apparent sticking coefficient is lower for further distanced dosing (2.55×10^{-4} for 1.8 cm and 5.54×10^{-4} for 1.0 cm), the flux ratio is also lower (1.47 at 1.8 cm and 4.77 at 1.0 cm), the final sticking coefficient, taking background sticking coefficient and flux ratio in, of the two is close, with 1.0 cm dosing of 1.16×10^{-4} and 1.8 cm dosing of 1.73×10^{-4}. These results are comparable to another experiment done several months apart, where the sticking coefficient is 1.29×10^{-4} (dosing distance of 1.0 cm).

3.5.2 Heating 700K carbon angular distribution to 900K

The angle-resolved sticking coefficient at 800K and 900K are both broad and have the same cosine dependence. Aside from high vibrational energy and high surface energy, carbon diffusion across the surface could also cause the angular distribution to broaden. To eliminate this possibility, an angle-resolved experiment was done at 700K to acquire a surface with a carbon deposition distribution. The surface is subsequently heated to 700K, 800K, and 900K for 10 minutes, respectively. The carbon concentrations at three spots were measured after heating. All three spots measured showed no change after heating at 700K for 10 minutes; less than 0.4% increase even after heating at 800K for 10 minutes; less than 0.7% increase even after heating at 900K for 10 minutes. The result showed that there's no carbon diffusion laterally on the Rh(111) surface, indicating that the broadening angular distribution was from methane reacting on the impinging spot, not from carbon migrating from an area with higher concentration to an area with low concentration. The even carbon concentration increases across the surface after heating at temperature higher than 800K might be from the fluctuations in AES measurements or carbon migration from the bulk to the surface.

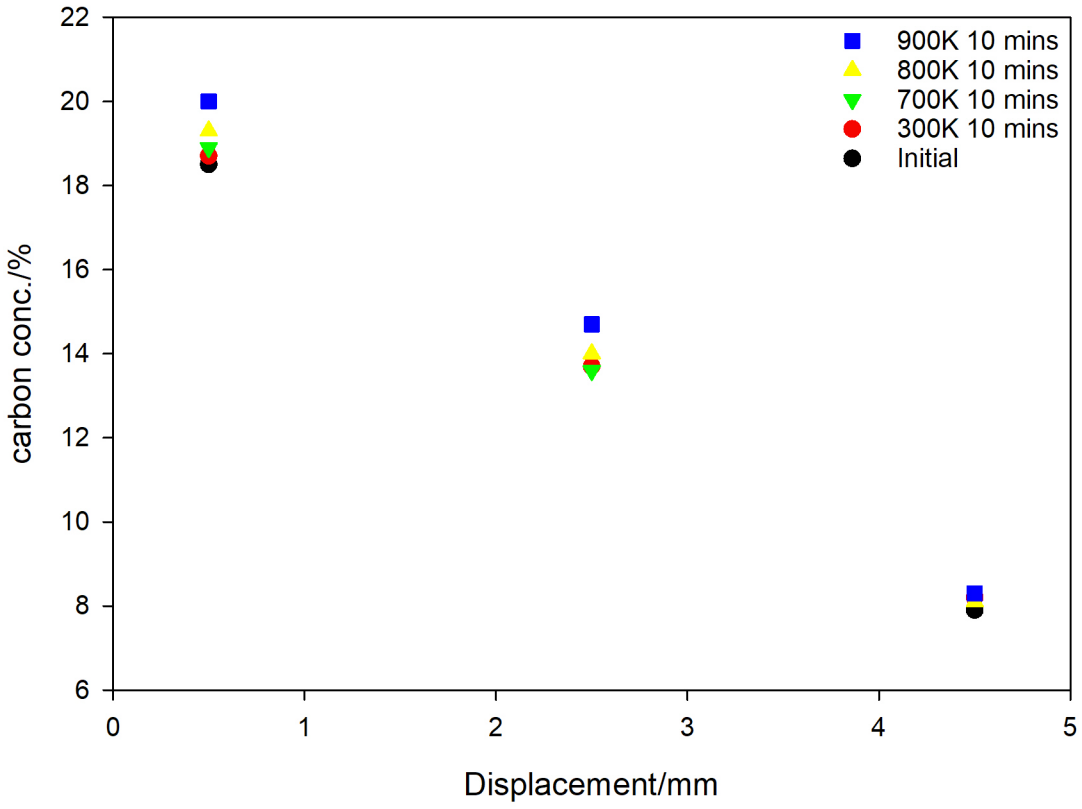

Figure 3-12 Carbon concentration change with different heating time. The 300K, 700K, 800K, and 900K heating were done sequentially, in that order.

3.6 Terrace and Defect Channel

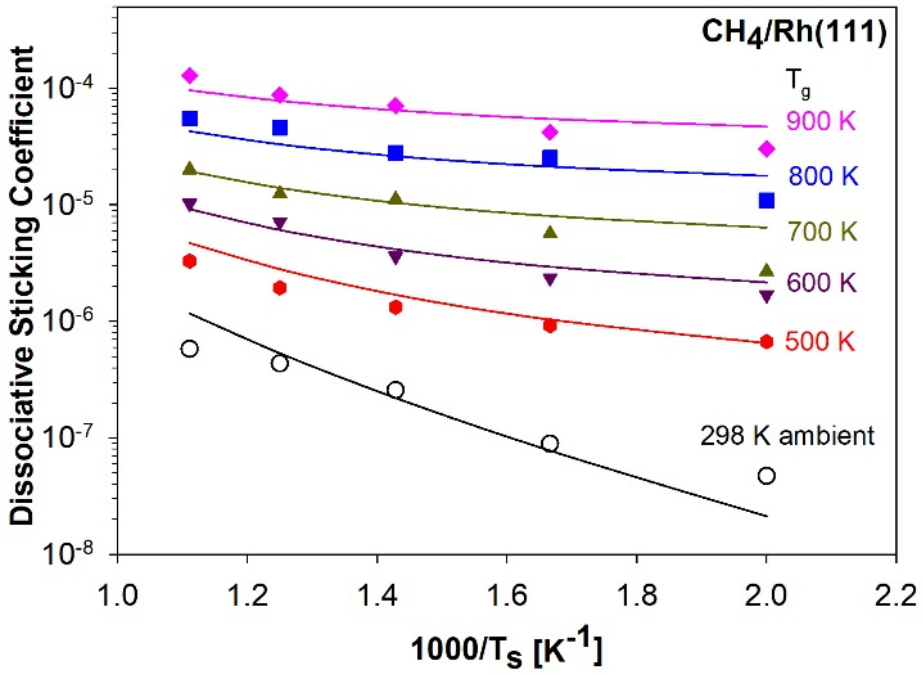

Figure 3-13 Experimental dissociative sticking coefficients (points) and PMMT calculated values (lines) with parameters {threshold energy at terrace $E_{0,terrace}$ = 74.3 kJ/mol, threshold energy at step $E_{0,step}$ = 36.7 kJ/mol, surface oscillator s = 1, vibrational efficacy η_v= 0.55} for both terrace and step sites. Agreement is good across all temperatures in question, even for 300K ambient dosing.

Although the two Arrhenius simulation fit well to the equilibrium (T_s=T_g) data, it introduced two more parameters. What is more, it does not explain the sticking coefficients at non-equilibrium temperatures; nor does it fit the thermal sticking coefficient data done by Ehrlich[12]. Here, an PMMT model with an extra parameter, threshold energy on the step sites, was introduced, and it fit better to the experiments. (Figure 3-13)

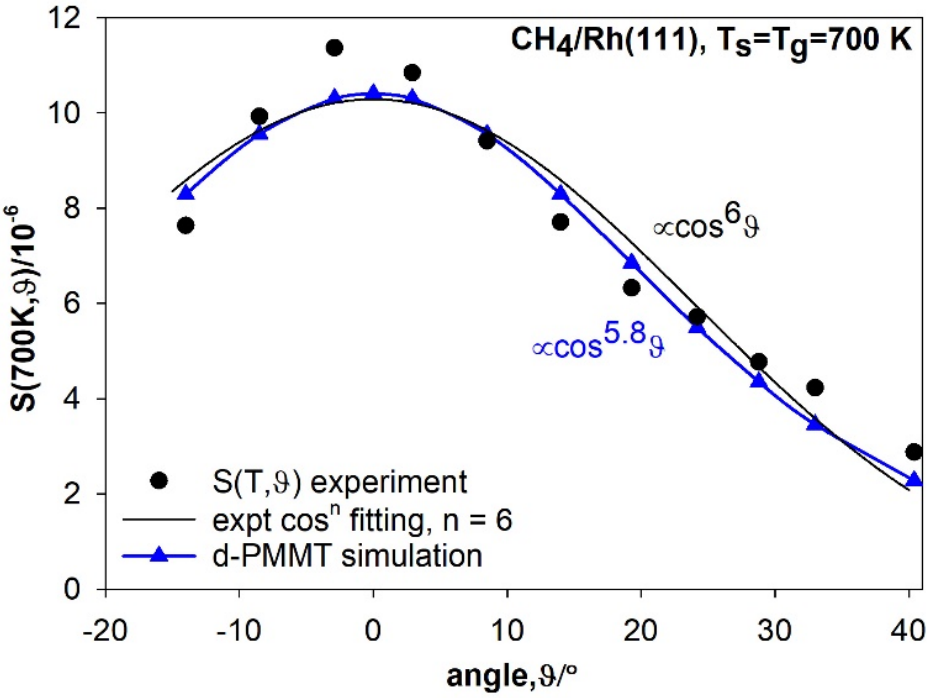

Figure 3-14 PMMT model with defect sites (black) v.s. experimental sticking coefficient (blue dots) at T_g=T_s=700K, angular distribution. Solid blue line is the numeric fitting to experimental data.

Model and experiments also agree well for angular distribution. (Figure 3-14) It fits the best when terrace threshold energy is 74.3 kJ/mol, step sites threshold energy is 36.7 kJ/mol, and vibrational efficacy is 0.55, with an ARD of 0.271.

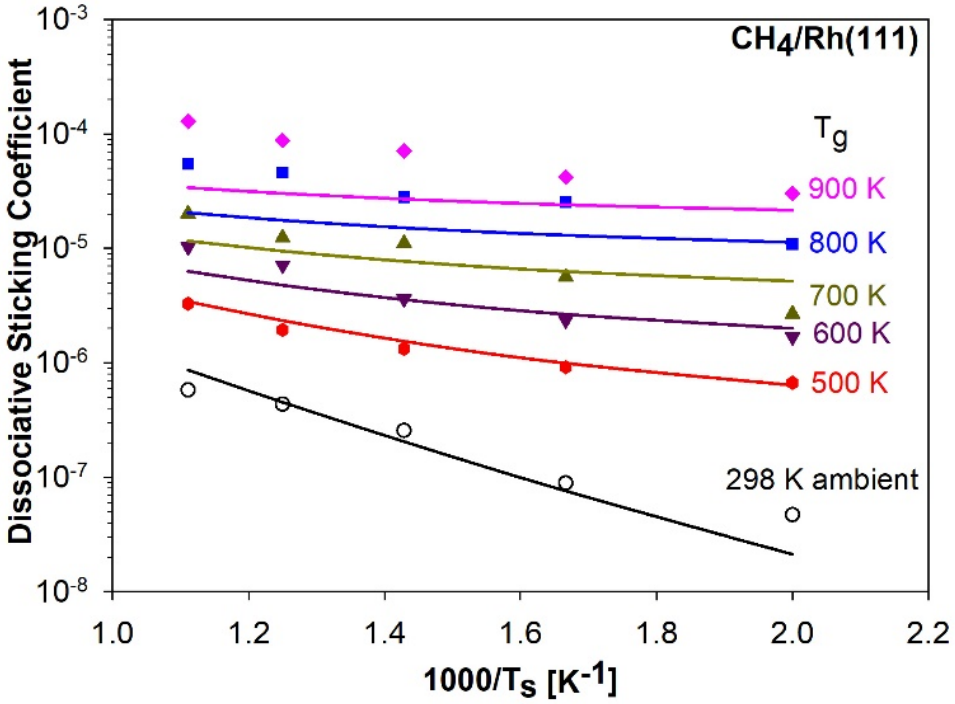

Figure 3-15 PMMT model showing only the defect sites reactivity.

According to PMMT modelling, defect sites play a significant role in promoting C-H bond cleavage in methane. In fact, at lower temperatures (600K and below), defect sites are the main reacting sites rather than terraces, which is surprising especially when how small amount of defects counts in the whole system is considered. Similar effect was observed for angular distribution experiments at 700K.

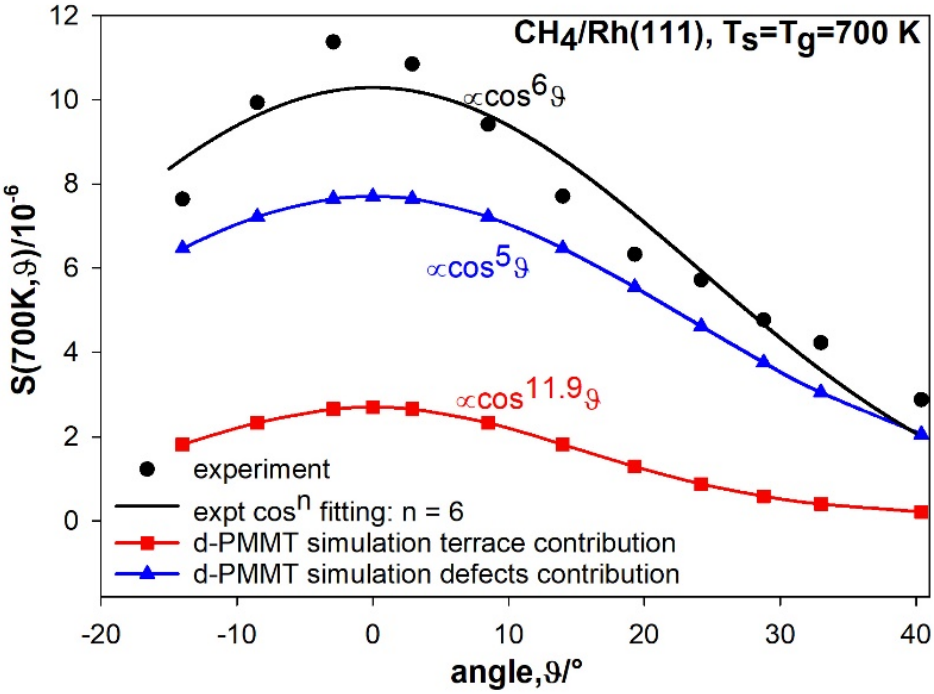

Figure 3-16 PMMT simulation showing the contribution from defects and terrace respectively.

When the impinging angle of the molecules increases, the normal translational energy is effectively discounted, similar to the effects of decreasing the temperature, whereas vibrational energy remains unchanged. The angular distribution experiment shows that at higher angles (lower temperatures), defect sites made up more fraction of the reactivity observed. Reactivity on the terrace also decreases at a much faster rate when angle increases ($\propto\cos^{11.9}\vartheta$), whereas on the step sites, reactivity only decreases to $\propto\cos^{5}\vartheta$, indicating different reaction mechanism on these sites.

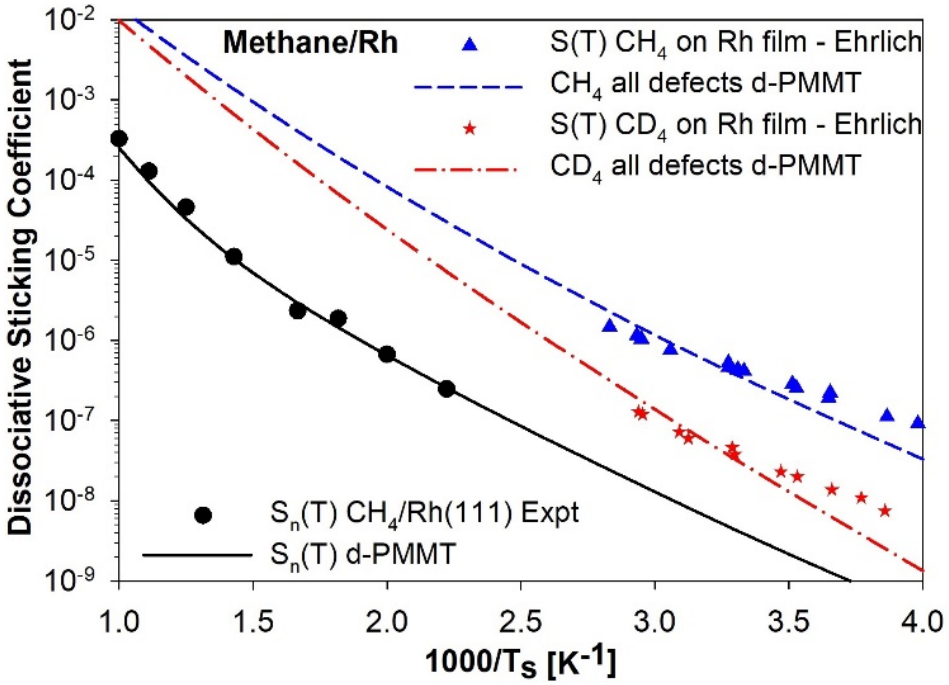

Figure 3-17 Kinetic isotope effects. The PMMT simulation predicts the sticking coefficient on Rh film experiments for both CH_4 and CD_4 closely.

One thing worth noting is that effusive beam sticking coefficient experiments $S_n(T)$ measured along the surface normal are not equal to thermal sticking experiments with an ambient gas S(T). Averaging the $S(\vartheta;T)$ measurements over the angular flux distribution of an ambient gas hitting a surface under thermal equilibrium condition allows for calculation of the thermal dissociative sticking coefficient S(T):

$$S(T) = \int S(\vartheta;T)\frac{cos\vartheta}{\pi}d\Omega \tag{3.16}$$

Here, PMMT simulates much wider temperature range than the experiments limits. Although direct sticking coefficient is beyond detection limit on this Rh(111) surface, Ehrlich[12] did the thermal experiments S(T) at near room temperatures on a Rh film, where all the surface site can be considered as 100% defect or step sites. With the same set of

parameters extracted from the data set of this work, a PMMT model of a step reactivity surface is able to replicate Ehrlich's data closely, further attesting to the robustness of the model. Furthermore, the PMMT model also replicates Ehrlich's CD_4 experiments well, which allows for an investigation of the kinetic isotope effect at relatively low temperatures. Thermal sticking coefficient on metal terrace sites falls off so quickly with decreasing temperature that they become impractical or impossible to measure at low T_s where tunneling is likely important. However, the enhanced reactivity of step or defect sites on Ehrlich's Rh film surface allowed for reactivity measurements near room temperature.

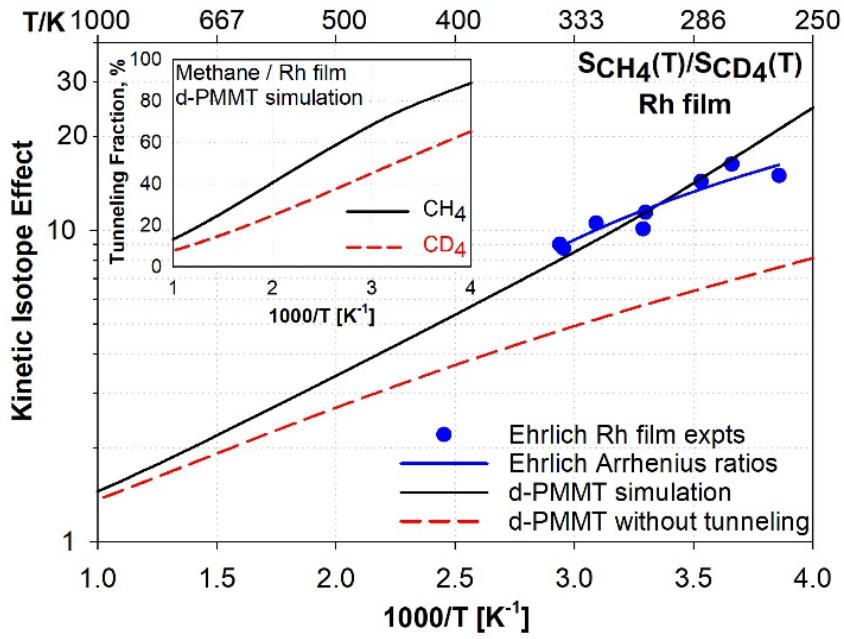

Figure 3-18 Kinetic isotope effects. PMMT simulation predict higher KIE at lower temperature, which agrees with Ehrlich's experimental data. KIE at higher temperature is predicted to be non-significant.

PMMT simulates kinetic isotope effects from 7 to 24 in the temperature range 350 – 250K. This is comparable to Ehrlich's experiment value (8-15 in the temperature range 340 – 260K). The experimental kinetic isotope effect is much higher than what can be accounted for based on the zero-point energy isotope effects alone (7 - 8), indicating that tunneling is participating in the activation process.

PMMT indicates that at 250K, 88% of successfully reacting CH_4 do so by tunneling. This fraction is still significant at 65% for CD_4. However, at temperatures more appropriate to industrial processes near 800K, tunneling accounts for 20% of the reactive trajectories for CH_4.

3.7 Sputtered Surface

PMMT model and DFT calculation suggested that activation energy on defect sites is different from terrace sites. PMMT model further indicates that at low temperatures, defect sites are the main reactive sites, rather than terrace sites, even though defect sites only count for 0.17% of the surface sites. Changing the amount of defect sites should also change the reactivity and can be reflected in a change in sticking coefficient. Here, we attempted to change the defect density by argon ion sputtering at 700K at 5×10^{-5} torr for 10 minutes. The sticking coefficient of the sputtered surface was three times that of the annealed surface. More detailed experiments on a sputtered surface is discussed in the next chapter.

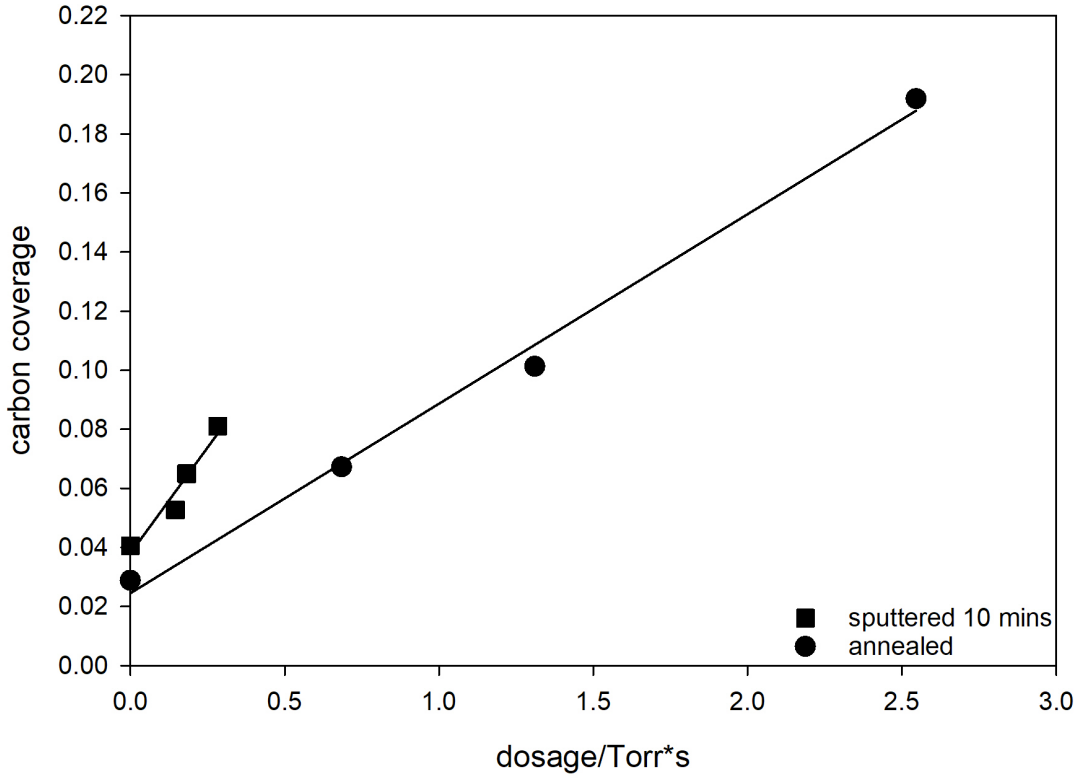

Figure 3-19 Carbon coverage with dosage of sputtered and annealed surfaces

3.8 Conclusion

The methane activation on Rh(111) study provided direct experimental dissociative sticking coefficients on a single crystal surface which was never done before. The single crystal surface, oriented to 0.1º with a nominal step density of 0.17%, had a reactivity dominated by steps at temperatures below about 700 K. The experiments were found to be optimally fit with a two channel dynamically-biased PMMT model accounting for the low step density and with parameters ($E_{0,terrace}$ = 74.3 kJ/mol, $E_{0,step}$ = 36.7 kJ/mol, s = 1, η_v= 0.55), where s=1 could be fixed in advance by the DFT calculated transition state structure, and the reaction threshold energies are for the terrace and step defects, while the vibrational

efficacy value was taken as shared for both reaction sites. Unlike Pt(111), the step sites are not readily poisoned on Rh(111) but rather contribute steadily to the reactivity even as substantial coverages of carbon accumulate at the surface (up to 0.3 ML). The threshold energies, especially their difference, compare well to Hu's DFT calculation of activation energies for the Rh(111) terrace and step sites of 64.6 kJ/mol and 30.9 kJ/mol, respectively.[17] Ehrlich's measurements of methane thermal reactivity on "defects dominated" deposited Rh film surfaces[12] were reproduced by d-PMMT simulations assuming film sites are 100% defects with the Rh(111) step characteristics. The high kinetic isotope effect (9-15) observed in Ehrlich's relatively low temperature experiments were reproduced and the importance of tunneling was quantified with the d-PMMT model. The finding that the vibrational efficacy extracted from our Rh(111) experiments matched previous prediction by Scott[29] based on correlations to DFT calculated transition state geometries represents progress towards the reverse process of DFT calculations predicting parameters for d-PMMT models that can accurately predict experimental outcomes, including ones far from equilibrium. The remarkable activity of steps in the reactivity of CH_4 on Rh(111) but not on Pt(111) helps explain why CH_4 steam reforming turnover frequencies on metal nanoparticle catalysts increases with dispersion much more rapidly for Rh than for Pt.[30]

Reference

1. Mhadeshwar, A. B.; Vlachos, D. G., A Catalytic Reaction Mechanism for Methane Partial Oxidation at Short Contact Times, Reforming, and Combustion, and for Oxygenate Decomposition and Oxidation on Platinum. *Ind Eng Chem Res* **2007**, *46*, 5310-5324.
2. Maestri, M.; Vlachos, D. G.; Beretta, A.; Forzatti, P.; Groppi, G.; Tronconi, E., Dominant Reaction Pathways in the Catalytic Partial Oxidation of Ch4 on Rh. *Top Catal* **2009**, *52*, 1983-1988.
3. Goetsch, D. A.; Schmidt, L. D., Microsecond Catalytic Partial Oxidation of Alkanes. *Science* **1996**, *271*, 1560-1562.
4. Schwiedernoch, R.; Tischer, S.; Correa, C.; Deutschmann, O., Experimental and Numerical Study on the Transient Behavior of Partial Oxidation of Methane in a Catalytic, Monolith. *Chem Eng Sci* **2003**, *58*, 633-642.
5. Hickman, D. A.; Schmidt, L. D., Steps in Ch4 Oxidation on Pt and Rh Surfaces - High-Temperature Reactor Simulations. *Aiche J* **1993**, *39*, 1164-1177.
6. Deutschmann, O.; Schmidt, R.; Behrendt, F.; Warnatz, J., Numerical Modeling of Catalytic Ignition. *Twenty-Sixth Symposium (International) on Combustion, Vols 1 and 2* **1996**, 1747-1754.
7. Deutschmann, O.; Schmidt, L. D., Modeling the Partial Oxidation of Methane in a Short-Contact-Time Reactor. *Aiche J* **1998**, *44*, 2465-2477.
8. Stewart, C. N.; Ehrlich, G., Dynamics of Activated Chemisorption - Methane on Rhodium. *J Chem Phys* **1975**, *62*, 4672-4682.
9. Thiel, P. A.; Williams, E. D.; Yates, J. T.; Weinberg, W. H., The Chemisorption of Co on Rh(111). *Surf Sci* **1979**, *84*, 54-64.
10. Brass, S. G.; Reed, D. A.; Ehrlich, G., Vibrational-Excitation and Surface Reactivity - Examination of the Nu-3 and 2nu-3 Modes of Ch4. *J Chem Phys* **1979**, *70*, 5244-5250.
11. Brass, S. G.; Ehrlich, G., Activated Chemisorption - Internal Degrees of Freedom and Measured Activation-Energies. *Phys. Rev. Lett.* **1986**, *57*, 2532-2535.
12. Brass, S. G.; Ehrlich, G., Dissociative and Molecular Adsorption of Methane on Rhodium. *Surf Sci* **1987**, *187*, 21-35.
13. Bunnik, B. S.; Kramer, G. J., Energetics of Methane Dissociative Adsorption on Rh{111} from Dft Calculations. *J Catal* **2006**, *242*, 309-318.
14. van Grootel, P. W.; van Santen, R. A.; Hensen, E. J. M., Methane Dissociation on High and Low Indices Rh Surfaces. *J Phys Chem C* **2011**, *115*, 13027-13034.
15. Fechete, I.; Wang, Y.; Vedrine, J. C., The Past, Present and Future of Heterogeneous Catalysis. *Catal Today* **2012**, *189*, 2-27.
16. Zhu, T.; van Grootel, P. W.; Filot, I. A. W.; Sun, S.-G.; van Santen, R. A.; Hensen, E. J. M., Microkinetics of Steam Methane Reforming on Platinum and Rhodium Metal Surfaces. *J Catal* **2013**, *297*, 227-235.
17. Liu, Z. P.; Hu, P., General Rules for Predicting Where a Catalytic Reaction Should Occur on Metal Surfaces: A Density Functional Theory Study of C-H and C-O Bond Breaking/Making on Flat, Stepped, and Kinked Metal Surfaces. *J Am Chem Soc* **2003**, *125*, 1958-1967.
18. Abbott, H. L.; Bukoski, A.; Harrison, I., Microcanonical Unimolecular Rate Theory at Surfaces. Ii. Vibrational State Resolved Dissociative Chemisorption of Methane on Ni(100). *J Chem Phys* **2004**, *121*, 3792-810.
19. Bukoski, A.; Blumling, D.; Harrison, I., Microcanonical Unimolecular Rate Theory at Surfaces. I. Dissociative Chemisorption of Methane on Pt(111). *The Journal of Chemical Physics* **2003**, *118*, 843-871.
20. Bukoski, A.; Abbott, H. L.; Harrison, I., Microcanonical Unimolecular Rate Theory at Surfaces. Iii. Thermal Dissociative Chemisorption of Methane on Pt(111) and Detailed Balance. *J Chem Phys* **2005**, *123*, 94707.

21. Donald, S. B.; Navin, J. K.; Harrison, I., Methane Dissociative Chemisorption and Detailed Balance on Pt(111): Dynamical Constraints and the Modest Influence of Tunneling. *J Chem Phys* **2013**, *139*, 214707.
22. Cushing, G. W.; Navin, J. K.; Valadez, L.; Johanek, V.; Harrison, I., An Effusive Molecular Beam Technique for Studies of Polyatomic Gas-Surface Reactivity and Energy Transfer. *Rev Sci Instrum* **2011**, *82*.
23. Donald, S. B.; Harrison, I., Rice-Ramsperger-Kassel-Marcus Simulation of Hydrogen Dissociation on Cu(111): Addressing Dynamical Biases, Surface Temperature, and Tunneling. *J Phys Chem C* **2014**, *118*, 320-337.
24. Ukraintsev, V. A.; Harrison, I., A Statistical Model for Activated Dissociative Adsorption: Application to Methane Dissociation on Pt(111). *The Journal of Chemical Physics* **1994**, *101*, 1564-1581.
25. Bunker, D. L.; Hase, W. L., On Non-Rrkm Unimolecular Kinetics: Molecules in General, and Ch3nc in Particular. *The Journal of Chemical Physics* **1973**, *59*, 4621-4632.
26. Forst, W., *Unimolecular Reactions : A Concise Introduction*; Cambridge University Press: Cambridge, U.K.; New York, 2003.
27. Donald, S. B.; Harrison, I., Dynamically Biased Rrkm Model of Activated Gas-Surface Reactivity: Vibrational Efficacy and Rotation as a Spectator in the Dissociative Chemisorption of Ch4 on Pt(111). *Phys Chem Chem Phys* **2012**, *14*, 1784-95.
28. Navin, J. K.; Donald, S. B.; Tinney, D. G.; Cushing, G. W.; Harrison, I., Communication: Angle-Resolved Thermal Dissociative Sticking of Ch4 on Pt(111): Further Indication That Rotation Is a Spectator to the Gas-Surface Reaction Dynamics. *J Chem Phys* **2012**, *136*, 061101.
29. Donald, S. B. Precursor Mediated Microcanonical Trapping Model of Activated Dissociative Chemisorption at Surfaces: Assessment of Dynamical Effects. University of Virginia, 2013.
30. Jones, G., et al., First Principles Calculations and Experimental Insight into Methane Steam Reforming over Transition Metal Catalysts. *J Catal* **2008**, *259*, 147-160.

4 Ethane Activation on Rh(111) and Carbon Migration

4.1 Introduction

Ethane is the second most abundant component in shale gas, accounting for about 7%.[1-2] The reactive processes involving ethane are more than that of methane, due to the extra carbon and the C-C bond in ethane. In gas phase, the C-C bond is weaker than the C-H bond.

$$C_2H_6 \rightarrow 2CH_3\bullet \quad \Delta H = 369.0\ kJ/mol$$

$$C_2H_6 \rightarrow C_2H_5\bullet + H\bullet \quad \Delta H = 422.6\ kJ/mol\ ^{3}$$

However, it is more valuable to dehydrogenate ethane to make ethylene than to break C-C bond to make single carbon species. Different catalysts can be selective to either C-H bond or C-C bond hence making different products. There are various processes to utilize ethane, such as steam cracking, steam reforming, dry reforming, partial oxidation including oxidative dehydrogenation (ODH), and direct dehydrogenation (DDH).[4]

4.1.1 Steam Cracking

Steam cracking is the most prevalent process to produce ethylene with ethane as a feedstock.[5-6] However, this process is a non-catalytic, radicals-promoted, thermal cracking process, performed in the presence of steam at high temperature and short residence times.

$$C_2H_6 \rightarrow CH_2 = CH_2 + H_2 \quad \Delta H = 136.4\ kJ/mol$$

During the steam cracking operation, highly pressurized steam is used to dilute ethane to suppress coking effects on Ni heating tubes. Because steam cracking reaction is highly endothermic, the reaction is carried out at high temperature (700 – 950 °C) and the

residence time ranges from a few seconds to tenths of a second. The product is a mixture of ethane, ethene, steam, hydrogen, and other hydrocarbons. The mixture is then separated by a series of operations. The reaction goes through a typical chain mechanism for radical reactions:

Initiation:

$$CH_3CH_3 \rightarrow CH_3\bullet + CH_3\bullet$$

Propagation:

$$CH_3CH_3 + CH_3\bullet \rightarrow CH_4 + CH_3CH_2\bullet$$

$$CH_3CH_2\bullet \rightarrow CH_2 = CH_2 + H\bullet$$

$$H\bullet + CH_3CH_3 \rightarrow CH_3CH_2\bullet + H_2$$

Termination:

$$2CH_3CH_2\bullet \rightarrow CH_3CH_2CH_2CH_3$$

$$CH_3CH_2\bullet + H\bullet \rightarrow CH_3CH_3$$

Modern olefin plants, however, still convert more than 10% of ethane into CO_2. And because of the high peak temperature of the flame in the tube furnace, significant pollutants such as NO_x are inevitably produced.[7]

Steam reforming of ethane (ESR) is similar to that of methane:

$$CH_3CH_3 + 2H_2O \rightarrow 2CO + 5H_2$$

ESR is not widely discussed as methane steam reforming. It is a competing reaction for steam cracking, and the product is not as valuable as ethylene.

4.1.2 Dry Reforming

Dry reforming, as the name suggests, is a reforming process without water; instead, CO_2 is used to produce CO and H_2 (syngas)[8]:

$$CH_3CH_3 + 2CO_2 \rightarrow 4CO + 3H_2 \;\; \Delta H = 429.0\ kJ/mol$$

The attractiveness of this process is that it takes two greenhouse gases and produces syngas, which can be used to make higher hydrocarbons via the Fischer-Tropsch process. However, since it is also endothermic, it is only economical to couple the plant with renewable yet unstable energy resources such as solar and wind energy.[9-10] The use of a catalyst is also necessary to avoid very high temperatures and to facilitate the feasibility of the process.[8] What is more, the process produces hydrogen, which reacts with CO_2 to produce water through reverse water gas shift:

$$H_2 + CO_2 \rightarrow CO + H_2O \;\; \Delta H = 41\ kJ/mol$$

that reduces the yield of H_2. Coking is another great challenge in ethane dry reforming. On a Rh/ZSM-t catalyst, significant deactivation occurs within 30 minutes of reaction, at an ethane concentration as low as 6.5%.[11]

4.1.3 Direct Dehydrogenation

Direct dehydrogenation, also referred as catalytic dehydrogenation, is a process that produces alkenes and hydrogen using a catalyst at high temperature.

$$C_2H_6 \rightarrow CH_2 = CH_2 + H_2$$

There are commercially available catalysts that facilitate on-purpose production of propylene with propane, the Olefex (UOP) and the Catofin (Lummus) technologies.[12] Both

technologies use an alumina-supported catalyst: Pt-Sn/Al_2O_3 for Olefex and Cr_2O_3/Al_2O_3 for Catofin. Since the reaction is endothermic and equilibrium-limited, high temperatures and low pressures are favored. The high temperature conditions inevitably lead to coke formation; thus a regeneration step is needed. Although the regeneration is not reversible, the process can run continuously for several years.[13] In 2014, around 5 million tons of propylene is produced by propane dehydrogenation. Other than metal oxide-based catalysts, nanocarbon materials that do not contain any metals are being studied with the hope to develop robust catalysts with high coke resistance.[14] Carbon-based materials have high stability toward deactivation by carbonization. Multi-walled carbon nanotubes (MWCNT), reduced graphene oxide (rGO), activated carbon, and nanodiamonds have been explored and showed high activity and excellent coke resistance.

All dehydrogenation reactions are reversible and have limitations such as thermodynamic restriction on conversion and selectivity, side reactions, strong endothermic main reaction and necessity to supply heat at high temperature, and coke formation and resulting catalyst deactivation.[15]

4.1.4 Partial Oxidation

Partial oxidation of ethane has many products depending on the reaction environment and catalysts used. Oxidative dehydrogenation provides an alternative to produce ethylene from ethane.[7, 16]

$$C_2H_6 + O_2 \rightarrow CH_2 = CH_2 + H_2O \quad \Delta H = -105.4\, kJ/mol$$

The reaction itself is exothermic; it uses oxygen, which is readily available, as a reactant; and the side product is water, making it a good candidate for producing ethylene. On a

platinum-tin catalyst, at least 85% selectivity to ethylene at greater than 80% conversion can be obtained by partial oxidation of ethane by adding large amounts of H_2 to the reaction mixture, at 950°C with a contact time of 10^{-3} seconds. Undesired CO and CO_2 formation also decreased from 20% without H_2 to 5 % when H_2 is added. H_2 is also generated in the successive reactions, so with recycle, no addition H_2 is needed in this process.[7] In a quartz tube, a mixture of ethane and oxygen with nitrogen as carrier gas at 1 atm can react to produce ethylene at above 930K. Ethylene yield is high with excess amount of ethane (above 7:1 oxygen); when oxygen fraction increases in the mixture, more CO and CH_4 are produced. This provided an opportunity for oxidative pyrolysis that allows efficient operation of smaller plants and reduced energy consumption.[16] ODH has its own drawbacks too, such as difficulty of controlling the consecutive oxidation of alkanes/alkenes to carbon oxides, removal of reaction heat, and flammability of reaction mixture.[15] The key to these issues is the development of catalysts only activating the C-H bond of an alkane molecule.

There has also been research on partial oxidation of ethane to oxygenates such as acetic acid.[17-20] In the 1980s, a series of Mo-V-Nb oxide catalysts were studied. Under 2 MPa and at 400 – 500°C, acetic acid was produced along with ethene, CO, and CO_2[19-21]. The acetic acid selectivity is about 20% while ethylene selectivity is about 70%. With addition of Pd to the MoVNb catalysts, the acetic acid selectivity greatly increased to 80% and CO is completely oxidized to CO_2.[18] In liquid phase, ZSM-5 catalysts containing Fe and Cu are effective for the partial oxidation of ethane with hydrogen peroxide giving combined oxygenate selectivities and productivities of up to 95.2% and 65 mol $kg_{cat}^{-1}h^{-1}$, respectively. The conversion of ethane to acetic acid has a 56% conversion rate and 70%

selectivity. Ethene is also formed and can be subsequently oxidized.[17] More recently, on a Rh/HZSM-5 catalyst, ethane can be oxidized by hydrogen peroxide in aqueous solution to form acetic acid and formic acid at a temperature ≤ 50 °C at ethane pressure at 1.5 bar. Single Rh atom sites, Rh_1O_5 anchored in the micropores of the HZSM-5, is considered the active sites.[4]

Similar to that of methane, there has not been direct surface chemistry experimental work on Rh(111) to determine the activation barrier of ethane. In our lab, we measured the sticking coefficient of ethane with different gas and surface temperature, providing information on both gas activation and surface activation. Arrhenius fit was used to find the activation energy of ethane dissociation on Rh(111). The unusually high sticking coefficient at high surface temperature led to the study of carbon migration on Rh surface. However, the behavior of carbon and species formed on Rh(111) still need further investigation.

4.2 Experimental Method

The molecular beam doser and methodology for making effusive molecular beam measurements of alkane dissociative chemisorption is same as methane experiments for the most part, only the difference is described here in detail. Ethane was obtained from Matheson Tri-Gas (RES) and had a purity of 99.995%, and was further purified by flowing through a Supelco filter (model 2-2450-U), capable of removing trace amounts of reactive impurities. Experiments were performed using an ultrahigh vacuum (UHV) surface

analysis chamber equipped for Auger electron spectroscopy (AES) using a double pass cylindrical mirror analyzer, thermal programmed desorption, residual gas analysis, and effusive molecular beam dosing. The UHV chamber had a base pressure of 1×10^{-10} torr.

Due to carbon migration into the bulk as discussed in section 4.4, two methods were used to clean the surface. The first method is by Ar^+ ion sputtering at T_s at 700K with 5×10^{-5} torr of Argon and annealing to 1300K in good UHV, until no contaminants were detectable by AES. The second method is to oxygen cleaning at 900K, with 2×10^{-7} torr of oxygen for 20 minutes; then the oxygen is pumped out until the chamber pressure is below 10^{-9} torr; follows by Ar^+ ion sputtering at T_s at 700K with 5×10^{-5} torr of Argon for 10 minutes and annealing to 1300K in good UHV for 3 minutes, until no contaminants were detectable by AES. The detail is discussed in chapter 2.

For high surface temperatures, the final sticking coefficient is the slope of coverage versus exposure. For low surface temperatures, the sticking coefficient is acquired by fitting the coverage versus exposure to the coverage dependent sticking coefficient $\theta = \theta_{max}(1 - \exp\left(-\frac{S_0 \epsilon}{\theta_{max}}\right))$, as discussed in chapter 2.

The preliminary results were acquired with only argon sputtering as the cleaning method. The data excluded carbon diffusion (with oxygen cleaning and argon sputtering as a cleaning cycle before dosing) is being obtained at the time of writing.

4.3 Preliminary Results

4.3.1 Direct sticking coefficient

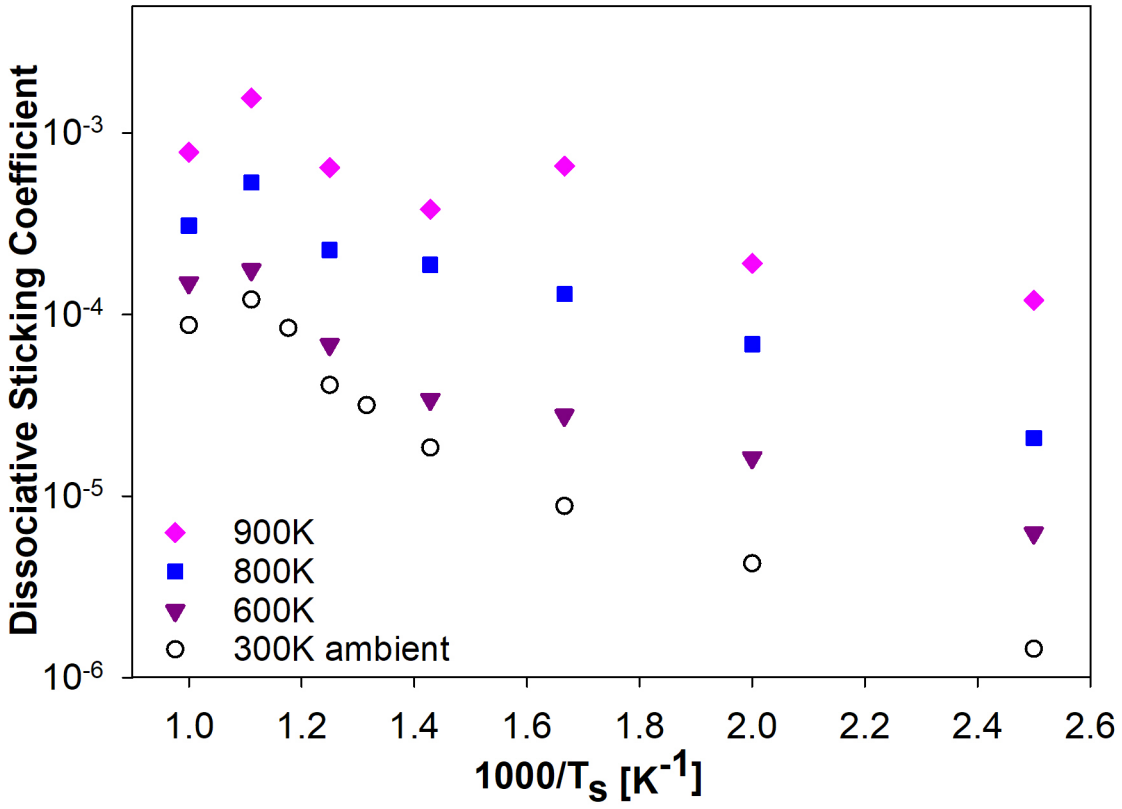

Figure 4-1 Sticking coefficient of ethane on Rh(111).

Direct sticking coefficient is shown in Figure 4-1. DSCs for every temperature are higher than those for methane. For every gas temperature, there is an apparent increase in sticking coefficients for surface temperatures of above 700 K. The sticking coefficients for 1000 K surface are all unusually lower than those of 900 K surface. For 900 K gas, the sticking coefficient for 600 K surface is higher than that of 700 K surface. The $S_n(T_g$ = 900K, T_s = 600K) and $S_n(T_g$ = 900K, T_s = 700K) experiments were both repeated twice, yet the results showed a consistency (Table 4-1).

Surface temp	Expt 1	Expt 2
600 K	0.000658	0.000665
700 K	0.000379	0.000464

Table 4-1 Sticking coefficients at 900K gas temperature, in two experiments. The sticking coefficients of 600 K surface are consistently higher than those of 700 K surface.

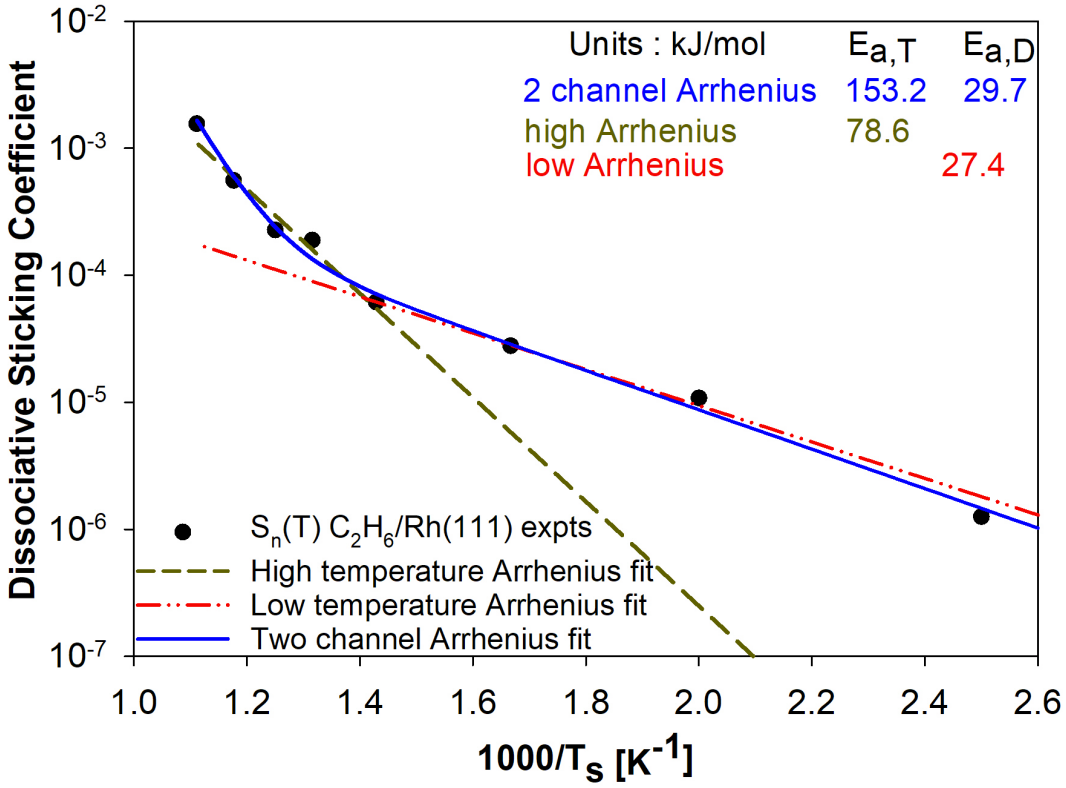

Figure 4-2 A dual channel Arrhenius fit to equilibrium experiments (900 K – 400 K)

Similar to methane, there are also two domains in ethane activation, one above 700 K and one below 700 K. Using Arrhenius fit $S = S_0 \exp\left(\frac{E_a}{RT}\right)$, activation energies and pre-exponential factors can be determined for each domain individually. A dual channel

Arrhenius fit in the form $S = S_T \exp\left(\frac{E_{a,T}}{RT}\right) + S_D \exp\left(\frac{E_{a,D}}{RT}\right)$ can also be used to find the composite activation energies and pre-exponential factors. The parameters from Arrhenius fits are listed in table 4-2.

Surface temp		Activation energy	Pre-exponential factor
Composite	High	153.2	1.13×10^{6}
	Low	29.7	0.0111
High temp		78.6	40.3
Low temp		27.4	6.91×10^{-3}

Table 4-2 Arrhenius fits parameters of the dual channel fit and two individual fits. Activation energy is in kJ/mol.

As seen in table 4-2, the activation energy of low temperature domain is 27.4 kJ/mol, which is slightly lower than that of methane, 32.1 kJ/mol. However, for the high temperature domain, activation energy from either the dual-channel fit or the single channel fit is higher than that of methane (65.8 kJ/mol). The pre-exponential factors are both greater than 1, for the dual-channel fit, in the order of 10^6.

It is later discovered that, on Rh, carbon can migrate into the bulk and out of the bulk on to the surface under certain circumstances. Moreover, there appears to be different behaviors exhibited when dosing C1 versus C2 species on Rh(111). Indeed, different reactive behaviors have been seen between acetylene and ethylene derived C deposited on Pt(111).[22] Hence, the preliminary sticking coefficients presented here may be subject to some systematic error. Carbon segregation on Rh is discussed in detail in the next section.

4.3.2 Angle-resolved sticking coefficient

The sticking coefficient from -14 to 24 degrees were measured with the center of the crystal being 1.0 mm from the centerline of the doser. Compared to methane, DSCs are one order of magnitude larger. However, the cosine dependence is found to be 6.5, which is close to that of methane, 6.0. As a comparison, on Pt(111), the cosine power dependence for methane is 12.8, ethane is 5.6.[23] This could be qualitatively explained by potentially high vibrational efficacy on Rh and high degrees of freedom in ethane. From the dynamically biased PMMT model on Rh(111) and Pt(111), the efficacies of vibrational energy in methane activation are 0.55 and 0.4, respectively. For a more quantitative analysis, a PMMT model from multidimensional DSCs of ethane on Rh(111) is needed with sticking coefficients that are not affected by carbon migration, which we believe to be the case here at T_s=700 K.

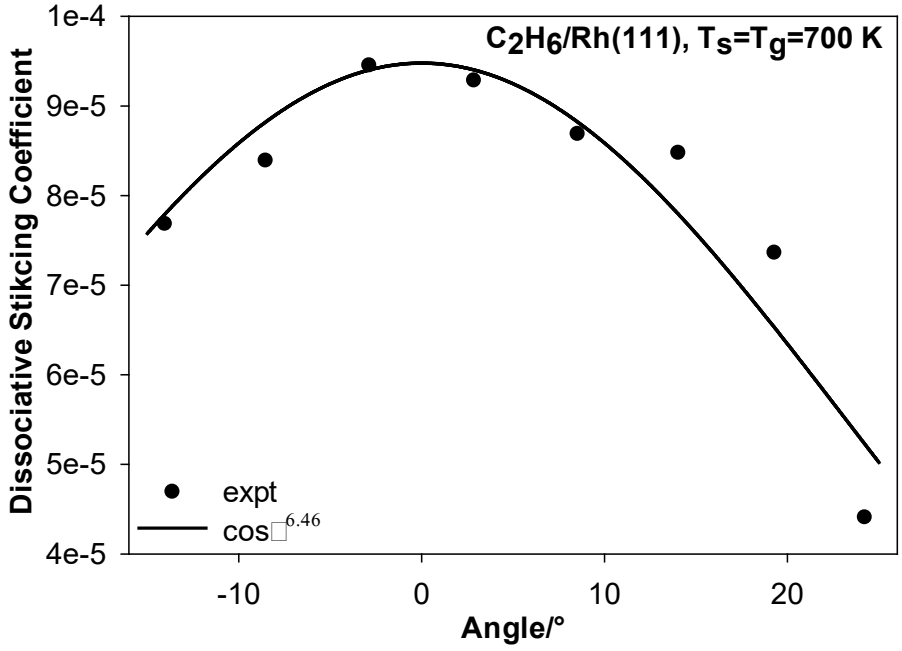

Figure 4-3 Angle-resolved sticking coefficient of ethane on Rh(111). T_g = T_s = 700K

4.4 Carbon segregation

The sticking coefficients for high surface temperature (above 800 K) are unusually high for every gas temperature measured. The dual-channel Arrhenius fit yields an activation energy of 153 kJ/mol with a pre-exponential factor of 10^6. This activation energy is comparable to that for carbon diffusion in bulk Rh, which is 135 kJ/mol.[24] Subsurface carbon is a general feature of noble metals[25] and the behavior of subsurface carbon may affect sticking coefficient measurements to a considerable extend (as shown in the following section, DSC values can be different by two folds depending on different dosing time) and hence not only a clean surface but also a clean subsurface is required for accurate experiments. For argon sputtered surface, carbon migrates onto the surface at a considerable rate at surface temperature of 900 K:

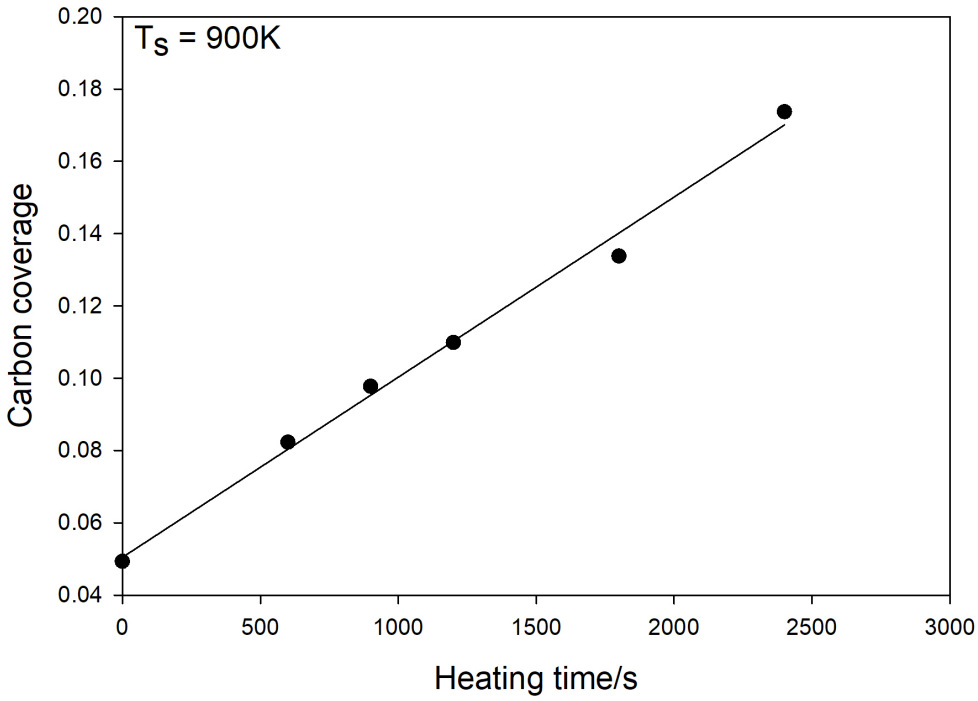

Figure 4-4 Carbon migration on "cleaned" Rh surface. Chamber pressure is 9×10^{-10} torr. Carbon coverage increases about 3% per 10 minutes.

4.4.1 *Carbon migration on Rh surface*

Carbon diffusion coefficient D is a function of bulk temperature T[24]:

$$D = D_0 e^{-\frac{E_{diff}}{kT}}$$

where D_0 is the prefactor, E_{diff} is the diffusion activation energy, k is the Boltzmann constant. The temperature dependent diffusion coefficient is shown in Figure 4-5.

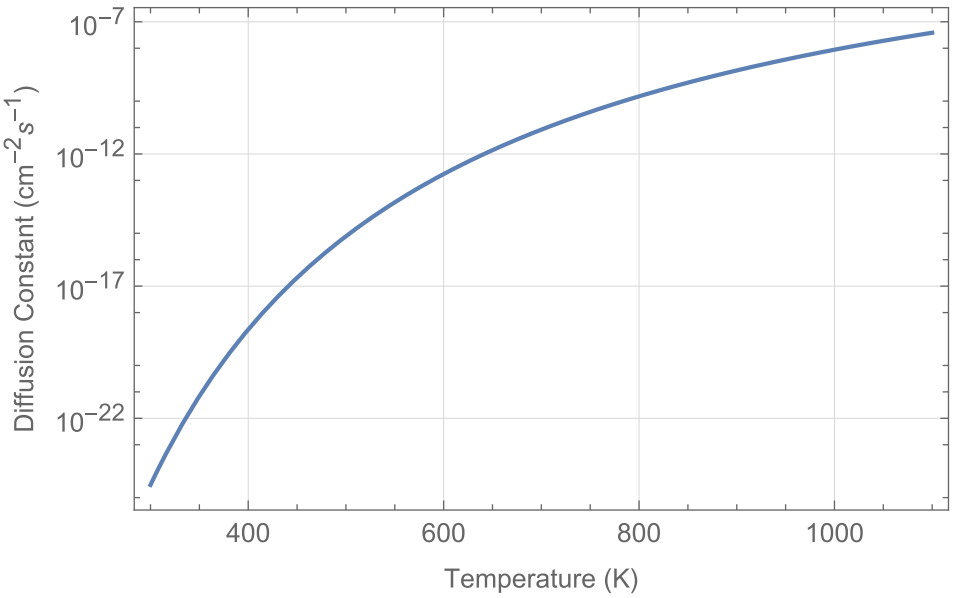

Figure 4-5 Diffusion coefficient with respect to bulk temperature. The coefficient increases exponentially with inversed temperature.

If the initial concentration in the bulk is uniform and there is no additional activation energy to move from the surface to the bulk, then the incremental bulk concentration of carbon at time τ should be:

$$C_b(x,\tau) = \int_0^t \frac{\exp\left(-\frac{x^2}{4D\tau}\right)}{(\pi D\tau)^{\frac{1}{2}}} \mathrm{d}\tau$$

x is the depth into the bulk, *D* is diffusion coefficient at that temperature. For one monolayer of carbon on Rh(111) surface, if all the carbon is homogeneously dissolved in 1 mm thick of crystal, the bulk concentration is 2.21×10^{-7} (carbon atom per rhodium atom). However, dissolving in the solid state takes a long time to reach equilibrium. Figure 4-5 shows, in 1 day, at different temperatures, with an initially clean bulk, the carbon fraction distribution across the depth of the crystal. At 700K, most carbon would still be in the top 0.005 cm region with the topmost concentration of 1.85×10^{-5}; at 800K, most carbon would still be in the top 0.015 cm region, top most concentration around 4.5×10^{-6}; at higher temperatures, carbon dissolves into the bulk more quickly and carbon distributes more evenly across the bulk.

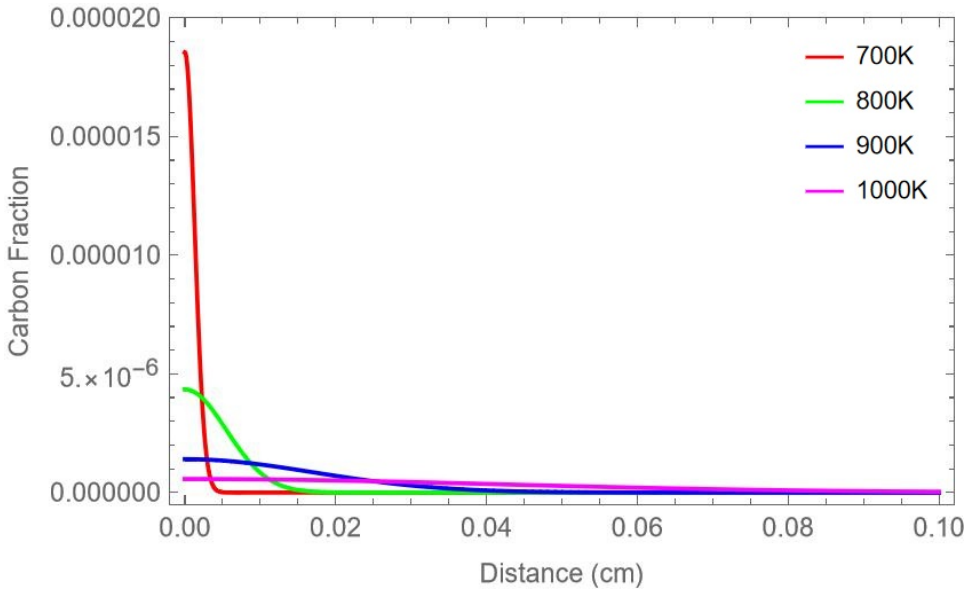

Figure 4-6 carbon fraction at different depth in the bulk for about 1 day.

Under the same assumptions as above, at 900K where carbon is calculated to dissolve at a noticeable rate, it takes about 16 minutes to get 0.005 cm into the bulk, about 2.7 hours to get 0.015 cm into the bulk, and days to get evenly distributed across the bulk. Figure 4-

5 shows the mean distance traveled by carbon from the surface with time. At 700K, carbon migrates very slowly; while at 1000K, carbon migrates at a considerable rate.

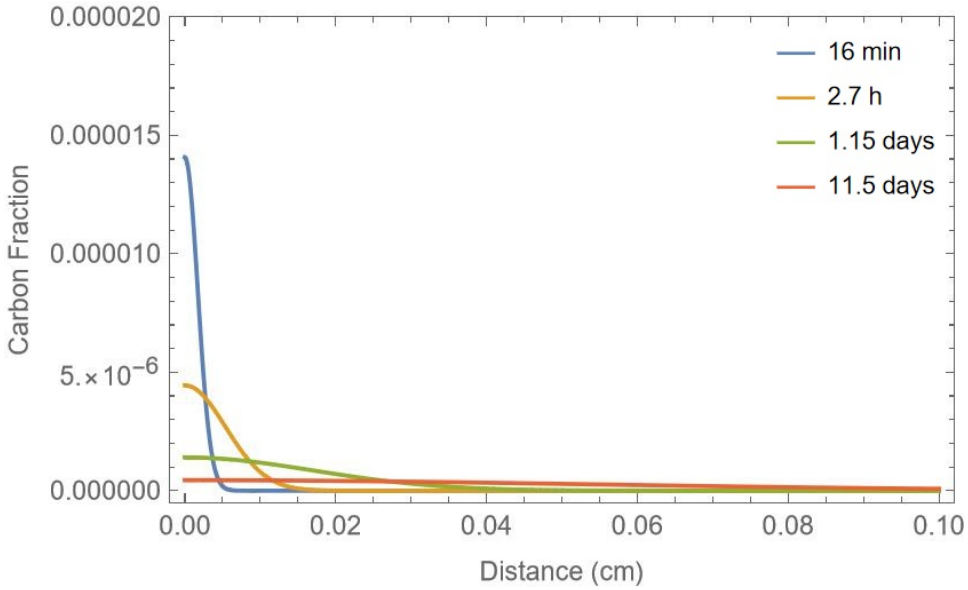

Figure 4-7 Carbon fraction at different depth in the bulk at 900K.

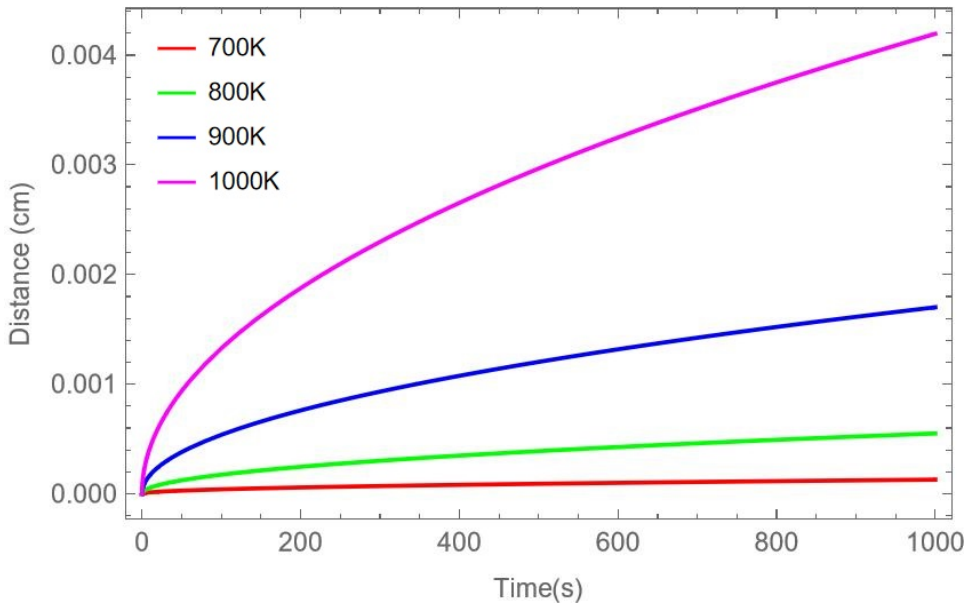

Figure 4-8 Mean distance traveled by carbon atoms into the bulk at different temperatures

Figure 4-9 shows the calculated equilibrium carbon coverage on the surface at different bulk carbon concentrations at different temperatures based on the equality of the chemical potentials of C in the bulk and at the surface as isolated C atoms and on DFT derived values for C atom energies.[24-27] At low concentrations, carbon only shows on the surface at low temperatures (below 500K); with increasing concentrations, carbon starts to show on surface at elevated temperature(above 600K). Notice that 1 monolayer of carbon on a 1 mm thick Rh(111) crystal equals to bulk concentration of 2.21×10^{-7} if disturbed evenly across the crystal. Since carbon coverage measurements were all done at below 350K, all carbon deposited from ethane should be detectable by AES.

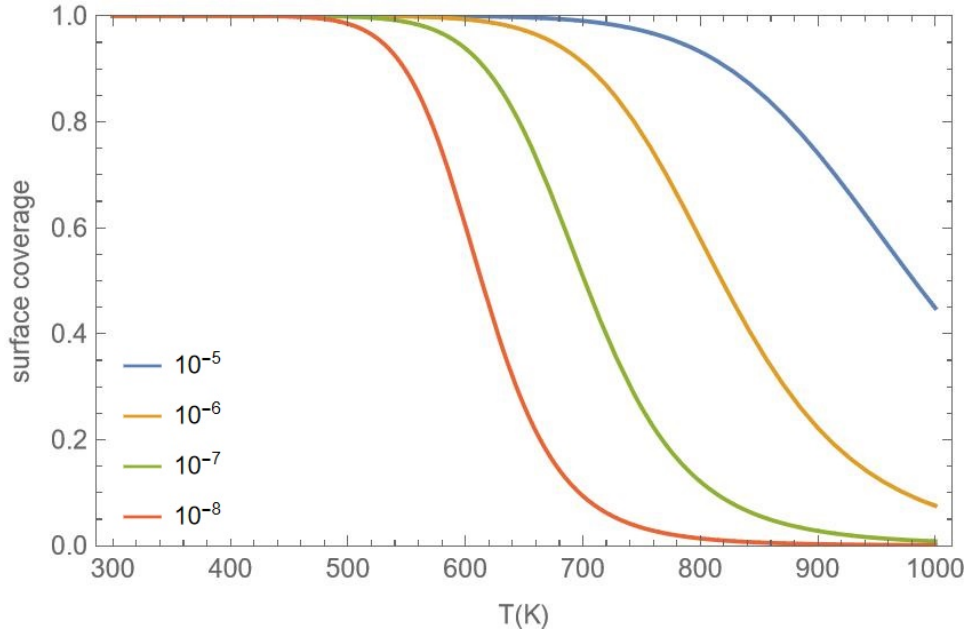

Figure 4-9 Under equilibrium, at different bulk concentrations, surface carbon coverage with respect to temperature - Rh(111)

In comparison, on Pt(111), surface carbon coverage decreases at lower temperatures than on Rh(111) at equivalent bulk concentrations. Due to that surface carbon is less stable relative to bulk carbon on Pt(111).

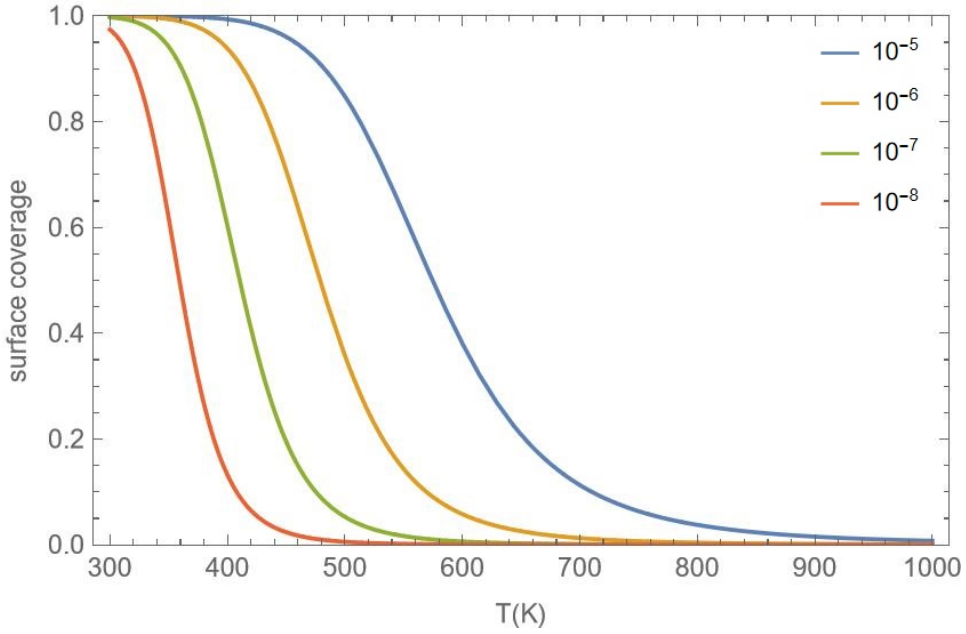

Figure 4-10 Under equilibrium, at different bulk concentrations, surface carbon coverage with respect to temperature - Pt(111)

It is worth noting that the carbon segregation discussed in this section is about carbon atoms. On a Rh(111) surface, it is easy to form graphene from C_2 species[28], hence this may change the equilibrium towards carbon migrating onto the surface by introducing a more stable form of C at the surface.

4.4.2 Correction to carbon migration

Although it is ideal to get a clean surface and bulk, this is difficult to achieve. Four cycles of oxygen cleaning at 2×10^{-7} torr at 900K for one hour followed by argon sputtering at 5×10^{-5} torr at 700 K for 20 minutes were done in a period of three days; upon heating the surface to 900K, there was still carbon growth on the surface. However, carbon coverage increase seems to be at a constant rate. This provides opportunities to correct for carbon migration to get the actual carbon deposition from gas dosing (ethane dissociative chemisorption) rather than carbon migration from the bulk.

In three experiments, carbon coverage increase rate was tested. The surface was cleaned first and then dosed by ethane ambiently at 900K surface temperature. Then the surface was heated to 900K without dosing to test the carbon growth on the surface. The cleaning and dosing condition are tabulated in Table 4-3 and Figures 4-12 to 4-14. The growth rate, *r*, was determined for each experiment. The carbon deposition θ' were assumed to be only from two sources: ethane dissociative chemisorption, θ_c, and carbon migration from the bulk, θ_m.

$$\theta' = \theta_c + \theta_m$$

Based on growth rate *r* and dosing time *t*, the carbon amount from migration from the bulk could be determined by,

$$\theta_m = rt$$

Then the actual carbon deposition from ethane can be calculated as,

$$\theta_c = \theta' - rt$$

Once the carbon deposition from ethane was determined, a new sticking coefficient that excluded migration could be calculated.

	Dosing pressure/torr	Total dosing time/min	Cleaning method	note
A	5×10^{-6}	40	Ar^+ sputter only	Ar^+ sputtered then heat to 900K
B	3.5×10^{-5}	15	O_2 cleaning and Ar^+ sputter	Heat to 900K after dosing
C	2×10^{-6}	60	O_2 cleaning and Ar^+ sputter	Heat to 900K after dosing

Table 4-3 Three experiments done to determine carbon growth rate

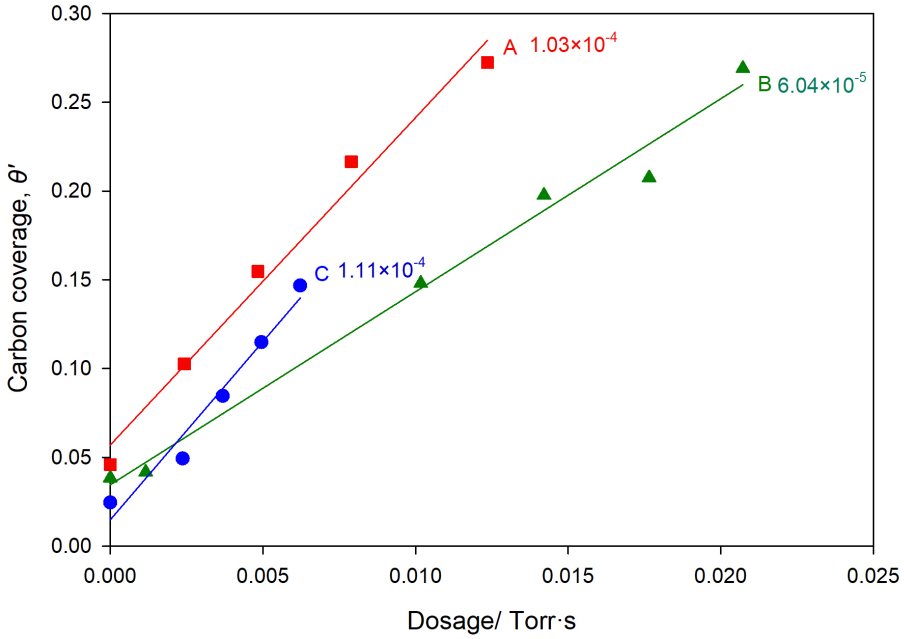

Figure 4-11 Ethane ambient dosing at 900K. When not counting carbon migration, the sticking coefficients (slope) were not reproducible.

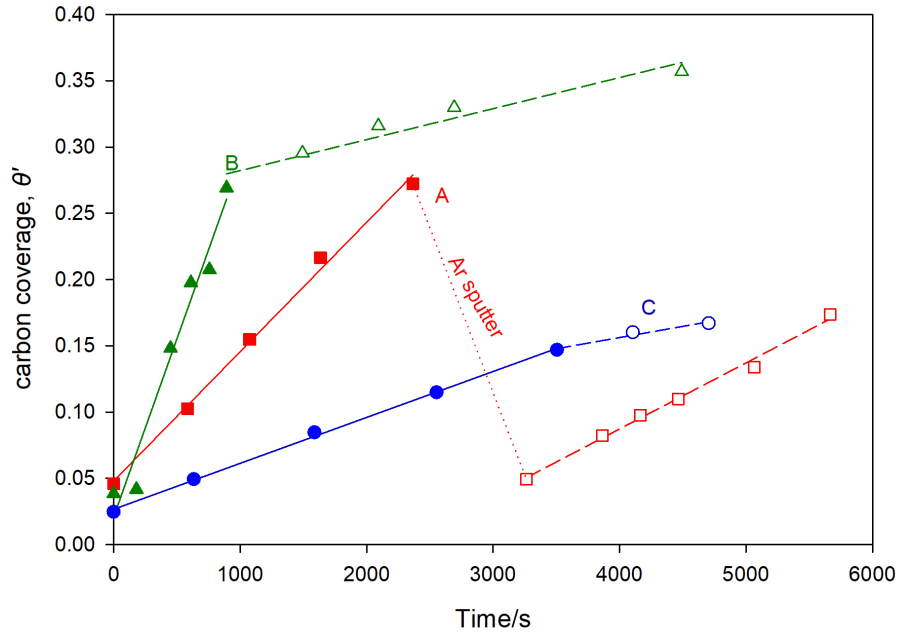

Figure 4-12 Ethane dosing time and carbon coverage increase. Ethane was first ambiently dosed on 900K surface (solid lines). Then the crystal was then heated to 900K in vacuum (dash lines). Carbon coverage increase at a steady rate even without any ethane in the gas phase. This carbon is assumed to be from the bulk. The slope of the dash line is the carbon growth rate, r.

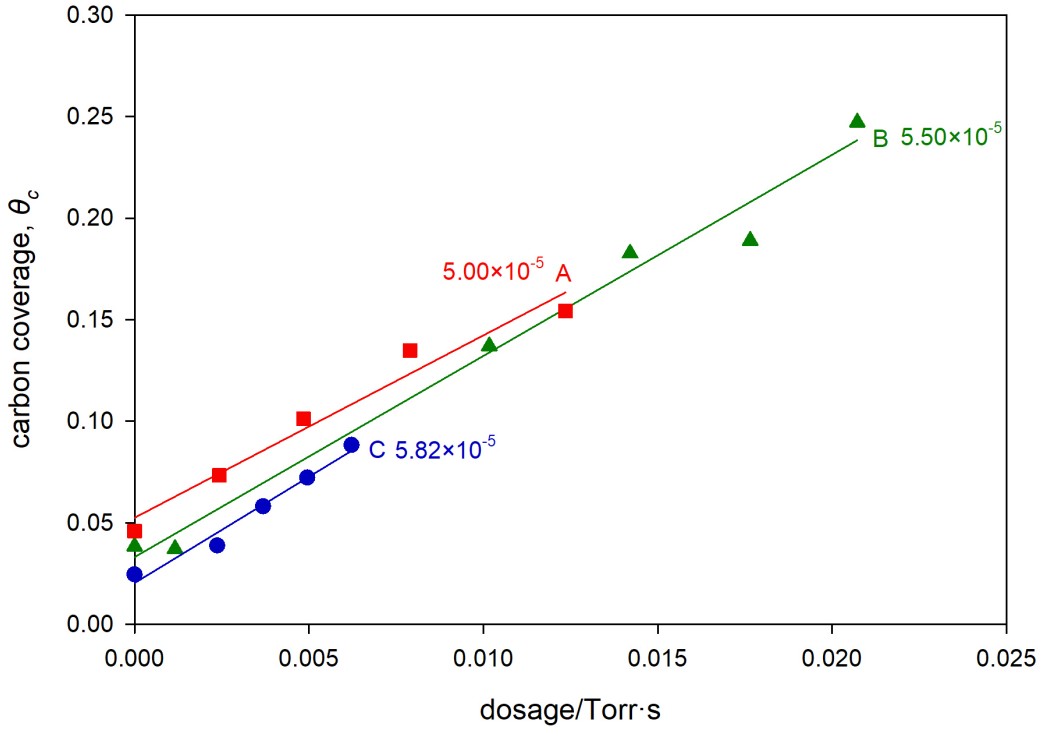

Figure 4-13 Ethane dosage and carbon coverage when carbon migration is excluded. The points on this graph are only the carbon deposition from ethane dissociative chemisorption. The sticking coefficients (slope) are reproducible now.

This might provide opportunity in acquiring the actual sticking coefficient when getting a clean surface and bulk is difficult. However, the assumption here is that all the carbon from ethane dissociative chemisorption stays on the surface at this temperature and carbon growth rate is linear in the coverage range in question. Further studies are being conducted at the time of writing.

To summarize, at surface temperatures above 1000 K, no C is observed on the surface following dosing of ethane. This phenomenon is attributed to fast diffusion of C into the Rh bulk relative to the time necessary to measure the C coverage by AES (i.e., ~ 5 mins).

At temperatures of 800 K and below, there is no experimental evidence for either dissolution of C into the bulk nor growth of carbon coverage coming from the bulk. Only the intermediate temperature range of ~900 K is growth of C coverage observed after ethane is dose. Interestingly, if the surface is cleaned and then held at 900K in the absence of dosing ethane then there is no growth of C coverage with time. We speculate that this is because ethane dissociative chemisorption at 900 K generates polymeric C species or graphene species that bulk C atoms can attach to which provides a more energetically stable final state than a surface carbon atom. At higher temperatures, C diffusion into the bulk becomes too fast. At lower temperatures, C diffusion is too slow, as may be formation of favorable C polymeric species on the surface, to influence the C coverage deposited by dissociative chemisorption.

4.5 Defects Level Monitored by Change of Sticking Coefficients from Sputtering

To test if the step sites are indeed contributing to the elevated sticking coefficient at low temperatures, dosing experiments at different step sites density can be a good indication. Fcc crystals can be cut to different orientations to form stepped surface with different step density. Table 4-3 listed the miller index and stepped surface designation some common step surfaces.

miller index	stepped surface designation
(544)	(S)-[9(111)x(100)]
(755)	(S)-[6(111)x(100)]
(533)	(S)-[4(111)x(100)]
(211)	(S)-[3(111)x(100)]
(311)	(S)-[2(111)x(100)]

Table 4-4 Common step surfaces and their designation

However, due to the limitations in the lab, only a Rh(111) surface is available. Hence, argon ion sputtering is used to create defect sites on the surface.[29-32] The ion flux on the surface can be calculated by measuring the current from the crystal to ground.

$$I = \frac{Q}{t} = \frac{N \times e}{t} = \frac{\% \times N_{Rh} \times e}{t} = \frac{D \times A \times e}{t} = F \times A \times e$$

where Q is the electric charge, t is the time the crystal being hit by the ions, N is the number of electrons, e is the elementary charge, % is the percentage of Rh atoms being hit by an argon ion, N_{Rh} is amount of Rh on the crystal surface, D is the ion dose, A is the area of the crystal surface, and F is the ion flux. The area of the surface is approximately 7.5×10^{-5} m^2. The relation between argon pressure in the chamber and the current is shown in figure 4-15. At typical argon sputter pressure 5×10^{-5} torr, the ion current is 2.2 μA, then there's 1.16% of Rh atoms being hit by an argon ion every second, equals to an ion flux of 1.83×10^{17} ions/m^2s.

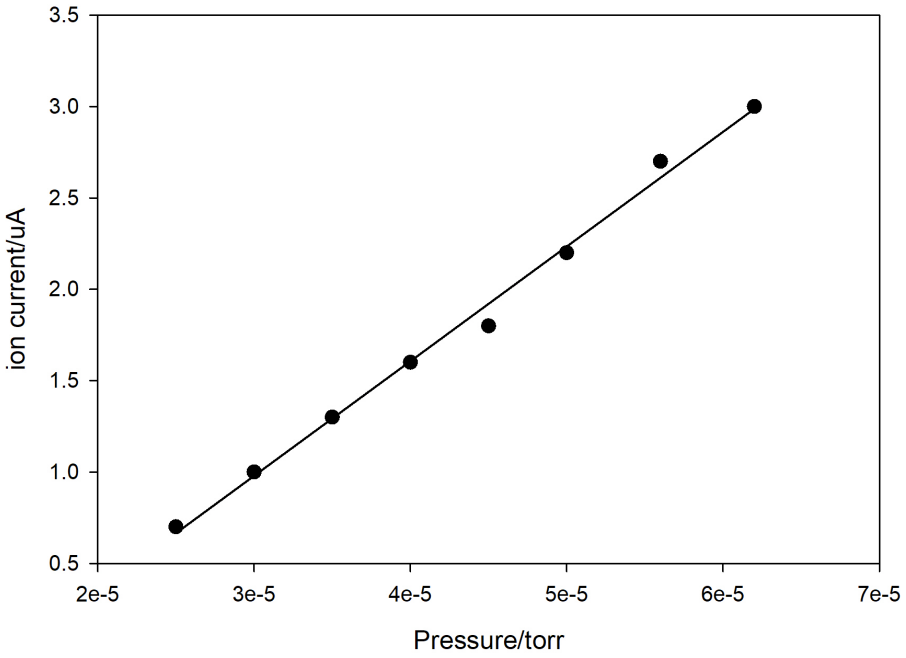

Figure 4-14 Ion current with respect to chamber pressure in Ar^+ ion sputtering

Theoretically, if the sputtering efficiency is 1, each ion bombardment leaves a vacancy site on the surface, thus it should take 86 second for every Rh atom on surface to be bombarded. However, the sputtering efficiency is not 1 since the weight of Rh (103) is 2.5 times the weight of Ar (40); also, the surface undergoes reconstruction simultaneously during the sputtering process. This reconstruction leaves surface vacancy islands of different sizes depending on the sputtering and/or annealing temperature. In our previous experiments on methane sticking coefficients on Rh(111) surface, sputtering at 700K rendered a surface with three times difference in sticking coefficients for methane. This agrees with earlier research that sputtering at elevated temperatures only produce large vacancies of thousands of angstrom[33-35], where defect density is only twice as much as a flat surface that has a miscut of 0.1º (See sample calculations next page). To create a surface with more than 10 times higher defect density, sputtering at low temperatures is required to create vacancy island sizes of ~250 Å. On Au(111), sputtering with 500 eV Ar ion beam at temperature range of 25 – 150 ℃, vacancy island sizes are in the range of 10 – 350 Å.[35] The lower sized vacancy islands decrease in number and the higher sized vacancy islands increase in number with increasing sputtering temperature. However, since sticking coefficients get too low at low temperature, a comparison is not easily done at such temperatures. Thus, a temperature where enough vacancies could be created while sticking coefficient changes can be measured is needed. At 125 ℃ (about 400K), the majority of the vacancy island sizes are between 100 and 200 Å in diameter on Au(111), which would likely cause a big enough change in step density. The sticking coefficient of ethane at 400K on the flat Rh(111) is on the order of 10^{-6}, which is easily measurable. Hence, 400 K surface was chosen to compare the sticking coefficients of sputtered and annealed surface. The

sputter time explored were 10 and 20 minutes, which are well over 1 monolayer ion dosage.[33]

Calculation of step density with different vacancy island sizes

For a sample area of 10000 × 10000 atoms with a miscut to 0.1, the step density is arctan (0.1°) = 0.0017, the number of step sites is $0.0017 \times 10000 \times 10000 = 1.7 \times 10^5$

The sample area has an area of $(1.35 \times 10000)^2 = 1.82 \times 10^8$ *Å*^{2}

The area of a 2100 Å diameter island is $\pi \times (2100/2)^2 = 3.46 \times 10^6$ *Å*^{2}

Hence the sample area has $1.82 \times 10^8 / 3.46 \times 10^6 = 52$ *such islands.*

52 islands of 2100 Å diameter has a total perimeter of $52 \times \pi \times 2100 = 3.4 \times 10^5$ *Å which is equal to* $3.4 \times 10^5 / 1.35 = 2.6 \times 10^5$ *atoms of step sites*

Hence an area with vacancy island size of 2100 Å has about twice as many as step sites as a flat surface miscut to 0.1°.

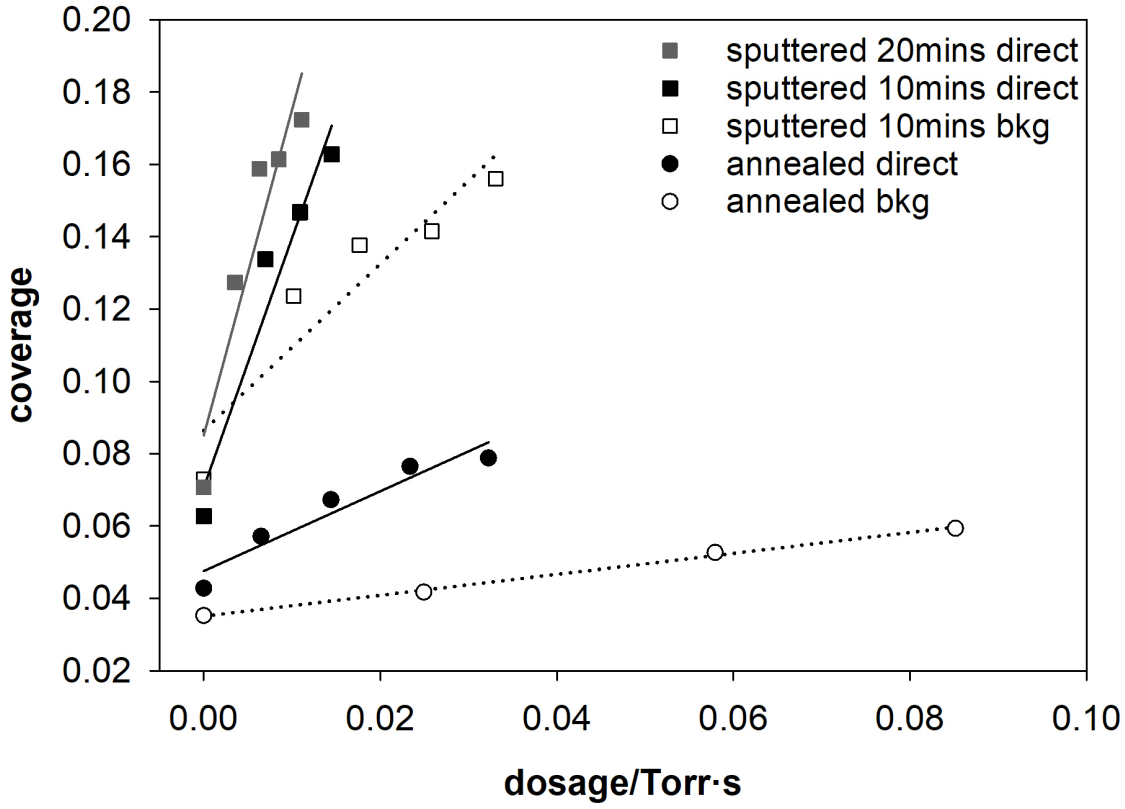

Figure 4-15 Carbon accumulation on cleaned (circles) and sputtered (squares) surface. Hollow points/dots show the background dosing and filled points/lines show the direct dosing.

As can be seen on figure 4-8, sputtered surface has a high sticking coefficient as well as a higher saturation coverage. Background sticking coefficient increased nearly ten-fold, from 1.4×10^{-6} on annealed surface to 1.3×10^{-5} on sputtered surface. Varying sputtering time, however, does not change sticking coefficient significantly, likely because that when sputter dosage is higher than a monolayer, surface morphology depends on the equilibrium between the sputter rate and the temperature-dependent rate of repair of the surface by atomic diffusion.

4.6 Outlook

Ethane activation on Rh(111) is proven to be more complicated than the situation for methane. Carbon segregation in each direct would interfere with sticking coefficient measurements. C2 species might favor the formation of polymeric C or graphene on the surface which was not observed for methane[28], which may further complicate carbon behavior on Rh(111) surface. A more robust way to clean the Rh surface is needed and cleanliness in the surface, the sub-surface, and the bulk needs to be checked carefully. Other than AES, more surface sensitive techniques, such as STM for checking the formation of graphene, XPS for checking the C-C sp^2 bond of graphene, and SIMS for checking carbon concentration at different depth could provide more information on ethane dissociative chemisorption kinetics on Rh surface.

Reference

1. Jeong, S.; Kim, S.; Lee, B.; Ryi, S.-K.; Lim, H., Techno-Economic Analysis: Ethane Steam Reforming in a Membrane Reactor with H2 Selectivity Effect and Profitability Analysis. *International Journal of Hydrogen Energy* **2018**, *43*, 7693-7702.
2. Furlan, C.; Mortarino, C., Forecasting the Impact of Renewable Energies in Competition with Non-Renewable Sources. *Renewable and Sustainable Energy Reviews* **2018**, *81*, 1879-1886.
3. Moldoveanu, S. C., Chapter 2 - Pyrolysis of Hydrocarbons. In *Pyrolysis of Organic Molecules (Second Edition)*, Moldoveanu, S. C., Ed. Elsevier: 2019; pp 35-161.
4. Li, Y.; Tang, Y.; Luan, N.; Tao, F. F., Catalytic Oxidation of Ethane to Carboxylic Acids in the Liquid Phase at near Room Temperature at Ambient Pressure. *Acs Sustainable Chemistry & Engineering* **2019**, *7*, 4707-+.
5. Le Van Mao, R.; Yan, H.; Muntasar, A.; Al-Yassir, N., Chapter 7 - Blending of Non-Petroleum Compounds with Current Hydrocarbon Feeds to Use in the Thermo-Catalytic Steam-Cracking Process for the Selective Production of Light Olefins. In *New and Future Developments in Catalysis*, Suib, S. L., Ed. Elsevier: Amsterdam, 2013; pp 143-173.
6. Ethane Cracking in the Uppoer Ohio Valley: Potential Impacts, Regulatory Requirements, and Opportunities for Public Engagement. Environmental Law Institute: 2018.
7. Bodke, A. S.; Olschki, D. A.; Schmidt, L. D.; Ranzi, E., High Selectivities to Ethylene by Partial Oxidation of Ethane. *Science* **1999**, *285*, 712-715.
8. Tanios, C.; Labaki, M., Chapter 5 - Catalytic Reforming: A Sustainable Technology for Hydrogen Production. In *Recent Advances in Renewable Energy Technologies*, Jeguirim, M., Ed. Academic Press: 2022; pp 199-247.
9. Chiuta, S.; Engelbrecht, N.; Human, G.; Bessarabov, D. G., Techno-Economic Assessment of Power-to-Methane and Power-to-Syngas Business Models for Sustainable Carbon Dioxide Utilization in Coal-to-Liquid Facilities. *Journal of CO2 Utilization* **2016**, *16*, 399-411.
10. Szima, S.; Cormos, C.-C., Exergoeconomic Analysis for a Flexible Dry Reforming Power Plant with Carbon Capture for Improved Energy Efficiency. In *Computer Aided Chemical Engineering*, Kiss, A. A.; Zondervan, E.; Lakerveld, R.; Özkan, L., Eds. Elsevier: 2019; Vol. 46, pp 1681-1686.
11. Solymosi, F.; Szőke, A.; Egri, L., Decomposition of Methane and Its Reaction with Co2 over Rh/Zsm-5 Catalyst. *Top Catal* **1999**, *8*, 249-257.
12. Amghizar, I.; Vandewalle, L. A.; Van Geem, K. M.; Marin, G. B., New Trends in Olefin Production. *Engineering* **2017**, *3*, 171-178.
13. Sattler, J. J. H. B.; Ruiz-Martinez, J.; Santillan-Jimenez, E.; Weckhuysen, B. M., Catalytic Dehydrogenation of Light Alkanes on Metals and Metal Oxides. *Chem. Rev.* **2014**, *114*, 10613-10653.
14. Bychko, I.; Abakumov, A.; Nikolenko, A.; Selyshchev, O. V.; Zahn, D. R. T.; Khavrus, V. O.; Tang, J. G.; Strizhak, P., Ethane Direct Dehydrogenation over Carbon Nanotubes and Reduced Graphene Oxide. *Chemistryselect* **2021**, *6*, 8981-8984.
15. Grabowski, R., Kinetics of Oxidative Dehydrogenation of C2 - C3alkanes on Oxide Catalysts. *Catalysis Reviews* **2006**, *48*, 199-268.
16. Bryukov, M. G.; Palankoeva, A. S.; Belyaev, A. A.; Arutyunov, V. S., Partial Oxidation of Ethane in the Temperature Range 773-1023 K. *Kinet Catal+* **2021**, *62*, 703-711.
17. Forde, M. M., et al., Partial Oxidation of Ethane to Oxygenates Using Fe- and Cu-Containing Zsm-5. *J Am Chem Soc* **2013**, *135*, 11087-11099.
18. Soliman, M.; Al-Zeghayer, Y.; Al-Awadi, A. S.; Al-Mayman, S., Economics of Acetic Acid Production by Partial Oxidation of Ethane. *APCBEE Procedia* **2012**, *3*, 200-208.

19. Ruth, K.; Burch, R.; Kieffer, R., Mo–V–Nb Oxide Catalysts for the Partial Oxidation of Ethane: Ii. Chemical and Catalytic Properties and Structure Function Relationships. *J Catal* **1998**, *175*, 27-39.
20. Ruth, K.; Kieffer, R.; Burch, R., Mo–V–Nb Oxide Catalysts for the Partial Oxidation of Ethane: I. Preparation and Structural Characterisation. *J Catal* **1998**, *175*, 16-26.
21. Thorsteinson, E. M.; Wilson, T. P.; Young, F. G.; Kasai, P. H., The Oxidative Dehydrogenation of Ethane over Catalysts Containing Mixed Oxides of Molybdenum and Vanadium. *J Catal* **1978**, *52*, 116-132.
22. Deng, R.; Herceg, E.; Trenary, M., Identification and Hydrogenation of C2 on Pt(111). *J Am Chem Soc* **2005**, *127*, 17628-17633.
23. Navin, J. K.; Donald, S. B.; Harrison, I., Angle-Resolved Thermal Dissociative Sticking of Light Alkanes on Pt(111): Transitioning from Dynamical to Statistical Behavior. *J Phys Chem C* **2014**, *118*, 22003-22011.
24. Rut'kov, E. V.; Kuz'michev, A. V.; Gall, N. R., Carbon Interaction with Rhodium Surface: Adsorption, Dissolution, Segregation, Growth of Graphene Layers. *Phys Solid State+* **2011**, *53*, 1092-1098.
25. Piqué, O.; Koleva, I. Z.; Viñes, F.; Aleksandrov, H. A.; Vayssilov, G. N.; Illas, F., Subsurface Carbon: A General Feature of Noble Metals. *Angewandte Chemie* **2019**, *131*, 1758-1762.
26. Laguës, M.; Domange, J. L., Surface Segregation: Comparison between Theory and Experiment. *Surf Sci* **1975**, *47*, 77-85.
27. Rut'kov, E. V.; Afanas'eva, E. Y.; Lavrovskaya, N. P.; Gall, N. R., Surface and Bulk Effects in Graphene Growth and Destruction on Rhodium. *Phys Solid State+* **2021**, *63*, 1769-1774.
28. Wang, B., et al., Ethene to Graphene: Surface Catalyzed Chemical Pathways, Intermediates, and Assembly. *The Journal of Physical Chemistry C* **2017**, *121*, 9413-9423.
29. Makeev, M. A.; Cuerno, R.; Barabási, A.-L., Morphology of Ion-Sputtered Surfaces. *Nuclear Instruments and Methods in Physics Research Section B: Beam Interactions with Materials and Atoms* **2002**, *197*, 185-227.
30. Eklund, E. A.; Bruinsma, R.; Rudnick, J.; Williams, R. S., Submicron-Scale Surface Roughening Induced by Ion Bombardment. *Phys. Rev. Lett.* **1991**, *67*, 1759-1762.
31. Michely, T.; Teichert, C., Adatom Yields, Sputtering Yields, and Damage Patterns of Single-Ion Impacts on Pt(111). *Phys Rev B* **1994**, *50*, 11156-11166.
32. Michely, T.; Comsa, G., Temperature-Dependence of the Sputtering Morphology of Pt(111). *Surf Sci* **1991**, *256*, 217-226.
33. Kalff, M.; Comsa, G.; Michely, T., Temperature Dependent Morphological Evolution of Pt(111) by Ion Erosion: Destabilization, Phase Coexistence and Coarsening. *Surf Sci* **2001**, *486*, 103-135.
34. Michely, T.; Comsa, G., The Scanning Tunneling Microscope as a Means for the Investigation of Ion Bombardment Effects on Metal Surfaces. *Nuclear Instruments and Methods in Physics Research Section B: Beam Interactions with Materials and Atoms* **1993**, *82*, 207-219.
35. Bose, A. C.; Yoshitake, M., Pattern Formation Induced by Ar+ Sputtering on Au(111). *Appl Surf Sci* **2005**, *241*, 174-178.